



Michigan Technological University
Create the Future Digital Commons @ Michigan Tech

Dissertations, Master's Theses and Master's
Reports - Open

Dissertations, Master's Theses and Master's
Reports

2011

***In-situ* electrical, mechanical and electrochemical characterizations of one-dimensional nanostructures**

Hessam Mir Shah Ghassemi
Michigan Technological University

Follow this and additional works at: <https://digitalcommons.mtu.edu/etds>

 Part of the [Mechanical Engineering Commons](#)

Copyright 2011 Hessam Mir Shah Ghassemi

Recommended Citation

Ghassemi, Hessam Mir Shah, "*In-situ* electrical, mechanical and electrochemical characterizations of one-dimensional nanostructures", Dissertation, Michigan Technological University, 2011.
<https://doi.org/10.37099/mtu.dc.etds/364>

Follow this and additional works at: <https://digitalcommons.mtu.edu/etds>

 Part of the [Mechanical Engineering Commons](#)

IN-SITU ELECTRICAL, MECHANICAL AND ELECTROCHEMICAL
CHARACTERIZATIONS OF ONE-DIMENSIONAL NANOSTRUCTURES

by
Hessam Mir Shah Ghassemi

A DISSERTATION
Submitted in partial fulfillment of the requirements for the degree of
DOCTOR OF PHILOSOPHY

(Mechanical Engineering-Engineering Mechanics)

MICHIGAN TECHNOLOGICAL UNIVERSITY

2011

© 2011 Hessam Ghassemi

This dissertation, “*In-situ* Electrical, Mechanical and Electrochemical Characterizations of One-Dimensional Nanostructures,” is hereby approved in partial fulfillment of the requirements for the Degree of DOCTOR OF PHILOSOPHY IN MECHANICAL ENGINEERING-ENGINEERING MECHANICS.

Department of Mechanical Engineering-Engineering Mechanics

Signatures:

Dissertation Co-Advisor

Reza S. Yassar

Dissertation Co-Advisor

Yoke Khin Yap

Department Chair

William W. Predebon

Date

Table of Content

Table of Content	3
LIST OF FIGURES	5
LIST OF TABLES	13
Preface	14
Acknowledgments	16
Abstract	17
1 -INTRODUCTION	19
1. 1. One-Dimensional Nanostructures	19
1.1.1 Boron Nitride Nanotubes	20
1.1.2 Silicon Nanowire/Nanorods	22
1. 2. The Order of Chapters in This PhD Dissertation	22
2 -EXPERIMENTAL GROWING METHOD	26
3 -ON THE MECHANICAL BEHAVIOR OF BORON NITRIDE NANOTUBES	28
3.1. Introduction	28
3.2. Thermal Vibrations of BN nanotube	29
3.3. Electric Field Induced Resonance Method	31
3.4. Multi-Cycle Bending Deformation	33
3.5. Direct Force Measurement under Combined AFM and TEM	35
3.6. Modeling and Simulation of BN Nanotube Mechanics	37
3.7. Conclusion	42
4 -REAL-TIME FRACTURE DETECTION OF INDIVIDUAL BORON NITRIDE NANOTUBES IN SEVERE CYCLIC DEFORMATION PROCESSES	44
4. 1. Introduction	44
4. 2. Experimental Procedure	45
4. 3. Results and Discussion	46
4. 4. Conclusion	53
5 - <i>IN-SITU</i> OBSERVATION OF REVERSIBLE RIPPLING IN MULTI-WALLED BORON NITRIDE NANOTUBES	54
5. 1. Introduction	54
5. 2. Experimental Procedure	55
5. 3. <i>In-Situ</i> Bending Experiments	55
5.3.1 Buckling Characteristics	57
5.3.2 Quantitative Correlation of Buckling and Nanotube Characteristics	59
5. 4. Conclusion	61
6 -FIELD EMISSION AND STRAIN-ENGINEERING OF ELECTRONIC PROPERTIES IN BORON NITRIDE NANOTUBES	63
6.1 Introduction	63
6.2 Materials and Methods	64
6.3 Materials and Methods	65
6.3.1 Strain Engineering of Electrical Conductivity in BNNTs	65
6.3.2 Field Emission Properties	68
6.4 Conclusion	72

7 - <i>IN-SITU</i> TEM MONITORING OF THERMAL DECOMPOSITION IN INDIVIDUAL BORON NITRIDE NANOTUBES	73
7.1 Introduction	73
7.2 Experimental Procedure.....	74
7.3 Results and Discussion	75
7.4 Conclusion	81
8 - <i>IN-SITU</i> ELECTROCHEMICAL LITHIATION/DELITHIATION OBSERVATION OF INDIVIDUAL AMORPHOUS SI NANORODS	82
8.1 Introduction	82
8.2. Experimental Procedure.....	84
8. 3. Results	84
8.3.1 Selective Lithiation of Si NRs	84
8.3.2 <i>In-Situ/Ex-Situ</i> Phase Transformation during Lithiation	88
8.3.3 The Effect of Contact Area in Ionic Liquids-Nanorods Interfaces.....	90
8.3.4 <i>In-Situ</i> Delithiation Process	92
8.4 Conclusion	94
9 -REAL-TIME OBSERVATION OF LITHIUM FIBERS GROWTH INSIDE A NANOSCALE LITHIUM-ION BATTERY	95
9.1 Introduction	95
9.2. Experimental Procedure.....	96
9.3. Results	96
9.4. Conclusion	100
10 -DISCUSSION	101
10. 1. <i>In Situ</i> Mechanical Characterizations of BNNTs	101
10. 2. <i>In Situ</i> Electrical Characterizations of BNNTs.....	102
10. 3. <i>In Situ</i> Electrochemical Lithiation/Delithiation of Si Nanorods.....	104
11 -Conclusions	106
12 -Future Works.....	108
12. 1. Chemical Effect on the Mechanical Properties of BNNTs.....	108
12. 2. Chemical Effect on the Electrical Properties of BNNTs.....	109
12. 3. <i>In-Situ</i> Electrochemical Characterizations of Cathode Materials.....	109
References.....	111
Appendix-A: BORON NITRIDE PHASES	127
Appendix-B: ON THE RELATIONSHIP BETWEEN TEMPERATURE AND CURRENT DURING JOULE HEATING EXPERIMENTS.....	128
Appendix-C: COPYRIGHT PERMISSIONS	129

LIST OF FIGURES

Figure 1.1 (a) schematic of a BN sheet to roll up and build a nanotube. (b) illustrates a single-walled BNNT. (c) low magnification of an individual multi-walled BNNT, indicating the presence of no contamination on the sample. (d) high-resolution bright-field image of a BNNT placed on the carbon coated grid.	20
Figure 2.1 (a) Schematic of synthesis process of BNNTs inside the furnace. (b) SEM image of as-grown BNNTs.....	26
Figure 2.2 (a) High resolution TEM image of a multi-walled BNNT. (b) The line intensity along the dashed line in (a) indicates that the distance between walls is around 0.35nm.	27
Figure 3.1 Schematic of a single wall BN nanotube	28
Figure 3.2 Thermal vibration can be used to estimate the elastic properties of a BN nanotube. ¹³ (Reprinted with permission from Solid-State Communications, 1998. 105(5): p. 297-300 Copyright 1998, Elsevier Science Ltd.)	30
Figure 3.3 RMS amplitude of oscillation as a function of position from the base. The solid line shows the best fit. ¹³ (Reprinted with permission from Solid-State Communications, 1998. 105(5): p. 297-300 Copyright 1998, Elsevier Science Ltd.)	31
Figure 3.4 Electric Field Induced Resonance method was used to measure the elastic properties of a BN nanotube. TEM images showing (a) A cantilevered BN nanotube with an outer diameter of 43 nm, an inner diameter of 12 nm, and a length of 9.75 mm, (b) the first mode of the BN nanotube, and (c) the second mode of the BN nanotube. The dotted lines in (b) and (c) are the analytical fit to the corresponding deflection contour of the resonances. ⁴¹ (Reprinted with permission from Applied Physics Letters, 2004. 84(14): p. 2527-2529 Copyright 2004, American Institute of Physics.)	32
Figure 3.5 Experimental setup for multi-cycle bending of BN nanotubes performed inside a high-resolution analytical transmission electron microscope (HRTEM).	

	The inset shows a TEM view of the setup. ¹⁴ (Reprinted with permission from Acta Materialia, 2007. 55(4): p. 1293-1298 Copyright 2007, Elsevier Ltd.)	33
Figure 3.6	The multi-cycle bending experiments on BN nanotubes inside a TEM. distortion of the tubular layers nanotube takes place (a and c), but the straight shape is recovered after reloading (b and d). ¹⁴ (Reprinted with permission from Acta Materialia, 2007. 55(4): p. 1293-1298 Copyright 2007, Elsevier Ltd.)	34
Figure 3.7	Schematic of the AFM-TEM holder. The inset on the right shows a TEM view of the framed area of an individual multi-walled BN nanotube. The position of the tube against the cantilever can be accurately attuned. ²⁸ (Reprinted with permission from Nano Letter, 2007. 7(7): p. 2146–2151. Copyright 2007, American Chemical Society.)	35
Figure 3.8	Force –piezo displacement curves obtained using a AFM-TEM holder. (a) shows the data for a thick BN nanotube; and (b) for thin BN nanotubes. ²⁸ (Reprinted with permission from Nano Letter, 2007. 7(7): p. 2146–2151. Copyright 2007, American Chemical Society.)	36
Figure 3.9	The energy difference ΔE versus the tensile strain ε for (5, 5) armchair and (10, 0) zigzag BN nanotubes. Here $\Delta E = E - E_{\text{perfect}}$ is the difference between the energy for systems with and without Stone–Wales transformation. SW formation occurs at tensile strains of 11.47% and 14.23% for (5, 5) armchair and (10, 0) zigzag BN nanotubes, respectively. ¹¹ (Reprinted with permission from Scripta Materialia, 2007. 57(7): p. 571–574. Copyright 2007, Elsevier Ltd.)	38
Figure 3.10	Variation of Young modulus with radius of BN nanotube and carbon nanotube. Young’s modulus decreases when the diameter of BN nanotubes increases from 7 Å for armchair and 10 Å for zigzag. ¹²	39
Figure 3.11	Young modulus as a function of diameter for carbon, BN nanotubes. Young’s modulus increases as the diameter increases. ⁶⁶	40

Figure 3.12 Young's modulus of BN nanotubes vs. the nanotube diameter for: (a) armchair BN nanotubes; and (b) zigzag BN nanotubes. Young's modulus is independent of the diameter as it exceeds 2 nm. ⁶⁷	41
Figure 3.13 Energy change relative to the initial geometry as a function of (a) bending angle $\Delta\theta$ and (b) twisting angle $\Delta\phi$ for (1) armchair (5,5) carbon nanotubes and (2) zigzag (17,0) BN nanotubes. Results show that required energy increases by increasing the bending angles, and at breaking point due to neck/crack formation, the required energy decreases. ⁶⁹	42
Figure 4.1 (a) High resolution TEM image of a multi walled BNNT. Scale bar is 5nm. (b) The line intensity along the dashed line in (a) indicates that the distance between walls is around 0.35nm.	45
Figure 4.2 Schematic of the in-situ AFM setup inside the TEM. BNNTs were placed on the Pd-Au wire and brought to contact with AFM cantilever through the movement of piezotube and sapphire ball.	46
Figure 4.3 In situ TEM observation shows small-angle ($\sim 65^\circ$) bending of an individual BNNT at 300nm displacement within 10s. Bending point (circled) appears near the middle of the nanotube and is fully recovered upon releasing the applied force. The images captured from the recorded video.	47
Figure 4.4 <i>F-D</i> curves during the cyclic bending deformation of an individual BNNT at deformation cycles of 1 and 10.	48
Figure 4.5 TEM images of a BNNT at the bended area reveal the mechanism by which the nanotubes accommodate high bending angles close to 65° . The compression, C, and tension, T, sides of the nanotube are schematically shown in the inset of (a). The dashed lines shown in (c) represent a tilt in atomic planes along a particular set of atoms.....	48
Figure 4.6 Process of fracture in an individual BNNT after the large-angle ($\sim 120^\circ$) bending cycles. (a) to (e) represent one cycle of bending. (f) to (i) showing nanotube breaking into two parts after pulling and stretching. (j) <i>F-D</i> plot represents the changes in force upon failure initiation and propagation during one cycle (a to e). Scale bars are 20 nm.	51

- Figure 4.7 (a)-(c) Manipulation of the broken BNNT on the left (1) using the broken segment on the right (2). (d) Cross-section view of the broken nanotube as marked in a circle. The empty area at the center represents the inner channel of the BNNT. Scale bars are 20 nm..... 52
- Figure 5.1 (a) Represents bending experiment of an individual multi-walled BNNT in contact with AFM tip (on left) and gold wire base (on right). (b) Free-body diagram of the bending experiment in (a) with analysis of associated forces. (c) The bent nanotube is shown and special pattern formation at the bent area is marked by arrows. (d) High Resolution (HR) TEM image of individual bent BNNT reveals that the special pattern consists of multiple rippling on the compressive side of nanotube..... 56
- Figure 5.2 Force-displacement plots of a BNNT under cyclic bending deformation. 57
- Figure 5.3 (a) HRTEM image of an individual BNNT shows typical V-shape buckles on compression side. (b) The line intensity across along the red line in (a) indicates that the average distance between walls is ~ 0.35 nm..... 58
- Figure 5.4 (a) Bright field TEM image of a buckled BNNT and the representative structural parameters r , h , and λ are shown. (b) The plot of buckling wavelength λ as a function of $(r.h)^{0.5}$ where several BNNTs (solid line) are compared with the available data on CNTs in the literature (dashed line). .. 60
- Figure 5.5 (a) Schematic of BN hexagon atomic arrangement in each shell before bending deformation. Arrow shows the direction of bond switching. (b) Top view of BN pentagon-heptagon pairs as a result of bending deformation. (c) A 2D schematic of ripples under two hypothetical scenarios. The ripples with wavelengths of λ_1 and $\lambda_2=2\lambda_1$ are shown for at total length of λ_2 . Thermodynamically unfavorable B-B and N-N bonds are higher in the small ripples in comparison to the large ripple. 61
- Figure 6.1 (a) The corresponding I - V curves of a BNNT under mechanical straining. The colored curves indicate the I - V data during progressive strain loading and the black curve (marked with a short arrow) shows the insulating behavior under no bending. (b) The TEM image of a BNNT in contact with STM tip (no

loading) corresponds to the black curve in (a). (c) and (d) The TEM images of BNNTs under the continues increase of mechanical straining, respectively. The bending curvatures of the BNNT increase due to higher mechanical straining. I - V curves 1 and 8 represent cases with the lowest to highest amount of bending.....	65
Figure 6.2 (a) Characteristic $\ln I$ - V data corresponding to the I - V curves shown in Figure 6.1a. Arrow from 1 toward 8 indicates the increase in the bending deformation. (b-d) represent the parameters of resistance, electron concentration and mobility of the bent BNNT as a function of mechanical straining.....	67
Figure 6.3 (a) the I - V curve represents the FE behavior of an individual BNNT shown in inset (1 st FE cycle). Scale bar is 200 nm. (b) The corresponding Fowler-Nordheim plot representing the field emission behavior shown in (a).	68
Figure 6.4 (a) Field emission behaviors of the BNNT at four consecutive measurements. (b&c) Arrows indicate the formation of black particles as a result of decomposition on the outer surface of BNNT.....	70
Figure 6.5 (a) The schematic represents the FE setup where there is a gap between the tip of the sample and STM tip. As shown, the sample is biased with negative voltage with respect to the STM tip. (b) Arrows indicate the formation of dangling B bonds. The nitrogen atoms leave the structure when the sample reaches to the decomposition temperature. (c) and (d) illustrate the formation of boron particles as the number of B atoms with dangling bonds is increased.....	71
Figure 7.1 (a) Schematic of the utilized STM-TEM sample holder. Sample mounted on Au wire approaches the STM tip via sliding on the sapphire ball. (b) Shows the electric circuit as the BNNT (inside the red circle) is connected to the STM tip and Au wire.....	74
Figure 7.2 (a, b) TEM images correspond to the process of inserting the STM tip into the nanotube to secure the electrical contact.....	75

- Figure 7.3 (a) TEM image of a BNNT connected across the Au wire and the STM tip. Scale bar is 200nm. (b) High resolution TEM image of the end of an individual BNNT shows that there is no amorphous layer or contamination outside or inside the nanotube. Scale bar is 5nm. (c) The inner-shell distances of a BNNT is determined as 0.35 nm, based on the intensity histogram obtained along the AB line in (b). 76
- Figure 7.4 (a) The typical I - V curve measured along individual BNNTs does not pass noticeable current under undeformed condition. (b) The strong absorption in UV-visible spectroscopy corresponds to the optical band gap of ~ 5.9 eV.¹⁷ Peak at 4.78 eV corresponds to intrinsic dark exciton absorption and the small peak at 3.7eV is suggested to be associated with the defect in BNNTs. 76
- Figure 7.5 Current flow as a function of duration of applied. Constant voltage of 100 V was applied to an individual nanotube. Current increases slightly in the beginning and increases more rapidly after 77 seconds. The sudden drop of current at 95 seconds corresponds to the disconnection of STM-BNNT-wire circuit due to the BNNT decomposition. (Inset) TEM image of showing the broken nanotube is attached to the STM tip. 78
- Figure 7.6 (a-f) High-resolution TEM images correspond to the process of nanoparticles formation during the thermal decomposition of BN nanotubes. Black arrows points toward the growth of nanoparticles on the outermost shell layers. Red arrows indicate the void formation in the outer shell of the BN nanotube and its propagation toward the inner shells. 79
- Figure 7.7 TEM images show variations in the density of nanoparticles during the thermal decomposition of a BN nanotube. Regions near the STM tip (a) with more particles indicate higher temperatures compared to zones further away from the STM tip (b and c). The locations of these TEM images are taken from different parts of the BNNT as schematically drawn in these images.. 80
- Figure 8.1 (a) Schematic of STM holder experimental setup. As the STM tip is positively biased, IL flows on the nanorods and Li ions diffuse into nanorods. (b)

Shows the low-magnification image during the lithiation experiment. The arrow indicates a droplet as the IL flows on the Si NR (the other arrow) from the STM side to the gold wire.	85
Figure 8.2 Snapshot series of lithiation process represents the swelling or radial straining at selective locations (indicated with red arrows) of a Si NR.	86
Figure 8.3 An amorphous Si NR in contact with the IL that has no Li content at (a) 0 min, (b) 10 min (c) 20 minutes, (d) 30 min, (e) 60 min. Insets in (a) and (e) show the diffraction pattern of the Si NR initially and after 1hr of experiment.	87
Figure 8.4 (a) An <i>in-situ</i> charged Si NR contains several particles of $\text{Li}_{22}\text{Si}_5$ phase marked by white arrows. Similar particle morphology was observed in the <i>ex-situ</i> fully charged Si NRs as shown in (b). (c) and (d) represent the HRTEM images of the $\text{Li}_{22}\text{Si}_5$ particles indicating the crystalline nature of the lithiated phase. The d spacing as shown in (d) measured to be 0.34 nm. (e) and (f) illustrate the electron diffraction patterns of the lithiated NRs in <i>in-situ</i> and <i>ex-situ</i> experiments, respectively.	89
Figure 8.5 (a) An individual Si NR that is in contact with the IL before lithiation. The Li ion diffusion is along the axis of the nanorod. Image in (b) shows the NR after lithiation process with straining of ~10% in diameter. (c) Individual Si NR in contact with IL from the side surface. The thickness of the NR was measured to be 26nm before the lithiation and high resolution image (inset) shows the amorphous structure of NR before lithiation. (d) After the lithiation process, the diameter of NR expanded to 70nm. Inset shows a high-resolution image of $\text{Li}_{22}\text{Si}_5$ particles formed as a result of lithiation.	91
Figure 8.6 Schematics of two cases of interactions at IL-NR interfaces are shown. Schematic (a) illustrates the case where IL is in contact with the tip of a Si NR. Schematic (b) represents a case where the sides of NR are dipped into the IL.	92
Figure 8.7 (I-a to I-c) <i>In-situ</i> lithiation of an individual Si nanorod. Images on (I-b) and (I-c) represent the formation of $\text{Li}_{22}\text{Si}_5$ after 20 and 30 min, respectively. The arrow in Image (I-c) indicates a crack formed on the surface of Si NR during	

lithiation process. (II-a to II-c) The delithiation process is shown. The white arrow in image (II-a) points to a $\text{Li}_{22}\text{Si}_5$ particle that disappears during delithiation process as shown in (II-b) and (II-c). In addition, a crack closure can be seen by comparing the images (II-a) and (II-c) and tracking the black arrow..... 93

Figure 9.1 (a) A schematic of the in-situ lithiation setup is shown where the anode is placed on the STM and the IL is placed on the cathode. (b) The TEM image shows a nano-battery configuration in which the Si NRs are in contact with the ILs prior to the lithiation experiment. (c) The formation of a thin layer of ILs on the surface of ILs (the darker region) is shown. (d) The TEM image of Si NR structure after 1hr of lithiation. Arrows indicate the $\text{Li}_{22}\text{Si}_5$ particles that are formed. Inset represents a diffraction pattern of the lithiated Si NR indicating the presence of the $\text{Li}_{22}\text{Si}_5$ phase. 97

Figure 9.2 (a) Represents a typical surface of ILs prior to the lithiation process; the EDP in the inset shows no crystalline ordering can be found within the IL. (b) The nucleation of Li fibers during the lithiation process. The EDP in the inset indicates the crystalline ordering within the IL. (c-g) Series of snapshots taken from the real-time video indicate the appearance of the Li fibers at various stages. The inset shows that the newly formed fibers have crystalline orders. 98

Figure 9.3 (a) Black arrows indicate an individual NR surrounded by IL. (b) Arrows indicate the formation of Li islands on the NR. (c) Represents the growth of Li fibers. (d) The formation of kinks and growth of Li fibers are marked by black arrows..... 99

Figure A. 1 Schematics of different phases of BN structures corresponding to (a) hBN, (b) wBN, (c) rBN and (d) cBN. (Reprinted with permission from Phys. Rev. B 50, 7884–7887 (1994) . Copyright 1994, American Physics Socieity Ltd.) DOI: 10.1103/PhysRevB.50.7884.....127

Figure B. 1 Plot of increase in temperature as a function of current density.....128

LIST OF TABLES

Table 1.1 Represents the reported mechanical, electrical and thermal properties of different BNNTs available in the literatures.	21
Table 1.2 Represents the reported mechanical, electrical and thermal properties of different BNNTs available in the literatures.	22
Table 4.1 The estimated structural parameters for five different BNNTs and the calculated Young's modulus and standard deviation are shown.	50

Preface

The publications presented in this thesis have been part of research work carried out at Michigan Technological University, during my PhD in the period of 2009-2011. Electrical, mechanical and electrochemical characterizations of one-dimensional nanostructures are studied.

Chapter 3 presents an overview on the mechanical properties of BN nanotubes. In this chapter reported results, including experimental and simulation studies, on both multi-walled and single-walled BNNTs are discussed.

Chapter 4 presents the real-time fracture detection of individual boron nitride nanotubes in sever cyclic deformation processes, using *in-situ* techniques. Experiments were designed and conducted by Mr. Ghassemi. Samples were also prepared by Mr. Ghassemi under supervision of Dr. Chee Huei Lee (Department of Physics, MTU).

Chapter 5 presents *in-situ* observation of reversible rippling in multi-walled boron nitride nanotubes. A model is proposed for the mechanism of rippling formations and disappearance under bending deformation. Experiments were designed and conducted by Mr. Ghassemi. Samples were also prepared by Mr. Ghassemi under supervision of Dr. Lee.

Chapter 6 presents the field emission and strain-engineering of electronic properties in boron nitride nanotubes, using *in-situ* microscopy. Different experiments were designed and conducted by Mr. Ghassemi. Samples were also prepared by Mr. Ghassemi under supervision of Dr. Lee.

Chapter 7 presents the *in-situ* TEM monitoring of thermal decomposition in individual boron nitride nanotubes. Several experiments were designed and conducted by Mr. Ghassemi. Samples were also prepared by Mr. Ghassemi under supervision of Dr. Lee.

Chapter 8 presents the *in-situ* electrochemical lithiation/delithiation observation of individual amorphous Si nanorods. Different experiments were designed and conducted by Mr. Ghassemi. Anode materials were prepared by Dr. Au; ionic liquid materials were prepared by Mr. Ning and Dr. Heiden.

Chapter 9 presents real-time observation of lithium fibers growth inside a nanoscale lithium-ion battery. Different experiments were designed and conducted by Mr. Ghassemi. Anode materials were prepared by Dr. Au; ionic liquid materials were prepared by Mr. Ning and Dr. Heiden.

Acknowledgments

I would like to express my great appreciation to Dr. Reza Shahbazian-Yassar, for his guidance, constant support, and encouragement over the course of this study. I would also like to thank Dr. Yoke Khin Yap, Dr. Gregory M. Odegard, and Dr. Denis Meng for serving as my committee members.

Additional thanks go to Dr. A. Asthana, A. Pakzad, Q. Gao, N. Parikh, our nanoscience research group, who have helped me through my research and study at Michigan Technological University.

Special thanks go to C. H. Lee from the Physics Department and O. Mills from Materials Science Department for their collaboration and help.

I gratefully acknowledge the financial support from Mechanical Engineering-Engineering Mechanics department of Michigan Technological University.

Hessam Ghassemi,

Michigan Technological University, Nov. 2011

Abstract

One-dimensional nanostructures initiated new aspects to the materials applications due to their superior properties compared to the bulk materials. Properties of nanostructures have been characterized by many techniques and used for various device applications. However, simultaneous correlation between the physical and structural properties of these nanomaterials has not been widely investigated. Therefore, it is necessary to perform *in-situ* study on the physical and structural properties of nanomaterials to understand their relation. In this work, we will use a unique instrument to perform real time atomic force microscopy (AFM) and scanning tunneling microscopy (STM) of nanomaterials inside a transmission electron microscopy (TEM) system. This AFM/STM-TEM system is used to investigate the mechanical, electrical, and electrochemical properties of boron nitride nanotubes (BNNTs) and Silicon nanorods (SiNRs).

BNNTs are one of the subjects of this PhD research due to their comparable, and in some cases superior, properties compared to carbon nanotubes. Therefore, to further develop their applications, it is required to investigate these characteristics in atomic level. In this research, the mechanical properties of multi-walled BNNTs were first studied. Several tests were designed to study and characterize their real-time deformation behavior to the applied force. Observations revealed that BNNTs possess highly flexible structures under applied force. Detailed studies were then conducted to understand the bending mechanism of the BNNTs. Formations of reversible ripples were observed and described in terms of thermodynamic energy of the system. Fracture failure of BNNTs were initiated at the outermost walls and characterized to be brittle. Second, the electrical properties of individual BNNTs were studied. Results showed that the bandgap and electronic properties of BNNTs can be engineered by means of applied strain. It was found that the conductivity, electron concentration and carrier mobility of BNNTs can be tuned as a function of applied stress. Although, BNNTs are considered to be candidate for field emission applications, observations revealed that their properties degrade upon cycles of emissions. Results showed that due to the high emission current density, the

temperature of the sample was increased and reached to the decomposition temperature at which the B-N bonds start to break.

In addition to BNNTs, we have also performed *in-situ* study on the electrochemical properties of silicon nanorods (SiNRs). Specifically, lithiation and delithiation of SiNRs were studied by our STM-TEM system. Our observations showed the direct formation of $\text{Li}_{22}\text{Si}_5$ phases as a result of lithium intercalation. Radial expansion of the anode materials were observed and characterized in terms of size-scale. Later, the formation and growth of the lithium fibers on the surface of the anode materials were observed and studied. Results revealed the formation of lithium islands inside the ionic liquid electrolyte which then grew as Li dendrite toward the cathode material.

Chapter 1 -INTRODUCTION

1. 1. One-Dimensional Nanostructures

Nanomaterials, structures with at least one dimension below 100nm, have received a growing interest due to their superior properties in comparison to their bulk counterparts.^{1,2} For instance, Agrawal *et al.*³ reported the elastic modulus of ZnO nanowires increases from 140 to 160 GPa as the diameter of the nanowires decreases from 80 to 20 nm. By comparing nanomaterials with bulk, one can notice that the surface area to volume ratio increases significantly and becomes more important than the morphology. In another word, a nanowire, for instance, has a higher portion of its atoms on the surface compared to a bulk wire. This is very important factor for critical applications involving catalyst applications,⁴ chemical⁵ and gas sensors.⁶ Takagi⁷ also reported for the first time that decreasing in the crystal size can reduce the melting temperature compared to that of the bulk. These results promised various types of applications of one-dimensional nanomaterials in nanodevices.

One-dimensional nanostructures introduced new aspects to the materials applications. For instance, carbon nanotubes (CNTs) are one of the best reinforcement candidates to enhance the stiffness and fracture toughness of epoxy matrices by addition of only 0.1wt%.⁸ Investigation showed that Zn nanowire arrays showed size-dependent melting behavior due to the heat of fusion change with the change of the diameter.⁹ Therefore by utilizing these properties, one can modify nanostructures to build new devices.

This project is mainly focused on two types of one-dimensional nanostructures; boron nitride nanotubes (BNNTs) and silicon nanorods (Si NRs). Mechanical, electrical, thermal, and electrochemical properties of BNNTs and Si NRs were characterized using *in-situ* TEM techniques. In below sections, we briefly described the important properties and terminology that has been used for the characterization of these nanotubes and nanorods.

1.1.1 Boron Nitride Nanotubes

Boron nitride nanotubes (BNNTs) are one of the most attractive one-dimensional materials that have similar structure to CNTs.¹⁰ Similar to CNTs their morphology is hexagonal, as shown in Figure 1.1a, and it can be indexed based on the chiral vector. To build a nanotube, one can roll up a sheet of BN. Therefore, as indicated in Figure 1.1a, the sheet can be rolled along the R direction from point A to point B . If R lies along the Armchair line, then the nanotubes chirality is Armchair. If the wrapping angle, φ , is equal to 30° , then the nanotubes is called Zigzag, and when $0 < \varphi < 30$, the nanotubes is called chiral. One can also observe that every boron atom is surrounded by six nitrogen atoms. Figure 1.1a represents three different types of chirality that can be obtained for BNNTs including, zigzag, armchair or chiral. Figure 1.1b depicts a single-walled BNNT and in Figure 1.1c an individual multi-walled BNNT is shown.

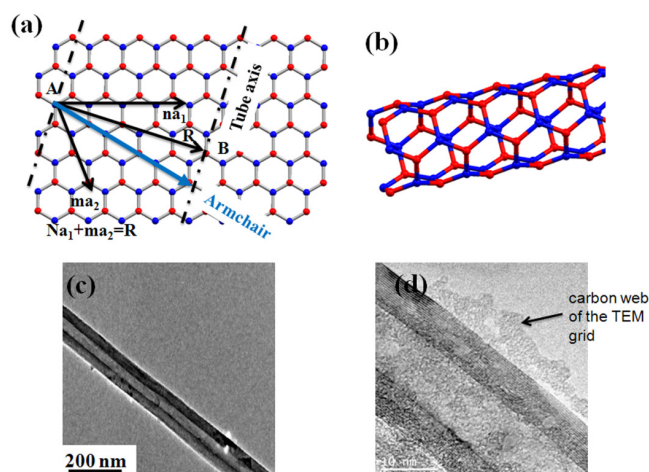


Figure 1.1 (a) schematic of a BN sheet to roll up and build a nanotube. (b) illustrates a single-walled BNNT. (c) low magnification of an individual multi-walled BNNT, indicating the presence of no contamination on the sample. (d) high-resolution bright-field image of a BNNT placed on the carbon coated grid.

Replacing the strong covalent sp^2 bond between carbon atoms by B-N bond is the main reason that their properties are different than those of their counterpart. Note, since the number of electrons in B-N bond is similar to that of the C-C bond, boron nitride structures have covalent structures with certain degree of ionic properties. For example, theoretical^{11,12} and experimental^{13,14} results showed that the Young's modulus of the

BNNTs is slightly lower than that of the CNTs. Interestingly, BNNTs show insulating behavior, which can be tuned upon filling the nanotube by conductive elements. Therefore, they can be used as strong coating layer for soft conductive materials for different purposes and applications.¹⁵ A summary of their mechanical, electrical and thermal properties reported in the literature is listed in Table 1.1.

Different BN structures such as, single-walled,¹⁶ multi-walled¹⁷ and doped BNNTs¹⁸ were synthesized using various techniques. Similar to carbon, nanostructures such as BN fullerene¹⁹ and BN nanosheet²⁰ were also observed. Arc-discharge²¹ and chemical vapor deposition²² are among the most common synthesis methods. However, techniques such as substitution reaction,²³ where CNT is used as a template, and laser ablation²⁴ are common as well.

BN nanosheets, for instance, can be deposited on various types of nanowires to form special cold electron field emitters.²⁵ BN fullerene²⁶ can be react with CO molecules and lead to formation of CO₂. Similar to carbon fullerene,²⁷ BN fullerene can also be used to store different nanomaterials for various purposes. Considering advantages that BNNTs possess over their counterpart, one can propose broad type of applications.

Table 1.1

Represents the reported mechanical, electrical and thermal properties of different BNNTs available in the literatures.

Sample	Multi-walled	Single-walled
Young's modulus	0.5-0.6 TPa ^{14,28}	1-1.2 TPa ^{11,12}
Bandgap	5.4 ²⁹ -5.9 ¹⁷	-
Thermal conductivity	18 W/mK ³⁰	-

1.1.2 Silicon Nanowire/Nanorods

Silicon is the most abundant element after oxygen in the universe and possesses remarkable characteristics. Due to its semiconducting properties, it is attractive for different industrial proposes such as solar cells,³¹ nanoelectronic devices.³² Hochbaum *et al.*³³ reported enhancement of thermoelectric performance of Si nanowires compared to that of the bulk. The significant improvement in the thermal conductivity is explained in terms of fundamental physics of heat transfer in the one-dimensional nanostructure of Si. Table 1.2 compares reported range of the Young's modulus, resistivity and thermal conductivity of Si bulk with those of the nanowires.

Table 1.2

Represents the reported mechanical, electrical and thermal properties of different BNNTs available in the literatures.

Sample	Young's modulus (GPa)	Resistivity (Ω .cm)	Thermal conductivity (W/m.K)
Si Bulk	170 ³⁴	0.64 ³⁵	241 ³⁶
Si NWs	93-250 ³⁷	0.01 ³⁸	5-50 ³⁹

Another potential application for Si is in lithium-ion batteries, to replace the carbonaceous anodes, which are used in the common batteries. The fundamental reason behind that is that each Si atom can accommodate up to 4.4 Li atoms ($\text{Li}_{22}\text{Si}_5$),⁴⁰ while in graphite each carbon atom can accommodate 1/6 Li atom (LiC_6).

1. 2. The Order of Chapters in This PhD Dissertation

In order to study mechanical and electrical properties of BNNTs, as described in Chapter 2, thermal chemical vapor deposition (CVD) technique were used to prepare our samples. CVD technique does not require dangerous chemicals precursor and can be operated in a conventional tube furnace at relatively lower temperature. High-resolution TEM images confirmed the high quality and concentration of the products.

Previous studies^{13,41} have shown that Young's modulus of BNNTs is comparable to that of the CNTs. However, some degree of difference in mechanical properties due to change in electronic structure of BNNTs is expected. Replacing strong covalent sp^2 bond between carbon atoms by B-N bond is the main difference between BNNTs and CNTs. Several experimental and computational methods are used to explain the mechanical properties of BNNTs, yet the results have not been systematically compared. In Chapter 3, we conducted a thorough literature review to better understand the prior works on the mechanical properties of BNNTs from both experimental and theoretical perspectives. We realized that there is lack of detailed studies on the underlying mechanisms responsible for high mechanical flexibility of BNNTs. To further analyze and characterize the mechanical response of BNNTs under cyclic loading and to reveal the structural details responsible for their high flexibility, a series of in-situ mechanical experiments were performed on multi-walled BNNTs. In Chapters 4 and 5, the multi-walled BNNTs were subjected to bending deformations at two ranges of $\alpha < 60^\circ$ and $\alpha > 120^\circ$. We found out that when $\alpha < 60^\circ$, BNNTs recovered their original shape upon removing the applied force. The high-resolution TEM images revealed that bent BNNTs form multiple rippling upon buckling, by which the nanotubes can accommodate the applied deformation. However, upon bending curvature of $\alpha > 120^\circ$, structural failure was observed after several cyclic loadings.

The surprising high mechanical flexibility of BNNTs means that they can be used in future micro-and nano-electronic devices, however the effect of mechanical straining on electrical properties of nanotubes was not quantified. Therefore, in the next step, the electronic conductivity of BNNTs was studied as a function of applied mechanical straining. Although, BNNTs are considered to be electrically insulator (due to a wide band gap of 5.4-5.9 eV), theoretical simulations predict that their electronic properties can be tuned by means of mechanical deformation.⁴² *In-situ* TEM studies⁴³ confirmed that under applied force the insulating characteristics of BNNT converts to semiconducting. However, no quantitative study had been performed to correlate the amount of mechanical strain and the changes in the electrical conductivity of the nanotubes. In Chapter 6, the current-voltage behavior of BNNTs was studied under

various amount of bending deformation and a metal-semiconductor-metal model was used to retrieve the electrical resistance, resistivity, mobility, and carrier concentrations in deformed BNNTs. By engineering the electrical properties of BNNTs, they can also become a superb candidate for field emission (FE) applications.⁴⁴ *In-situ* FE experiments conducted by Cumings *et al.*⁴⁵ on individual BNNTs showed stable current at high bias voltages. However, the stability of emission current under multi-cycle measurements is not studied. Since long-term emission stability is one of the major factors that preventing practical applications of nanotubes,⁴⁶ it is thus important to further understand the performances of BNNTs for potential applications in flat panel displays. In Chapter 6, a detailed study on the stability of emission current during cycles of FE experiments were also performed. The TEM analysis of the FE cycled nanotube revealed the likelihood of structural decomposition that can explain the reduction in the field enhancement factor.

In addition to their high mechanical flexibility, the thermal stability of BNNTs is also remarkable. In fact, one of the superior properties of BNNTs is their high decomposition temperature, $\sim 1000^\circ\text{C}$, while CNTs decompose at $\sim 500^\circ\text{C}$.²² Hence, in Chapter 7, *in-situ* Joule heating experiments were conducted to characterize the decomposition mechanism at relatively high temperatures. HRTEM showed that the decomposition failure occurs due to the dissociation of atomic structure resulting in the formation of nanoparticles with different sizes and population density.

In addition to electromechanical and thermal characterizations, *in-situ* electrochemical studies can be conducted inside TEM chamber. In Chapter 8, a simple nanobattery was constructed to mimic the true electrochemical reactions that occur inside a lithium-ion battery. Lithium-ion batteries have had a huge impact on our daily life. Silicon is one of the most promising replacements for the current carbonaceous anode materials in lithium-ion batteries. The problem, however, with silicon anode materials is that they expand and shrink excessively during charging-discharging cycles.⁴⁷ Over several life-cycles, this process leads to formation of crack and eventually capacity fading. In contrast to bulk Si anode, recent studies⁴⁸ showed that Si nanowires/nanorods accommodate the volume expansion without significant structural failure. The one-dimensional morphology of nanowires is expected to better accommodate with lateral

strains generated upon Li^+ intercalation. *In-situ* electrochemical studies were conducted in Chapter 8 to investigate the intercalation of lithium atoms into amorphous Si NWs. The results confirmed the direct formation of $\text{Li}_{22}\text{Si}_5$ phase due to intercalation of Li-ions as well as radial straining.

Aside from the capacity concern of the anode materials, safety of the lithium-ion batteries is also a key issue. After several charging-discharging cycles, a short circuit can be created between the cathode and anode due to the formation of lithium dendrite on the anode surface.⁴⁹ In a severe case, when a high rate of overcharging is applied to the cell, it can catch fire or even explode.⁵⁰ Therefore, in Chapter 9, *in-situ* experiments were conducted to understand the mechanism of dendrite formation and growth. Our observations revealed the formation of lithium islands inside the ionic liquid electrolyte. These islands continued to grow as Li dendrite toward the counter electrode parallel to the applied electric field.

Chapter 2 -EXPERIMENTAL GROWING METHOD

As mentioned earlier, several types of synthesis techniques can be used to produce BN nanostructures. These techniques are challenging and require very high growth temperatures ($>1500\text{ }^{\circ}\text{C}$), a specific fabrication system, or dangerous chemistry.^{21,22} BNNTs were synthesis for the first time by Chopra *et al.*,²¹ using arc-discharge technique. Later on, techniques such as laser ablation,²⁴ substitution reactions from CNTs⁵¹ and ball milling⁵² were developed to optimize the growth yield and reduce the impurity. The impurities include BN amorphous structure and several by product from the media.

Chemical vapor deposition (CVD) technique is another synthesis method which can be used to grow BNNT inside a furnace. Recently, BNNTs were grown without dangerous chemicals in a conventional tube furnace at relatively lower temperature.¹⁷ We grow these nanotubes under the supervision of Prof. Yap in Physics Department at Michigan Tech. These BNNTs are grown directly on Si substrates by thermal chemical vapor deposition at $1100\text{-}1200\text{ }^{\circ}\text{C}$, as shown schematically in Figure 2.1a.

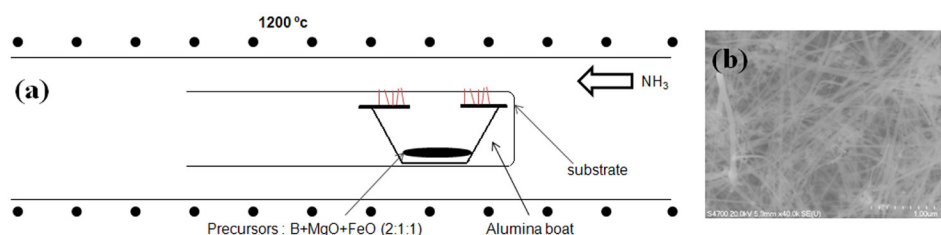


Figure 2.1 (a) Schematic of synthesis process of BNNTs inside the furnace. (b) SEM image of as-grown BNNTs.

Figure 2.1b shows the scanning electron microscope (SEM) image of the as-grown BNNTs. It can be seen that nanotubes are straight and a few micrometers long. Inside the furnace, B powder react with the MgO which results in the oxidation of boron in gas form in the reaction area, as shown in the reaction 1. Then, in the next step which is shown as reaction 2, the boron oxide gas react with the ammonia gas that is introduced into the furnace. The product of this reaction is BNNTs, which forms on top of the Si substrate placed on the boat, as shown in Figure 2.1.

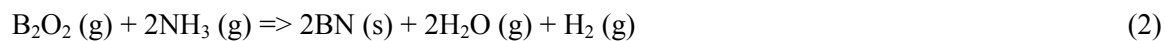


Figure 2.2*a* shows a high resolution TEM image of the wall structure in a multi-walled BNNT. The line intensity shown in Figure 2.2*b* along the dashed line (marked as *d*) in Figure 2.2*b* indicates that the distance between walls is around 0.35nm. The interlayer distance is in good comparison with the reported results in the literature.⁵³

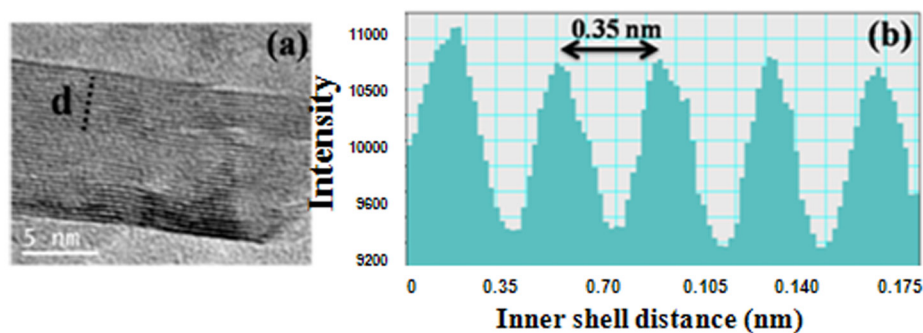


Figure 2.2 (a) High resolution TEM image of a multi-walled BNNT. (b) The line intensity along the dashed line in (a) indicates that the distance between walls is around 0.35nm.

Chapter 3 -ON THE MECHANICAL BEHAVIOR OF BORON NITRIDE NANOTUBES

The material contained in this chapter was previously published in the *Applied Mechanics Reviews* (Reprinted with permission from H. M. Ghassemi and R. S. Yassar, *Applied Mechanics Reviews* 63, 020804-1 (2010). Copyright 2010, ASME)

3.1. Introduction

The discovery of nanotubes has introduced new aspects of research experiments. A boron nitride (BN) nanotube has structural analogue similar to a carbon nanotube in nature, where alternating B and N atoms entirely substitute for C atoms in a graphitic-like sheet, as shown in Figure 3.1.

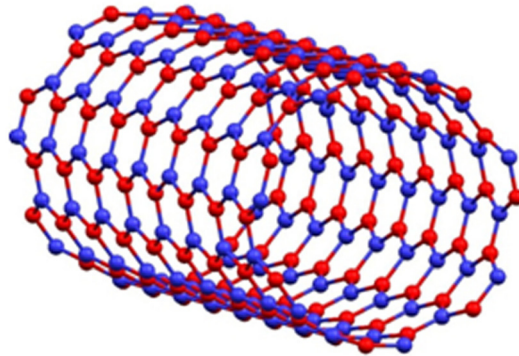


Figure 3.1 Schematic of a single wall BN nanotube

Different methods of BN nanotube synthesis are available such as arc-discharge,⁵⁴ laser ablation,⁵⁵ and substitution reaction.⁵⁶ But the most efficient method which is capable of synthesizing reasonable amount of BN nanotubes is chemical vapor deposition (CVD).⁵⁷ For pure carbon nanotubes, theoretical calculations predict that mechanical properties depend on radius and chirality of the nanotubes.⁵⁸ However, some degree of difference in mechanical properties due to change in electronic structure of BN nanotubes is expected. Replacing strong covalent sp^2 bond between carbon atoms by B-N bond is

the main difference between BN nanotubes and carbon nanotubes. BN nanotubes show a preference for zigzag lattice formation, since an atomic layer of B has considerably more surface energy than one comprised of N atoms.⁵⁹ In fact, due to presence of σ bonds in BN nanotubes, charge distribution between the B atoms and the nearest N atoms occurs. Therefore, the distribution of charge density along the BN nanotube is not uniform anymore. In addition, the effect of isolated electron pairs localized at the N atoms or localized π electronic states in BN nanotubes alternate for that of the delocalized π electronic states in carbon nanotubes. These differences between BN nanotubes and carbon nanotubes cause the differences in physical, chemical, and mechanical properties.⁶⁰ Another effect of the BN bonds may be destabilizing single-wall nanotube formation and strengthening so-called “lip–lip” interactions between adjacent layers in multi-walled BN nanotubes.⁶¹ So the mechanical properties of BN nanotubes can be predicted as well as those of carbon nanotubes.

Several experimental and computational methods have been used to explain the mechanical properties of BN nanotubes, yet the results have not been systematically compared. To the authors’ knowledge, this is the first review of mechanical properties of BN nanotubes. Our goal is to provide a better understanding on the relationships between mechanical properties and structural characteristics of BN nanotubes. A more thorough review on the electrical, optical, and thermal properties of BN nanotubes was discussed in a recent article,⁵³ hence they are not reviewed here.

3.2. Thermal Vibrations of BN nanotube

Chopra and Zettl¹³ were the first to measure the elastic modulus of individual BN nanotubes grown by the arc discharge method. The tests were performed inside a high resolution transmission electron microscope (HR-TEM) equipped with a thermal excitation apparatus. With the thermal vibration method, increasing the temperature of the specimen results in vibration. Figure 3.2 is a TEM image of two BNNTs during thermal vibration experiments. As shown, the tip of the longer one is not in focus, which is due to higher amplitude of the thermal vibration. This was verified by performing a focusing plane and rotation study. Figure 3.3 shows the root mean square (RMS)

transverse nanotube vibration amplitude in relationship to the distance from the base of the nanotube.

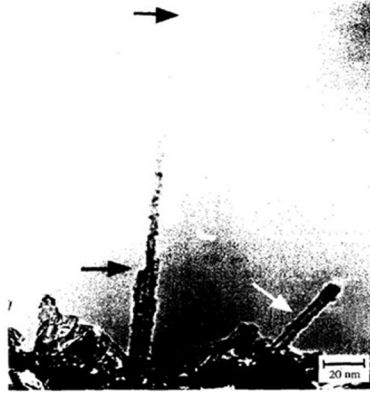


Figure 3.2 Thermal vibration can be used to estimate the elastic properties of a BN nanotube.¹³ (Reprinted with permission from Solid-State Communications, 1998. 105(5): p. 297-300 Copyright 1998, Elsevier Science Ltd.)

The magnitude and functional form of the vibration amplitude data of Figure 3.3 allowed measuring the elastic properties of BN nanotubes. The authors approximated the nanotube as a cantilever beam with a uniform circular cross section of outer diameter

$$\omega_n = (\beta_n L)^2 \sqrt{\frac{YI}{\mu L^4}} \quad (3-1)$$

where ω_n is the frequency, Y is the Young's modulus, and $\beta_n=1.8751, 4.6941, 7.8548, 10.996$ for $n=1, 2, 3, 4$ respectively. Furthermore, μ is the mass per unit length, I is the moment of inertia of the tube, and L is the beam length. From the fit in Figure 3.3 (solid line), the maximum RMS amplitude of oscillation was reported to be 0.8 nm . This fit, together with the measured dimensions of the nanotube, $a = 3.5 \text{ nm}$, $b = 2.2 \text{ nm}$ and $L = 153.8 \text{ nm}$, yields an elastic modulus of $Y = 1.22 \text{ TPa}$ for the BN nanotube at $T = 300 \text{ }^\circ\text{K}$. The uncertainties was estimated to be roughly 0.1 nm in a, b , and L . This led to an uncertainty in the absolute value of Y of order $\pm 20\%$. The Young's modulus BN nanotube was calculated to be 14 times greater than the measured in-plane modulus of

bulk hexagonal BN material. This difference can be because the tube has no defect while the bulk hexagonal material could be a composite of defected layers.

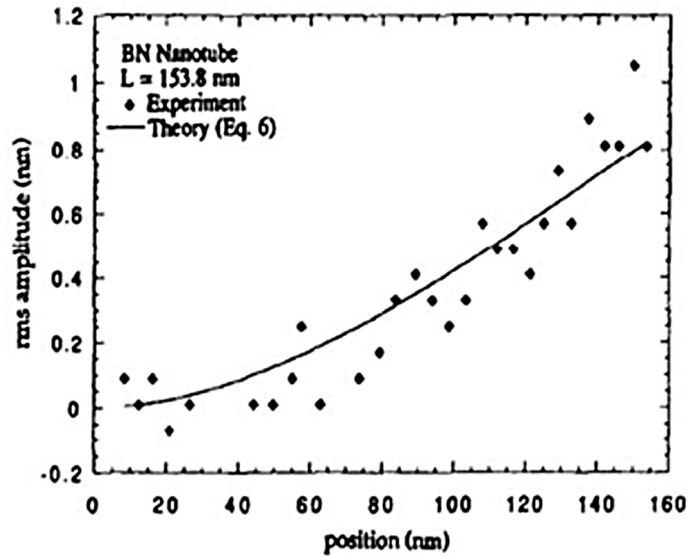


Figure 3.3 RMS amplitude of oscillation as a function of position from the base. The solid line shows the best fit.¹³ (Reprinted with permission from Solid-State Communications, 1998. 105(5): p. 297-300 Copyright 1998, Elsevier Science Ltd.)

Although this method can estimate the elastic modulus of BN nanotubes at different lengths, the main limitation is that this elastic modulus is calculated on the tip of the nanotube. Therefore, the elastic modulus is length dependent. In addition, the calculation is based on the distance from the fixed base, and other geometrical parameters, such as chirality, diameter of nanotube, and numbers of walls were not taken into account. Moreover, the applied method does not capture the force-displacement relationship in the tube and therefore no information can be obtained regarding the tensile strength and elongation to failure.

3.3. Electric Field Induced Resonance Method

Suryavanshi *et al.*⁴¹ measured the elastic modulus of BNNT grown by carbon free chemical vapor deposition (CVD) process. The authors used the electric field induced resonance method inside a TEM. The TEM sample holder was retrofitted with a manipulator integrated with a quadruple segmented piezoelectric tube. A tungsten (W) probe having a tip radius of less than 200 nm was used as the counter-electrode. A

sinusoidal AC signal was applied between the BNNT and the W probe. They conducted a detailed study on the elastic modulus and resonance behavior of BNNTs through the measurement of a set of 18 individual BNNTs. The diameters of the measured BN nanotubes ranged from 34 to 94 *nm*, and the lengths from 3.09 to 11.65 *mm*. First and second mode harmonic resonances of cantilevered BN nanotubes were induced, the resonance response curves were acquired, and the effective elastic modulus was deduced based on the classic beam mechanics following this equation;

$$E = \frac{64\pi^2 L^4 \rho}{(d_1^2 + d_2^2)} \left(\frac{f_i}{\beta_i^2} \right)^2 \quad (3-2)$$

where d_1 is the outer diameter, d_2 is the inner diameter, L is the cantilever length of the nanotube, β_i is a constant determined by boundary conditions, and f_i is the resonance frequency for the harmonic resonance mode i . For BN nanotube, the density of 2180 kg/m^3 was used, according to the density of hexagonal-BN.

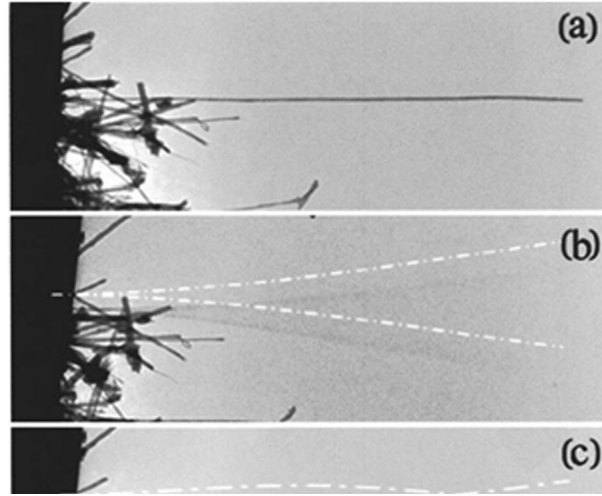


Figure 3.4 Electric Field Induced Resonance method was used to measure the elastic properties of a BN nanotube. TEM images showing (a) A cantilevered BN nanotube with an outer diameter of 43 nm, an inner diameter of 12 nm, and a length of 9.75 μm , (b) the first mode of the BN nanotube, and (c) the second mode of the BN nanotube. The dotted lines in (b) and (c) are the analytical fit to the corresponding deflection contour of the resonances.⁴¹ (Reprinted with permission from Applied Physics Letters, 2004. 84(14): p. 2527-2529 Copyright 2004, American Institute of Physics.)

Figure 3.4 shows the TEM images of the cantilevered BN nanotube with the modes of harmonic motions. The value of E from was obtained to be 722 GPa for a 34 nm diameter tube. According to the Equation 3-2, the elastic modulus E is proportional to L^4 , which makes the estimation of E to be responsive to the length measurement. This means that long nanotubes, in principal, should yield a higher elastic modulus in comparison to short tubes. However, the authors did not observe reliance of elastic modulus on the outer diameter and the length of the BNNTs (see Ref. 11, Figure 3.4). In addition, the simplifying assumption of classical cantilever mechanics might not be accurate for nanotube structures. Similar to the thermal vibration method, this technique does not provide much understanding of the tensile properties of nanotubes.

3.4. Multi-Cycle Bending Deformation

Golberg *et al.*¹⁴ conducted a series of multi-cycle bending deformation of an individual multi-walled BN nanotube inside a high-resolution TEM using a piezo-driven scanning tunneling microscope (STM) holder. Figure 3.5 shows the experimental setup. The BNNTs on a gold wire were inserted into the movable part (sapphire ball) of the piezo-driven side entry TEM holder.

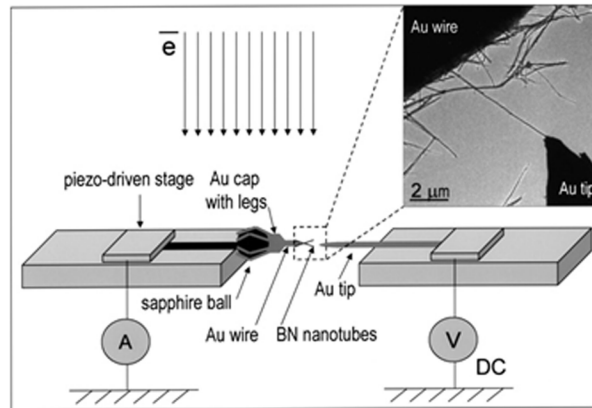


Figure 3.5 Experimental setup for multi-cycle bending of BN nanotubes performed inside a high-resolution analytical transmission electron microscope (HRTEM). The inset shows a TEM view of the setup.¹⁴ (Reprinted with permission from Acta Materialia, 2007. 55(4): p. 1293-1298 Copyright 2007, Elsevier Ltd.)

The authors conducted multi-cycle bending experiments on BN nanotubes where the bending angle could achieve $\sim 70^\circ$ (Figure 3.6). The authors reported that the pre-existing nanotube helicities did not influence the deformation. They also noticed that the BNNTs are highly flexible. The bending cycles could be performed at least twenty times without the observation of any failure in the BNNT. They contradicted the pre-existing belief about BNNT brittleness because the B-N bond is partially-ionic. Similar experimental⁶² and theoretical⁶³ measurements indicate high flexibility for carbon nanotubes, but this was not expected in BNNTs. Another discovery was that the nanotube deformed at the kink point, where, non-stoichiometric B-rich B_xN tetragonal phases were dominant. Figure 3.6 shows high resolution images of deformation kinks in the nanotubes. The only notable change in the nanotube morphology happened after numerous deformation cycles, where the BN filling phase was graphitized similar to a flattened condition.

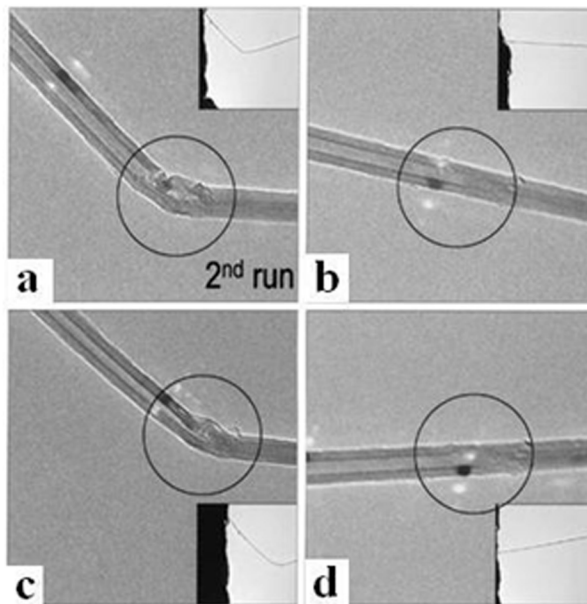


Figure 3.6 The multi-cycle bending experiments on BN nanotubes inside a TEM. distortion of the tubular layers nanotube takes place (a and c), but the straight shape is recovered after reloading (b and d).¹⁴ (Reprinted with permission from Acta Materialia, 2007. 55(4): p. 1293-1298 Copyright 2007, Elsevier Ltd.)

These experiments provided the first observation of deformation behavior in BN nanotubes; however, no quantitative data was reported on the force-displacement calculations. Therefore, the measured values of BNNT's mechanical properties remained unknown. The lack of such data motivated the authors to pursue the experiments with another setup that allowed the quantitative characterization of force-displacement data (see Section 3.5). The tests were limited to bending experiments and no information on tensile properties could be obtained.

3.5. Direct Force Measurement under Combined AFM and TEM

Golberg *et al.*²⁸ were the first to perform the direct force measurements under bending of Multi-Walled (MW)-BN nanotubes of various diameters. The force measurement experiments were carried out using an atomic force microscopy (AFM) holder, which was placed into the TEM (Figure 3.7). For AFM measurements, a silicon cantilever was attached to a fixed Microelectromechanical Systems (MEMS) force sensor, and an aluminum wire with a mounted BN nanotube sample was placed on the piezo movable side of the holder. The force reading was conducted by the piezoresistive properties of the Si cantilever enabling direct conversion of displacement values into force data. This allowed them to evaluate the bending stresses and to estimate the elastic modulus of individual BN nanotubes while monitoring the lattice changes during the deformation process.

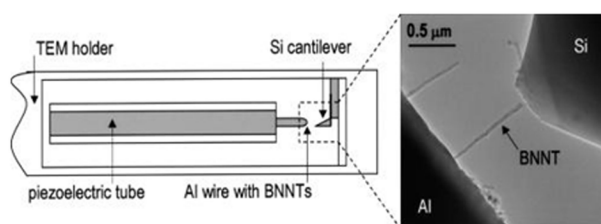


Figure 3.7 Schematic of the AFM-TEM holder. The inset on the right shows a TEM view of the framed area of an individual multi-walled BN nanotube. The position of the tube against the cantilever can be accurately attuned.²⁸ (Reprinted with permission from Nano Letter, 2007. 7(7): p. 2146–2151. Copyright 2007, American Chemical Society.)

The force-displacement curves during the deformation of a thick (100nm) and a thin tube (40 nm) are shown in Figure 3.8. The inset images demonstrate the bending process of BNNTs. The applied deformation forces for ~900 nm displacement were directly measured to be 900 nN and 300 nN for the thick and thin tubes, respectively.

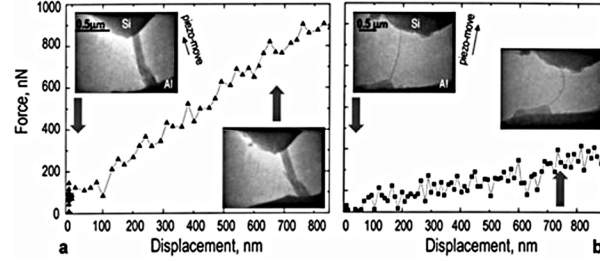


Figure 3.8 Force –piezo displacement curves obtained using a AFM-TEM holder. (a) shows the data for a thick BN nanotube; and (b) for thin BN nanotubes.²⁸ (Reprinted with permission from Nano Letter, 2007. 7(7): p. 2146–2151. Copyright 2007, American Chemical Society.)

The elastic modulus of the BN nanotube was also calculated using the Euler's formula:⁶⁴

$$F_{Euler} = \frac{\pi^2 EI}{L^2} I = \frac{\pi(d_2^4 - d_1^4)}{64} \quad (3-3)$$

where, L was the length of the BNNT between the two contacts, d_1 and d_2 were the internal and external BN nanotube diameters respectively, E was the elastic modulus, and F_{Euler} was the force applied. The values of the elastic modulus were found to be in the range of 0.5-0.6 TPa.

The in-situ deformation process allowed the authors to follow the sequence and time scale of the BN nanotube buckling/kinking phenomena that took place due to the applied large bending forces. It was observed that at bending angles more than 115° , a residual plastic buckle could remain in the structure of the tubes. This resulted in the formation of $\sim 30^\circ$ angled-kinks on BN nanotube after unloading. While at lower bending

angles kinks quickly disappeared in a spring-like fashion when the load was removed (Figure 3.6).

The in-situ experiments are difficult to perform due to the sliding of BNNTs over Si contact. This makes reliable statistical analysis of the data (including error analysis) rather difficult. Such sliding can only be prevented in the case of very tight physical contact between a tube and the mechanical clamps. In addition, the effects of high energy (300 kV) electrons on the BNNT defect formation were not fully ruled out. No tensile experiments were conducted; therefore, the tensile properties of the tubes remained unknown.

3.6. Modeling and Simulation of BN Nanotube Mechanics

Apart from experiments, a number of computational calculations have been conducted to estimate the mechanical properties of BNNTs. Song and Jiang¹¹ used a hybrid atomistic/continuum model based on inter atomic potentials for B and N, and studied the Stone-Wales (SW) transformation⁶⁵ in BN nanotubes subject to tension. SW transformations are topological defects which correspond to the 90° rotation of a B-N bond with respect to the center of the bond. The defect creates two pentagon-heptagon pairs. This model established an inter atomic potential based on:

$$V(r_{ij}; \theta_{ijk}) = V_R(r_{ij}) - B_{ij} V_A(r_{ij}) \quad (3-4)$$

where V_R and V_A are the repulsive and attractive pair terms that depend only on the distance r_{ij} between a pair of atoms i and j , and B_{ij} represents the multi-body coupling that depends on neighboring atoms through bond angle. It is used for atoms near the defect. The authors calculated differences between the energy level of a perfect nanotube (without any defects) and nanotubes with defects (shown as ΔE). Figure 3.9 illustrates the calculated ΔE versus the percentage of deformation. The SW transformation occurs and generates the 5-7-7-5 defects when the tensile strain reaches 11.47% for (5, 5) armchair and 14.23% for (10, 0) zigzag BN nanotubes. By comparing this information with the reversible cycling bending results¹⁴ discussed in Section 3.4, it can be concluded that no

SW formation develops when the BN nanotube bends in elastic region (below 70° angle), and, therefore, the bending is fully reversible. In other words, only at high angles of bending can SW formation be initiated.

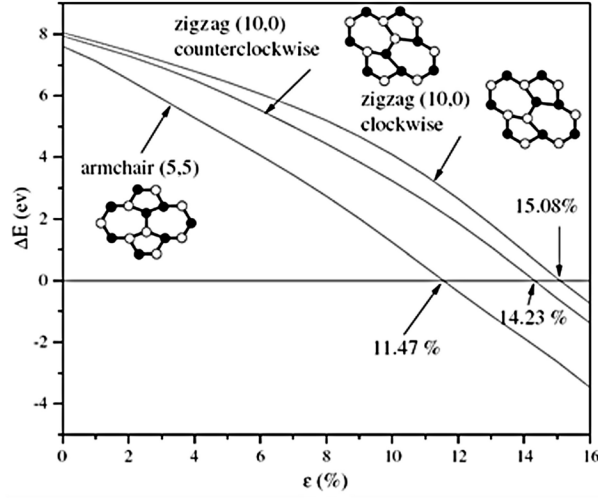


Figure 3.9 The energy difference ΔE versus the tensile strain ϵ for (5, 5) armchair and (10, 0) zigzag BN nanotubes. Here $\Delta E = E - E_{\text{perfect}}$ is the difference between the energy for systems with and without Stone–Wales transformation. SW formation occurs at tensile strains of 11.47% and 14.23% for (5, 5) armchair and (10, 0) zigzag BN nanotubes, respectively.¹¹ (Reprinted with permission from Scripta Materialia, 2007. 57(7): p. 571–574. Copyright 2007, Elsevier Ltd.)

Using the Tersoff–Brenner potential, Verma *et al.*¹² calculated that Young’s modulus for nanotubes with different diameters and observed dependency on nanotube chirality (Figure 3.10). The potential energy between the atoms i and j on the same tube separated by a distance r_{ij} is of the form

$$V(r_{ij}) = f_c(r_{ij})[f_R(r_{ij}) + b_{ij}f_A(r_{ij})] \quad (3-5)$$

where, f_c is a cut-off function. This form of cut-off is continuous and its derivative presents for any r $f_R(r) = Ae^{-\lambda_1 r}$ and $f_A(r) = -Be^{-\lambda_2 r}$. For further details see Ref. ¹². The authors reported an increase in Young’s modulus of BN and carbon nanotubes with

increases in diameter of both zigzag and armchair nanotubes up to certain diameter values. They also observed that when the diameter of BNNTs increased from 7 Å for armchair and 10 Å for zigzag, the Young's modulus decreased. This behavior was attributed to the poor and wavy shells of single-walled BNNTs. The ionic nature of the bonds between the B and N atoms gives rise to the decreasing of the Young's modulus upon increasing the diameter of the nanotube. This behavior was not observed for carbon nanotubes and the Young's modulus was reported to be independent of chirality. In addition, the results show that the Young's modulus of both zigzag and armchair carbon nanotubes are higher in comparison to the BN nanotubes. As explained earlier, the main difference between carbon nanotubes and BN nanotubes is in the type of bonding between the atoms. Since the Young's modulus is directly controlled by the strength of bonds, the covalent sp^2 bonds in carbon nanotubes are essentially stronger than B-N bonds.

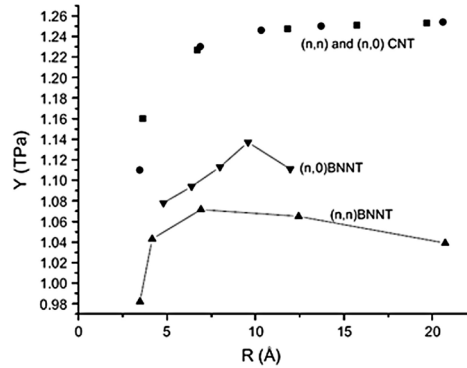


Figure 3.10 Variation of Young modulus with radius of BN nanotube and carbon nanotube. Young's modulus decreases when the diameter of BN nanotubes increases from 7 Å for armchair and 10 Å for zigzag.¹²

Hernández *et al.*⁶⁶ calculated the Young's modulus of BNNT in range of 0.8-0.9 TPa depending on diameter and chirality of nanotubes, using tight-binding methods. In their tight-binding scheme, the hopping integrals were used to construct the Hamiltonian. A minimal basis set corresponding to a single atomic-like orbital per atomic valence state was used. Young's modulus was calculated based on its conventional definition:

$$Y = \frac{1}{V_0} \frac{\partial^2 E}{\partial \epsilon^2} \quad (3-6)$$

where V_0 is the equilibrium volume and E is the strain energy. Their results, Figure 3.11, showed that the higher the diameter of nanotube, the greater the Young's modulus of nanotube.

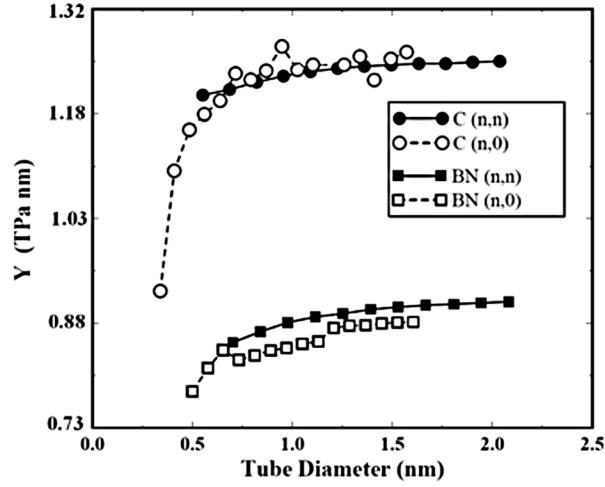


Figure 3.11 Young modulus as a function of diameter for carbon, BN nanotubes. Young's modulus increases as the diameter increases.⁶⁶

Song *et al.*⁶⁷ also found that the mechanical behavior of BN nanotubes does not depend on the diameter and length. The interatomic potential for boron and nitrogen was used to establish a continuum constitutive model for BNNTs via the modified Cauchy–Born rule.⁶⁸ Figure 3.12 shows Young's modulus of BN nanotube vs. the tube diameter for armchair (n, n) and zigzag (n, 0) BN nanotubes obtained from an atomistic-based continuum theory, based on Equation 3.6. The results were compared with atomistic-based continuum theory, tight binding, and ab initio [see the Ref. of ⁶⁷]. They observed that the Young's modulus is independent of the nanotube diameter at $d < 2$ nm. This is because the B–N bond length (~ 0.15 nm) is much smaller than the nanotube diameter (< 2 nm). Another explanation for this independence could be that at lower diameter sizes, bonds are more affected due to the curvature of the nanotube. In other words, for

nanotubes with large diameter, bonds are in a flat plane rather than being in a curved plane (wall of the nanotube).

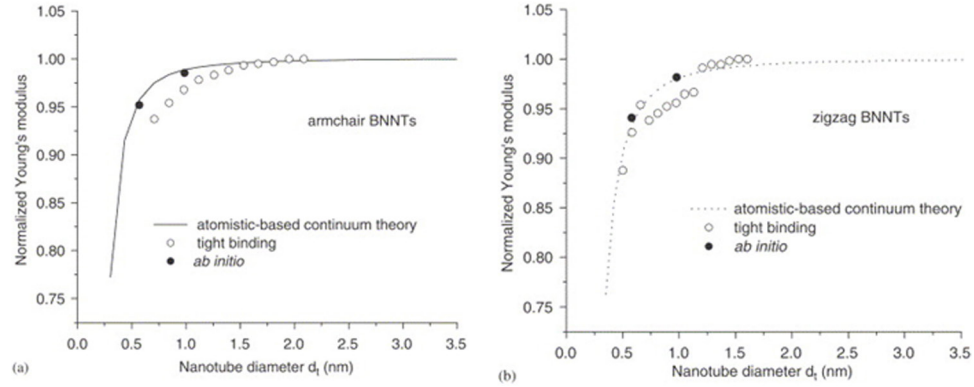


Figure 3.12 Young's modulus of BN nanotubes vs. the nanotube diameter for: (a) armchair BN nanotubes; and (b) zigzag BN nanotubes. Young's modulus is independent of the diameter as it exceeds 2 nm.⁶⁷

Enyashin and Ivanovskii⁶⁹ compared the atomic and energetic mechanism of bending and twisting of C with BN nanotubes using molecular dynamics. Their atomic models of tubes were obtained using a well-known algorithm (see Ref. ⁶⁹) by rolling planar graphitic and hexagonal BN sheets into seamless cylinders. Their results for bending, as shown in Figure 3.13a, show that to increase the bending angle, more energy is needed relative to the initial geometry for both carbon nanotubes and BN nanotubes. For carbon nanotubes, there is a significant decrease in energy at angles around 70° of bending where C-C bonds start to break. At the breaking range angle, C₆ rings convert to C₅ and/or C₇ rings, to maintain the energy state of the nanotube as low as possible, at each side of breaking. Therefore, this breaking point, which can act as a neck or initial crack, decreases the required energy for continuing the bending.

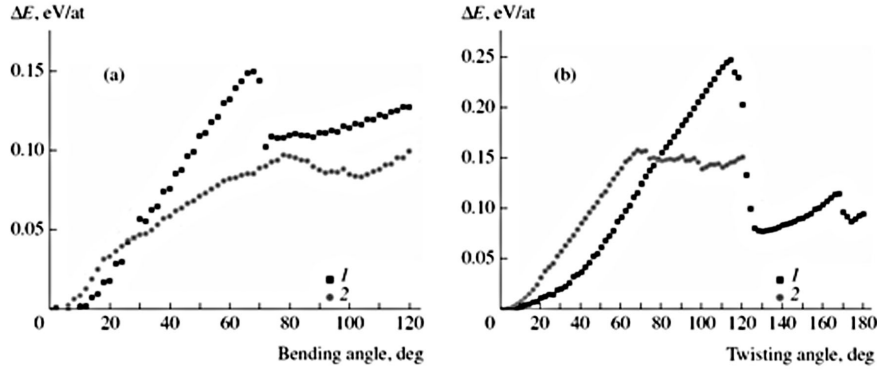


Figure 3.13 Energy change relative to the initial geometry as a function of (a) bending angle $\Delta\theta$ and (b) twisting angle $\Delta\phi$ for (1) armchair (5,5) carbon nanotubes and (2) zigzag (17,0) BN nanotubes. Results show that required energy increases by increasing the bending angles, and at breaking point due to neck/crack formation, the required energy decreases.⁶⁹

In case of B-N bonds breakdown at the necking point, the alternative bond should be either B-B or N-N, which are energetically unfavorable. Therefore, although the required energy for a given angle of bending is smaller for BN nanotube, the necking point starts at relatively higher angles. Breakdown of C-C bonds start at 65° while, that of B-N bonds happens at 85° . Effect of type of bonds becomes more significant in the twisting process. Figure 3.13b, shows that breaking of the bonds in twisting deformation require more energy than bending deformation. B-N bonds need more energy up to 60° angle of twisting; C-C bonds, however, can tolerate a higher twisting angle. There is again a breaking point for carbon nanotube and significant reduction in energy level. Unfavorable formation of B-B and/or N-N bonds prevents such sharp reduction, but mainly due to lower strength of the B-N bond, the breaking of the bonds starts at relatively lower angles.

3.7. Conclusion

Replacing strong covalent sp^2 bond between carbon atoms by B-N bonds and unfavorable B-B or N-N bonding give rise to differences in the mechanical behavior of BN nanotubes. Their Young's modulus was calculated to be in the range of 0.5-1.2 TPa from experimental tests and in the range of 1-1.2 TPa from theoretical calculations. The deformation experiments inside the electron microscope are ideal tests to tailor the

tubular lattice structural changes within an individual bent BN nanotube with an extremely spatial resolution to reveal the nanomechanical mechanisms. However, the effect of beam radiation should be taken into account. The cross linking between the walls due to beam radiation can affect the reported mechanical properties.⁷⁰ The BN nanotubes were found to be highly flexible and perfectly recover their original shape after 70° angle of bending. However, experiments at 120° bending angles resulted in 30° bending residuals in the nanotube structure. Theoretical calculations show higher mechanical property results for zigzag rather than armchair nanotubes which might be due to the number of bonds at a given length. Modeling results show that BN nanotubes neck at higher angles in comparison to carbon nanotubes due to unfavorable B-B or N-N bonding.

Chapter 4 -REAL-TIME FRACTURE DETECTION OF INDIVIDUAL BORON NITRIDE NANOTUBES IN SEVERE CYCLIC DEFORMATION PROCESSES

The material contained in this chapter was previously published in the *Journal of Applied Physics* (Reprinted with permission from H. M. Ghassemi, C. H. Lee, Y. K. Yap, and R. S. Yassar, *Journal of Applied Physics* 108, 1-1 (2010). Copyright 2010, American Institute of Physics)

4. 1. Introduction

Boron nitride nanotubes (BNNTs) possess lattice structures similar to carbon nanotubes (CNTs) but have a large theoretical band gap of ~ 5.5 eV.²⁹ These one-dimensional nanostructures are predicted to have exceptional mechanical properties and applicable for high strength composites. With respect to the experimental examination of mechanical properties of BNNTs, very few experiments have been performed to date. In order to enable the future application of BNNTs in future nano- or micro-scale devices, it is therefore important to understand the failure and deformation mechanisms of these nanotubes.

The authors of this manuscript recently conducted a thorough review on the theoretical and experimental understanding of BNNT's mechanics available in the literature.⁷¹ Theoretical studies predict that the Young's modulus of BNNTs can be up to 1.2 TPa.^{12,66} Experimentally, the Young's modulus was measured to be ~ 0.5 TPa using a direct force method,¹⁴ and ~ 0.8 TPa using the electric field induced resonance method.⁴¹ Theoretically, it was found that bending angle of $\sim 70^\circ$ can lead to failure or breaking of B-N bonds in pristine single-wall BNNTs.⁶⁹ Recently, Golberg *et al.*¹⁴ reported that at bending angles $\sim 115^\circ$, a residual plastic buckle could remain in the structure of the nanotube. This resulted in the formation of $\sim 30^\circ$ angled-kinks on BNNTs after unloading. We also recently studied the high temperature structural degradation of BNNTs.⁷² In the current research; we investigated the cyclic behavior of BNNTs as this had never been studied by previous researchers. Our objective was to understand the performance limits of BNNTs under severe bending condition.

4. 2. Experimental Procedure

We have studied the cyclic deformation of individual BNNTs under two different deformation regimes using small-angle ($\sim 65^\circ$) and large-angle ($\sim 120^\circ$) cyclic bending. Our experiments were conducted by atomic force microscopy (AFM) under *in-situ* monitoring using JEOL JEM-4000FX transmission electron microscopy (TEM) operated at 200 KeV. The reliability of such *in-situ* AFM/TEM measurements has been well-documented.^{14,15} Our BNNTs were directly deposited on Si substrates by thermal chemical vapor deposition at 1100-1200 °C in a conventional tube furnace. Precursor powders include MgO, Fe₂O₃ and pure B, and NH₃ were used as the source of Nitrogen. These BNNTs have a bandgap ~ 5.9 eV, which is higher than those used in previous reports (~ 5.4 eV), promising the high purity of sample.^{14,15} Figure 4.1 represents a high resolution TEM image of the synthesized BNNTs, and the line intensity shown in (b) along the dashed line in (a) indicates that the distance between walls is around 0.35 nm. Individual BNNTs were then attached on a Pd-Au wire by light mechanical scratching on the as grown samples. As a result of Van der Waals forces, individual nanotubes stick to the wire in different directions. The Pd-Au wire was then fixed on the Au hat, which sits on the sapphire ball. Applying friction force between hat legs and sapphire ball, the piezo-driven holder allows nanometer motion of the hat (which is actually the sample movement) toward the AFM tip (Figure 4.2). Using the *Nanofactory*TM software (NFC3), sample position was adjustable with a precision of 1 nm in *X*, *Y* and *Z* directions.

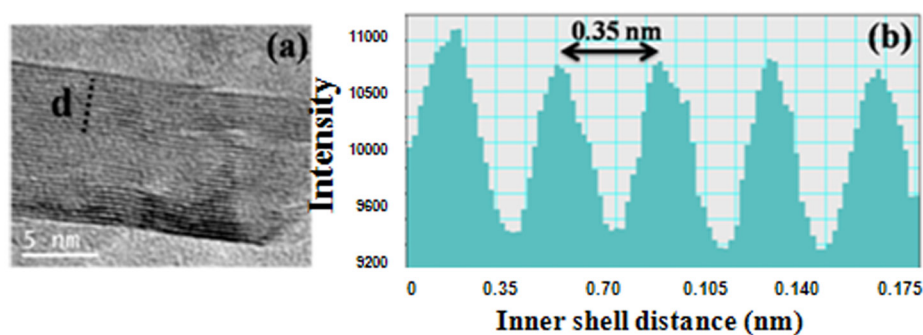


Figure 4.1 (a) High resolution TEM image of a multi walled BNNT. Scale bar is 5nm. (b) The line intensity along the dashed line in (a) indicates that the distance between walls is around 0.35nm.

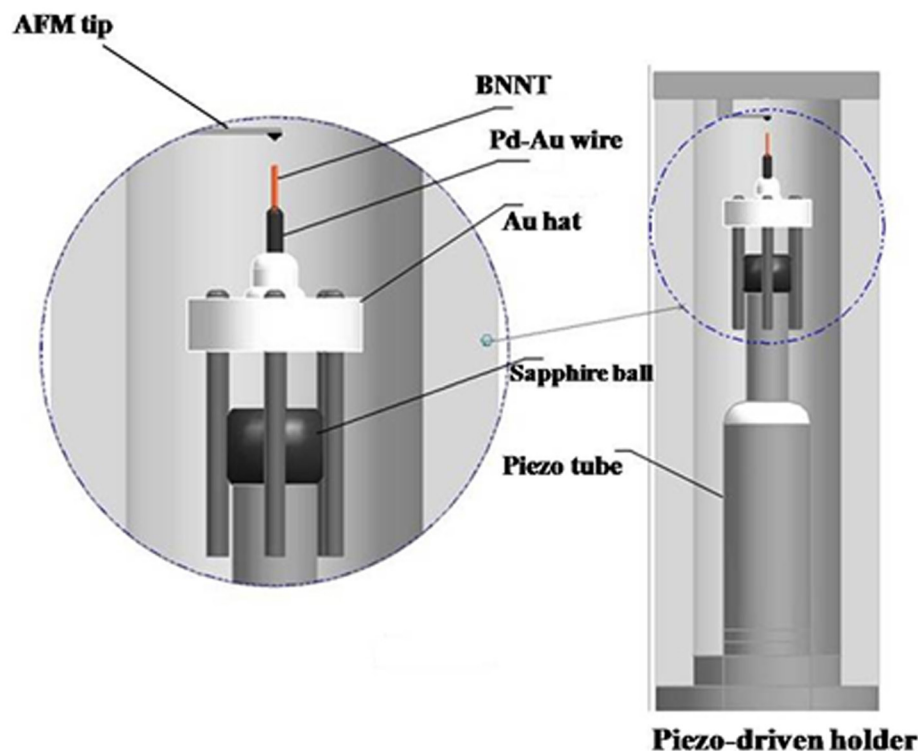


Figure 4.2 Schematic of the in-situ AFM setup inside the TEM. BNNTs were placed on the Pd-Au wire and brought to contact with AFM cantilever through the movement of piezotube and sapphire ball.

4. 3. Results and Discussion

Figure 4.3 shows the position of one individual BNNT (~ 50 nm in diameter) in contact with the AFM tip before, during and after the bending process. The nanotube was bent at the vicinity of the center, suggesting that there was no imperfection or filled part on the nanotube. Filled nanotubes were shown to deform at the vicinity of the filled part or imperfection sites.¹⁵ The maximum in-plane bending angle in our case was measured as $\sim 65^\circ \pm 3^\circ$ (Figure 4.3 at 10 seconds), which is in a good comparison with the 70° angle reported by Golberg *et al.* for multi walled BNNTs.¹⁴ For single walled BNNTs, Enyashin and Ivanovskii's theoretical simulations predicted this angle to be $30\text{-}40^\circ$.⁶⁹ We found that our nanotube can totally recover its initial tubular structure after unloading from the bending (Figure 4.3, Released). There was no noticeable defects formation or failure in the structure of this sample even after applying 50 cycles of bending, to the same bending angle, and unloading.

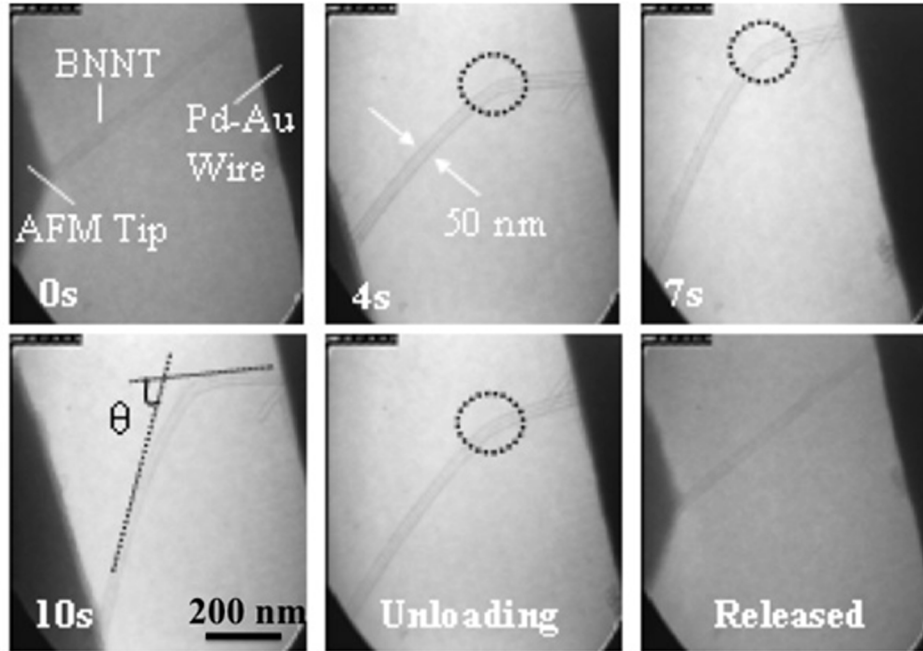


Figure 4.3 In situ TEM observation shows small-angle ($\sim 65^\circ$) bending of an individual BNNT at 300nm displacement within 10s. Bending point (circled) appears near the middle of the nanotube and is fully recovered upon releasing the applied force. The images captured from the recorded video.

Figure 4.4 displays the force-displacement (F - D) plots obtained after 1 and 10 bending cycles corresponds to the 65° of bending deformation. As shown, there was no sudden drop in the applied forces, indicates that the bending cycles introduce no structural failure in the nanotube. There are some deviation between these curves owing to the nanoscopic changes of contact condition between the AFM tip and the nanotube during the loading and unloading cycling processes.

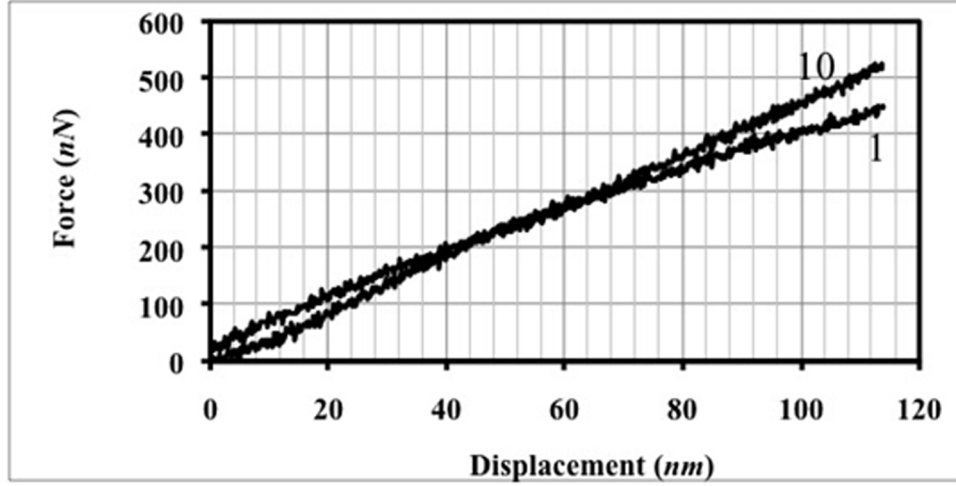


Figure 4.4 F - D curves during the cyclic bending deformation of an individual BNNT at deformation cycles of 1 and 10.

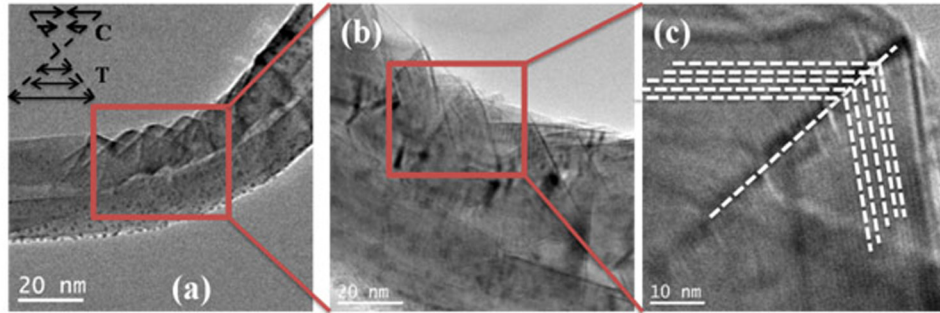


Figure 4.5 TEM images of a BNNT at the bended area reveal the mechanism by which the nanotubes accommodate high bending angles close to 65° . The compression, C, and tension, T, sides of the nanotube are schematically shown in the inset of (a). The dashed lines shown in (c) represent a tilt in atomic planes along a particular set of atoms.

Considering the ionic nature of bonding in BNNTs, one expects to observe a brittle type behavior. Such high flexibility motivated the authors to conduct a close examination of the bent nanotube in high resolution TEM. Figure 4.5 corresponds to serious of images that reveal the mechanism by which the BNNTs accommodate high bending angles close to 65° . The dashed lines shown in Figure 4.5c represent a tilt in atomic planes along a particular set of atoms. The compression, C, and tension, T, sides

of the nanotube are schematically shown in the inset of Figure 4.5a. In several locations along the compressive side of the nanotube these tilted planes were observed in Figure 4.5b. This mechanism was highly reversible and after unloading no sign of tilted plane could be detected.

Using the maximum applied forces in the F - D curves, the Young's modulus of nanotubes can be estimated based on the Euler's formula for nanotubes assuming that both ends are fixed,⁷³ where the maximum applied force is $F_{\text{Euler}} = \pi^2 EI / L^2$. Here, L is the length of the BNNT between the two contacts ($=1.5 \mu\text{m}$), E is the elastic modulus, and the moment of inertial,

$$I = \frac{\pi (d_2^4 - d_1^4)}{64} \quad (4-1)$$

where d_1 and d_2 are the internal and external BNNT diameters, respectively. Table 4.1 shows the calculations for five different nanotubes. The average Young's modulus detected here was $\sim 0.5 \text{ TPa} \pm 0.1 \text{ TPa}$. The data were reproducible after multiple tests with different individual BNNTs.

Table 4.1

The estimated structural parameters for five different BNNTs and the calculated Young's modulus and standard deviation are shown.

	d_1 (nm)	d_2 (nm)	L (nm)	F (nN)	Elastic Modulus (TPa)
Nanotube 1	34	51	1400	600	0.45
Nanotube 2	29	44	1600	390	0.68
Nanotube 3	25	50	1500	600	0.48
Nanotube 4	26	48	1800	420	0.58
Nanotube 5	22	38	1300	350	0.66

For the large-angle bending tests, we increased the deformation angle up to 120° to capture the pertinent structural changes. Interestingly BNNTs failed in a fracture mode. Figure 4.6 shows the representable real-time process of the failure of an individual BNNT after numerous cycling bending. The F - D curve corresponding to this fracture event illustrates the changes in the force applied to the nanotube (Figure 4.6a-e). We have recorded three discrete drops in applied forces. The first drop, at the beginning of the experiment, is due to the nanoscopic sliding of the nanotube on the AFM tip. This results in the drop of the applied force. The other two drops (~ 200 nN each) represent the process of failure initiation and propagation in the nanotube shell walls (Figure 4.6c-e). As the TEM images show, the fracture initiates from the outermost shells (Figure 4.6c) that are under tensile stress and propagates (Figure 4.6e) toward the axis of nanotube, almost perpendicular to the applied force axis. As this particular BNNT has a wall thickness ~ 12 nm, this nanotubes was having ~ 36 layers of hexagonal boron nitride (h -BN) shells. Since the fracture processes initiated only two discrete drops of applied forces within this particular cycle of bending, apparently multiple h -BN shells are broken simultaneously in two patches resembling a brittle type fracture. It is noted that a few layers of shells were still remained after this bending cycle as shown in Figure 4.6e. By repeating the bending cycles (Figure 4.6f-h), the nanotube was eventually broken into two parts (Figure 4.6i).

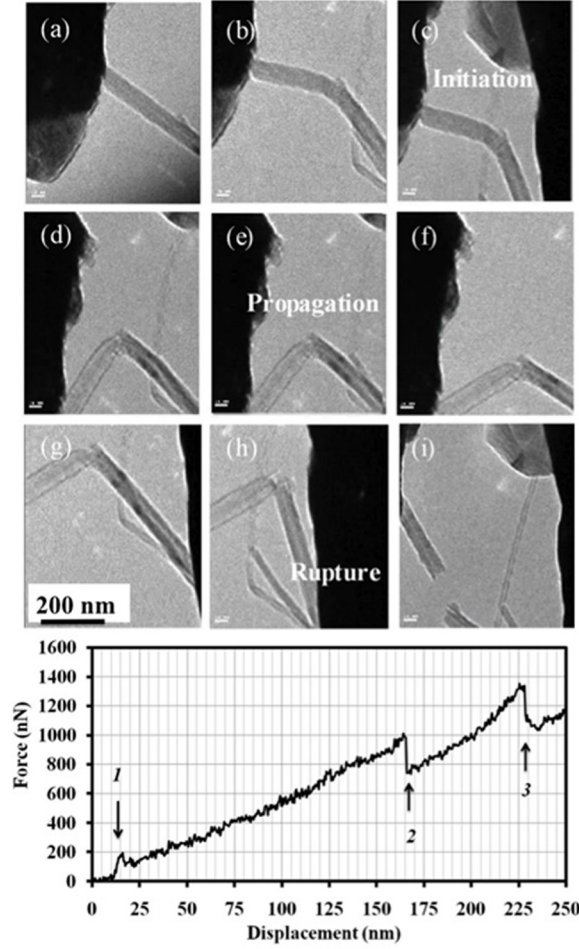


Figure 4.6 Process of fracture in an individual BNNT after the large-angle ($\sim 120^\circ$) bending cycles. (a) to (e) represent one cycle of bending. (f) to (i) showing nanotube breaking into two parts after pulling and stretching. (j) F - D plot represents the changes in force upon failure initiation and propagation during one cycle (a to e). Scale bars are 20 nm.

We think that the rupturing in the outermost shells may be initiated by structural imperfection such as the Stone-Wales defects.⁶⁵ Yu *et al.* reported the breakage of multi-walled carbon nanotubes (MWCNTs) in the outermost layer.⁷⁴ They assumed that structural defects, such as Stone-Wales, produced during the synthesis process, were responsible for the fracture. Espinosa *et al.*⁷⁵ also reported failure of outer shells of MWCNTs as a function of irradiation dose. Ding *et al.*⁷⁶ also observed similar failure

mechanism. They estimated that defects in the outer shell can cause stress concentrations and thus failure.

We then examined the cross-section of the fractured nanotube by using the broken segment 2 to lift the other segment 1. As shown in Figure 4.7, we used segment 2 to rotate segment 1 so that the cross-section is perpendicular to the electron beam. Figure 4.7a-c demonstrate these manipulation. In Figure 4.7d, the broken cross section (marked in a circle) is shown as a ring shape, indicating the present of the tubular structures. The inner channel at the center of the broken cross section can be clearly observed. The diameters of the two broken parts were almost similar (Figure 4.7d) suggesting that the breakage of the nanotube shells is brittle. This is in agreement with the existing belief about BNNT brittleness due to the partially ionic character of chemical bonding between the B and N atoms.

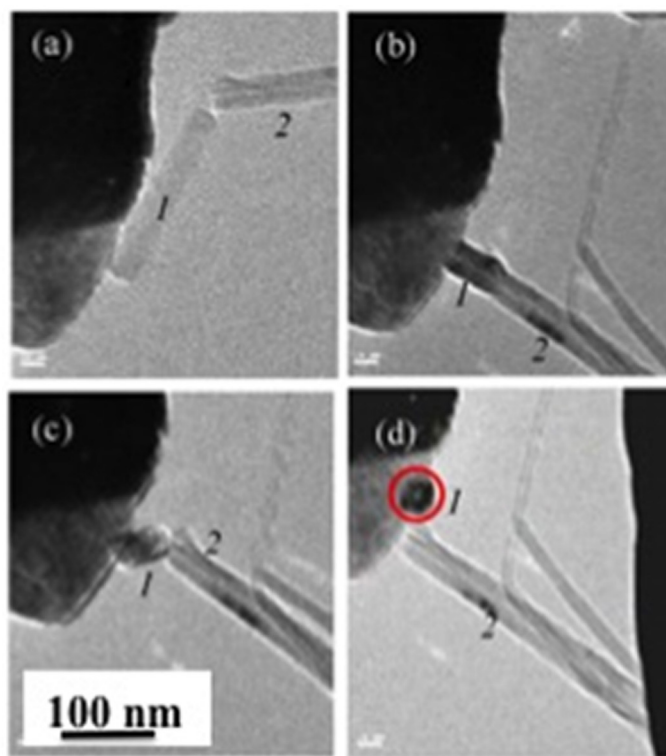


Figure 4.7 (a)-(c) Manipulation of the broken BNNT on the left (1) using the broken segment on the right (2). (d) Cross-section view of the broken nanotube as marked in a circle. The empty area at the center represents the inner channel of the BNNT. Scale bars are 20 nm.

4. 4. Conclusion

In summary, we tested the mechanical properties of individual BNNTs by cyclic bending using an in-situ AFM/TEM system. The structures of BNNTs remained after the low-angle ($\sim 65^\circ$) cyclic bending. For the high-angle ($\sim 120^\circ$) cyclic bending, in-situ TEM imaging allowed the real-time recording of the shell-walls failure initiation and propagation process. Brittle failure mechanism was observed for bending failure of BNNTs. The drops of the measured force corresponding to the failure of shell-walls determined the contribution of shell-walls on the overall strength of nanotubes.

Chapter 5 -IN-SITU OBSERVATION OF REVERSIBLE RIPPLING IN MULTI-WALLED BORON NITRIDE NANOTUBES

The material contained in this chapter was previously published in the *Journal of Nanotechnology* (Reprinted with permission from H. M. Ghassemi, C. H. Lee, Y. K. Yap, and R. S. Yassar, *Journal of Nanotechnology* 22, 115702 (2011). Copyright 2010, IOP Publishing Ltd.) doi:10.1088/0957-4484/22/11/115702

5. 1. Introduction

Mechanical properties of boron nitride nanotubes (BNNTs) are measured and calculated both theoretically^{12,67} and experimentally^{13,41} to be in the same range as those of carbon nanotubes (CNTs), their structural analogue. However, they exhibit important advantages over CNTs, such as higher thermal/chemical stability and thermal conductivity.^{30,77} In addition, their electronic properties are independent with respect to chirality, diameter, or nanotube length.²⁹ BNNTs offer variety of applications in nano-scale electronic devices,^{78,79} optoelectronics,⁸⁰ and as reinforcement in composites.⁸¹ Overall understanding of their mechanical behavior limits the drawing of BNNT-related materials.

There are numerous reports on mechanical responses of single-⁸² and multi-walled CNTs,^{62,83,84} CNTs embedded in matrices,^{85,86} or under torsion force. Iijima *et al.*⁶³ first observed single kinks in single-walled CNTs of diameters 0.8 nm and 1.2 nm bent to large angles. Later on, they also reported that in case of five-walled CNTs, first a single kink was developed; then at higher bending curvature, the same nanotube developed double kinks. Transmission electron microscopy (TEM) images revealed that the distances between respective shells of the nanotube stayed unchanged, even at presence of the kinks at high bending angles. Poncharal *et al.*⁸⁴ and Bower *et al.*⁸⁵ also observed local buckling of multi-walled CNTs during bending. Their TEM images indicate that the buckling wavelength is a function of nanotube radius and the wall thickness.

The authors recently reported⁸⁷ mechanical characterization and fracture detection of individual BNNTs as a result of cyclic bending deformation. We observed the formation of several ripples during bending deformation of multi-walled BNNTs. However, no quantitative correlation between nanotube's structural parameters and the rippling wavelength was given. Here, we examined the buckling formation of several BNNTs inside a TEM equipped with an atomic force microscope (AFM) and correlated the nanotube structural parameters and buckling characteristics.

5.2. Experimental Procedure

The in-situ experiments were conducted by an AFM that was operated inside a JEOL JEM-4000FX TEM at 200 kV. The BNNTs were directly deposited on Si substrates by thermal chemical vapor deposition at 1100–1200 °C in a conventional tube furnace.¹⁷ Powders including MgO, Fe₂O₃, and pure B were used as precursors, and NH₃ gas was used as the source of nitrogen.

Individual BNNTs were then attached on an Au wire by light mechanical scratching on the as grown samples. As a result of van der Waals forces, individual nanotubes stick to the wire in different directions. The Au wire was then fixed on the Au hat, which sits on the sapphire ball. Applying friction force between the hat legs and sapphire ball, the piezo-driven holder allows nanometer motion of the sample toward the AFM tip. Sample position can be adjusted with a precision of 1 nm in X, Y and Z directions.

5.3. *In-Situ* Bending Experiments

Figure 5.1*a* shows a multi-walled BNNT between the AFM probe and the base of gold wire. At this initial stage, there is no sign of rippling throughout the length of the nanotube. Upon applying axial compressive force (F_x) on the nanotube, the nanotube starts to bend. The bending deformation is due to the moment M introduced as a result of the off-axis configuration between the nanotube and the support contacts. This is shown by the free-body diagram expression of nanotube where force, F , is applied by the AFM tip along the horizontal direction (Figure 5.1*b*). Assuming the two-dimensional coordinates along the nanotube axis, the force on the nanotube can be dissociated into F_x

and F_y where $M = F_y \cdot L \cdot \cos\theta$, where L is the distance along the nanotubes axis between the contact points on the Au wire and the AFM tip, and θ is the angle between F and the nanotubes axis. Figure 5.1c shows multiple rippling formed around the bending center of the nanotube. The individual ripples are marked by arrows in Figure 5.1d. The rippling formation was observed only on the compressive side of the nanotube and no sign of rippling was detected on the tensile part (Figure 5.1d).

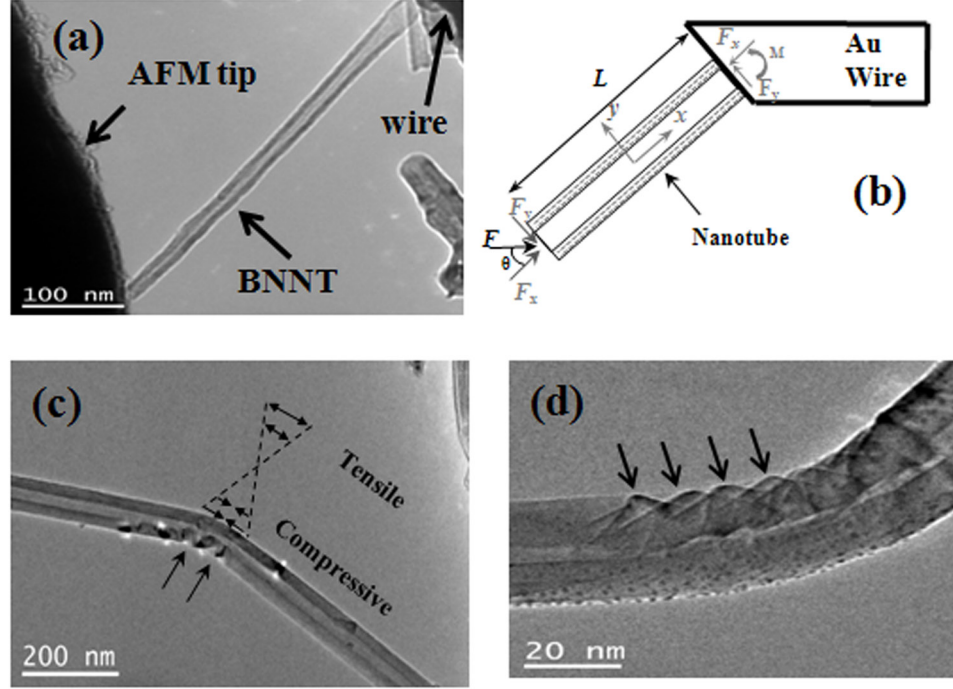


Figure 5.1 (a) Represents bending experiment of an individual multi-walled BNNT in contact with AFM tip (on left) and gold wire base (on right). (b) Free-body diagram of the bending experiment in (a) with analysis of associated forces. (c) The bent nanotube is shown and special pattern formation at the bent area is marked by arrows. (d) High Resolution (HR) TEM image of individual bent BNNT reveals that the special pattern consists of multiple rippling on the compressive side of nanotube.

Figure 5.2 represents force-displacement plots of typical individual nanotubes under one, ten, and twenty cycles of bending deformation. Not much difference in terms of applied force at various cycles could be detected which suggests that the rippling

formation is reversible. The HRTEM imaging of the nanotubes after unloading revealed no apparent fracture. Regularly distributed ripples were observed on the compressive side of the bent nanotube. Upon changing the direction of bending, the location of buckles shifted. This, in fact, suggests that the buckles formation is reversible and is not affected by defects.

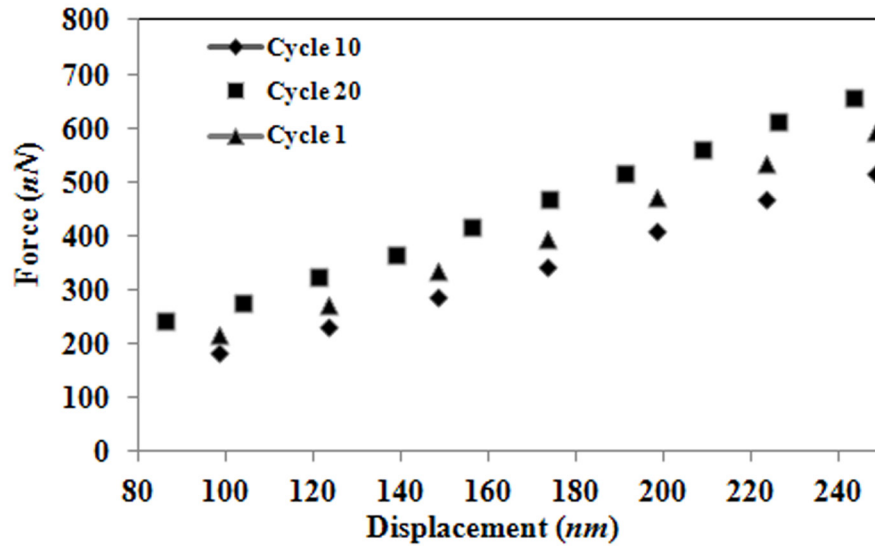


Figure 5.2 Force-displacement plots of a BNNT under cyclic bending deformation.

5.3.1 Buckling Characteristics

During bending and buckling deformation, a distinct morphological characteristic for rippling was observed. The buckling was associated with sharp corners as shown in Figure 5.3a. The appearance of V-shape buckles has not been reported in CNTs.^{82,62,86} The V-shaped ripple, shown in Figure 5.3a, has a folding angle of 120°. These sharp-cornered features are possible with the formation heptagon-pentagon pairs and unfavorable B-B or N-N bonds. The applied axial force, causing the bending deformation, can provide the energy required for this energetically unfavorable deformation. Hence, one can conclude that nanotube transmits the applied deformation force through the above mentioned mechanism to avoid mechanical failure and maintain the nanotubular structure. This interpretation is consistent with the reported flat tip

structure in BNNTs. Loiseau *et al.*⁵⁴ described that such a flat tip structure is correspond to three interconnected hexagonal BN network with 120° disclination in between. The results suggest that these thermodynamically unstable B-B/N-N bonds can switch back to stable B-N bonds as the force is unloaded, due to the more energetically favorite hexagonal BN structures. This conclusion is supported by the fact that multiple force-displacement data that were collected at various stages of rippling formation did not reveal obvious changes (Figure 5.2). Note, another possible scenario of the bond switching at the tip of the buckles can be explained in terms of formation of octagon-square pairs. Based on calculations^{88,89} on the flat end BNNTs, 5-7 member rings can be replaced by 4-8 members to lower the energy of the configuration.

The interlayer distances between the shells of the rippled area were not deviated from the original value of 0.35 nm, as shown in Figure 5.3a. This was validated by plotting the line intensity diagram of the nanotube (Figure 5.3b) in the buckled area of Figure 5.3a. The existence of van der Waals forces between the B-N atomic layers can play a major role in controlling the inner shell distances. The importance of these forces was also reported by Cumings *et al.*⁹⁰ during the telescoping phenomenon in multi-walled carbon nanotubes. The van der Waals forces between the B-N layers keep the inner shells distance fixed, resulting the rigid bending of B-N layers on top of each other. Van der Waals interactions also prevent the reduction of the inner diameter of the nanotube to below 0.35 nm, where these interaction forces become strongly repulsive. In other words, the van der Waals force can override the tube elasticity at *c*-axis.

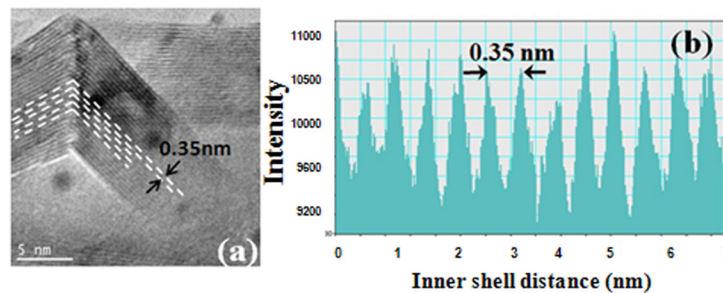


Figure 5.3 (a) HRTEM image of an individual BNNT shows typical V-shape buckles on compression side. (b) The line intensity across along the red line in (a) indicates that the average distance between walls is ~ 0.35 nm.

5.3.1 Quantitative Correlation of Buckling and Nanotube Characteristics

Assuming zero strain along the axis of nanotube, off-axis/buckling strain (ε) can be calculated as r/R , where r is the radius of the nanotube and R is the radius of curvature measured at the hollow center of the nanotube. Measurements based on HRTEM images reveal that first buckle starts to form at ε range from 4.1-9%, depending on the wall thickness of nanotubes. This is in agreement with the results by Bower *et al.*⁸⁵ where it is shown that the onset buckling strain of multi-walled CNTs inside a polymer matrix can reach up to 5%. The wall thickness represents the number of shells, which reflects the magnitude of B-N bonds and also van der Waals force against the bending deformation. Upon further bending, the second buckle starts to form, mainly at $\varepsilon > 11.6\%$. Finally, at $\varepsilon \approx 26\%$, periodic rippling is formed next to each other, on the compression side of the nanotube. This level of strain is equivalent to 240 nm of displacement shown in Figure 5.2. Upon unloading, the nanotube springs back to its original straight shape.

The circular cross section of nanotube tends to be ovalized which is known as Brazier effect.⁹¹ The other mode of deformation in bending experiment is bifurcation, which is well known in continuum mechanics.⁹² It is periodic rippling of the tube wall (Figure 5.1d) that appears on the compressive stressed side of the nanotube. The wavelength of the rippling is predicted by Timoshenko's thin shell theory under axial compression as:⁹³

$$\lambda = \frac{2\pi}{\sqrt[4]{12(1-\nu^2)}} \sqrt{r \cdot h} \quad (5-1)$$

where, ν is the Poisson ratio, r is the outer diameter and h is the wall thickness of thin shell. Substituting the Poisson ratio of 0.2-0.4⁹⁴ for h -BNs, the value of $\lambda/\sqrt{r \cdot h}$ is found to be 3.4-3.5. In the case of nanotubes, the r , h , and λ parameters are shown in Figure 5.4a and the variation of buckling wavelength for several BNNTs are plotted in terms of

$(r.h)^{0.5}$. The ratio of $\lambda/\sqrt{r.h}$ for multi-walled BNNTs is equal to ~ 1.45 , much smaller than the predicted value by classical mechanics (~ 3.4). The difference can be explained by the fact that the classical continuum mechanics models are defined for thin-shell tubes where $r/h > 10$, while in multi-walled BNNT $1.3 < r/h < 1.8$. Moreover, in case of nanotubes, the contribution of van der Waals interaction in transmitting the applied force through the shells should be taken into account. While, in classical continuum mechanics models the interaction between shells is ignored.

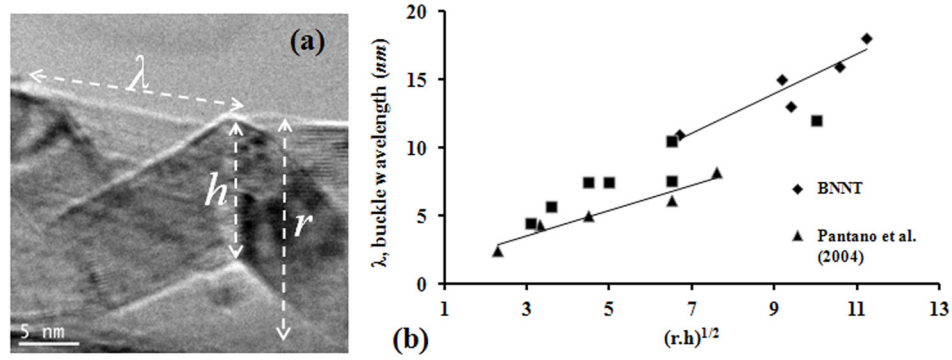


Figure 5.4 (a) Bright field TEM image of a buckled BNNT and the representative structural parameters r , h , and λ are shown. (b) The plot of buckling wavelength λ as a function of $(r.h)^{0.5}$ where several BNNTs (solid line) are compared with the available data on CNTs in the literature (dashed line).

In Figure 5.4b, the data for buckling formation in BNNTs are compared with the similar phenomenon in CNTs reported by Bower *et al.*⁸⁵ and Pantano *et al.*⁹⁵ In both cases of CNTs and BNNTs, as the thickness of nanotubes increase the wavelength of the buckles increase. However, in CNTs the ratio of $\lambda/(r.h)^{0.5}$ is reported to be close to ~ 1 ,⁸⁵ whereas we obtained the value of ~ 1.45 for BNNTs. The reason for higher rippling wavelength in BNNTs in comparison to that of CNTs can be explained in terms of minimization in the number of unfavorable B-B or N-N bonds. Figure 5.5a illustrates hexagon BN structure in each shell before bending deformation. The arrow indicates the bond switching that result in a heptagon-pentagon pair formation at the corner of the ripples as shown in Figure 5.5b. Hence, the system energy increases at those corners due to thermodynamically-unfavorable B-B or N-N bonds, and thus the BN structure tends to minimize the number of B-B or N-N bonds. In contrast, in CNT structures, the C-C

bonds have no thermodynamic restriction. Two hypothetical scenarios that can happen in the buckled BNNTs are described schematically in Figure 5.5c. In one scenario, two ripples with the wavelength of λ_1 are shown at total length of $2\lambda_1$. Statistically this structure has three unfavorable B-B or N-N at the three sharp corners. In Scenario 2 and for the same total length, the ripple with wavelength λ_2 has only two unfavorable B-B or N-N bonds. The latter scenario is more stable than the former and can explain the larger wavelength in BNNTs in comparison to CNTs.

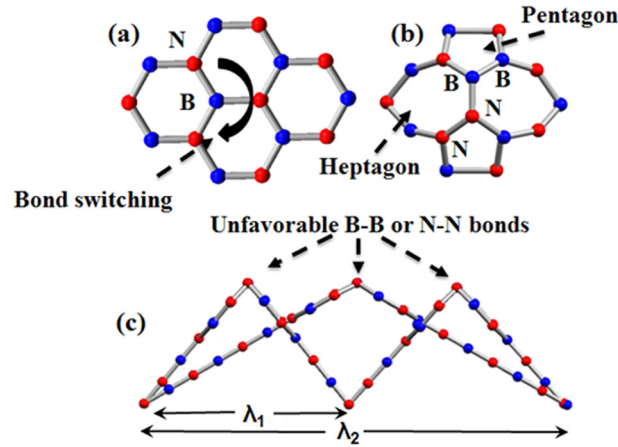


Figure 5.5 (a) Schematic of BN hexagon atomic arrangement in each shell before bending deformation. Arrow shows the direction of bond switching. (b) Top view of BN pentagon-heptagon pairs as a result of bending deformation. (c) A 2D schematic of ripples under two hypothetical scenarios. The ripples with wavelengths of λ_1 and $\lambda_2=2\lambda_1$ are shown for at total length of λ_2 . Thermodynamically unfavorable B-B and N-N bonds are higher in the small ripples in comparison to the large ripple.

5. 4. Conclusion

Multi-walled BNNTs were subjected to buckling experiments inside a TEM. We observe that BNNTs are highly flexible which is countertuitive knowing that they possess ionic structure. Multiple rippling was observed on the compressive side of buckled nanotubes. The first ripple started at strain of 4.1%, and more ripples were formed by increased the applied strain. Our results reveal that the rippling wavelength and nanotube outer diameter, r , and thickness, h , are correlated through the relationship of, $\lambda/(r.h)^{0.5} \approx 1.45$. It was also found that buckling was reversible up to 26% strain. The

buckling wavelengths in BNNTs are larger in comparison to the data reported in the literature for CNTs. This difference was explained by the tendency of BN structures to reduce the number of unfavorable B-B and N-N bonds at the sharp corners in the rippling regions.

Chapter 6 -FIELD EMISSION AND STRAIN-ENGINEERING OF ELECTRONIC PROPERTIES IN BORON NITRIDE NANOTUBES

The material contained in this chapter is submitted to the Journal of *Advanced Functional Materials*, but no copyright transfer agreement has been signed yet, as it is in the initial phase of review.

6.1 Introduction

Boron nitride nanotubes (BNNTs) are not only structurally similar to carbon nanotubes (CNTs),⁵³ but their mechanical properties are also calculated and measured to be comparable to that of the CNTs.⁷¹ However, BNNTs show insulating behavior due to wide band gap of 5.4 eV.²⁹ Theoretical simulations predict that the electronic properties in BNNTs can be tuned by means of mechanical deformation or chemical alteration. Kim *et al.*⁴² concluded that the band gap of BNNTs was reduced as the cross-section of the nanotubes became oval under bending deformation. Their density functional calculations showed that redistribution of charges is more significant in the conduction band, compared to that of the valence band. Golberg *et al.*⁹⁶ altered the BN structure by adding carbon and facilitating the formation of B-C-N layers. Their electrical and field emission (FE) results showed significant improvement in the measured conductivity.

The superior structural stability of BNNTs in comparison to CNTs justifies their candidacy for FE applications.⁴⁴ Thermogravimetry analysis shows that BNNTs are stable up to 950°C, while CNTs decompose at 500°C.²² *In-situ* transmission electron microscopy (TEM) observations also showed electrical failure of CNTs take place at a voltage range of ± 7 V whereas BNNTs could withstand up to ± 140 V with no electrical breakdown or physical failure.⁹⁷ *In-situ* FE experiments conducted by Cumings *et al.*⁴⁵ on individual BNNTs showed stable current at high bias voltages. However, they did not study the stability of emission current under multi-cycle measurements. Since long-term emission stability is one of the major factors that prevents practical the applications of

nanotubes,⁴⁶ thus it is important to further understand the FE cycling performance of BNNTs for potential applications in flat panel displays.

In this work, we first tuned the electrical properties of BNNTs under mechanical deformation. The mechanical deformation was performed on individual BNNTs inside the chamber of a TEM using an *in-situ* scanning tunneling microscopy (STM) holder. Electrical and semiconducting properties of BNNTs were measured under different strain level. Then, we evaluated the FE stability of individual BNNTs. TEM images were captured after each cycles of FE experiments to study the possible relation between the emission stability and the structural integrity of BNNTs.

6.2 Materials and Methods

Our BNNTs were directly deposited on Si substrates by thermal chemical vapor deposition at 1100-1200 °C in a conventional tube furnace.¹⁷ These BNNTs have a band gap of 6 eV,¹⁷ which is higher than those reported in previous works (~5.4 eV).^{98,99} The conductivity probing experiments were performed by STM holder under *in-situ* monitoring in JEOL JEM-4000FX, operated at 200 kV. Individual BNNTs were then attached on an Au wire by either light mechanical scratching on the as-grown samples or using silver paste. This Au wire was then fixed on the tip of a piezo-driven holder that allowed nanometer motion of the sample toward the STM tip. The sample position was adjustable with a precision of 1nm in X, Y and Z directions. Here, the sample was grounded and positive bias voltages were applied to the STM tip. Then the *I-V* curves were measured using the Nanofactory™ instrument (up to ±80 V) power generator. To reduce the effect of electron beam irradiation on the nanotubes during *I-V* measurements, the electron beam current of the TEM was reduced to half of those we use for normal imaging. For the FE experiments, BNNTs were retraced away from the STM tip and then were biased with negative range voltage to emit electrons. The applied range of voltage started from zero up to 110 V within 20-60 seconds. To enhance the accuracy of current measurements, a flat part of STM tip was used to collect the emission current. Because of insulating behavior of BNNTs and voltage limitation of our setup, a short distance between the tip of BNNTs and the STM tip were used to form sufficient electric field for capturing emission current from BNNTs.

6.3 Materials and Methods

6.3.1 Strain Engineering of Electrical Conductivity in BNNTs

Figure 6.1a represents I - V behaviors of individual BNNTs under continued increase of mechanical straining. The black curve near the X -axis shows a current flow of a few nA at 80V applied voltage indicating the insulating behavior of pure BNNTs with no bending deformation (corresponding to Figure 6.1b). Our calculations revealed that the resistance of pure non-deformed BNNT is around 10 G Ω which is in good agreement with the reported values.⁴³

Next, the nanotube was subjected to a series of mechanical straining while I - V data were simultaneously collected. Figure 6.1c and 1d represent two different bending curvatures of the BNNT (shown in Figure 6.1a) under different applied forces. The colorful curves in Figure 6.1a, labeled as 1-8, represent the I - V curves at different bending curvatures. The applied stress changes the conductivity of BNNT; hence, higher current flows were detected at higher strain levels (corresponding 1-8 in Figure 6.1a).

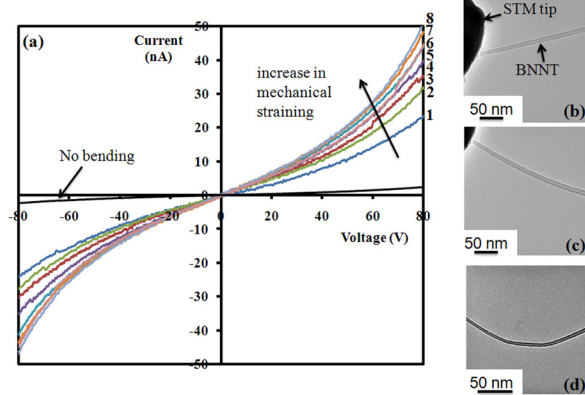


Figure 6.1 (a) The corresponding I - V curves of a BNNT under mechanical straining. The colored curves indicate the I - V data during progressive strain loading and the black curve (marked with a short arrow) shows the insulating behavior under no bending. (b) The TEM image of a BNNT in contact with STM tip (no loading) corresponds to the black curve in (a). (c) and (d) The TEM images of BNNTs under the continues increase of mechanical straining, respectively. The bending curvatures of the BNNT increase due to higher mechanical straining. I - V curves 1 and 8 represent cases with the lowest to highest amount of bending.

One can notice from Figure 6.1a that I - V curves are not symmetric, for instance, the red curve, labeled as 3, at 80 V leads to a current of 35 nA whereas the current detected at -80 V was -30 nA. These asymmetric I - V behaviors are due to different contact barriers at both ends of the BNNT. As mentioned in the experimental procedure, one end of the nanotube is in contact with the tungsten STM tip, and the other end is in contact with the gold wire. This can form a metal-semiconductor-metal (M - S - M) circuit with different work functions and therefore, different Schottky barriers.¹⁰⁰

Following the theory of a M - S - M circuit,¹⁰¹ one can calculate the semiconducting parameters of BNNT by

$$\ln I = \ln S + V \left(\left(\frac{q}{k_B T} \right) - \frac{1}{E_0} \right) + \ln J_s \quad (6-1)$$

where S is the contact area associated with a bias, J_s is slowly varying function of the applied bias. The $\ln I$ versus V plot gives an approximately straight line with a slope of $\frac{q}{k_B T} - \frac{1}{E_0}$, and an intercept of $\ln S$, as shown in Figure 6.2a. In this case, $E_0 = E_{00} \coth[E_{00} / (k_B T)]$, where $E_{00} = (\hbar q / 2)(n / (m^* \epsilon))^{1/2}$. Here, \hbar is $1/2\pi$ of the Planck constant, q is the elemental charge, k_B is the Boltzmann constant, m^* is an effective electron mass of BNNT, n is carrier concentration; and ϵ is the dielectric constant. The electron mobility, μ , is then calculated by using the relationship $\mu = I / (nq\rho)$, where ρ is the resistivity of the strained BNNT estimated from the I - V curves. The calculated parameters of a BNNT under different bending deformation are plotted as shown in Figure 6.2b-d.

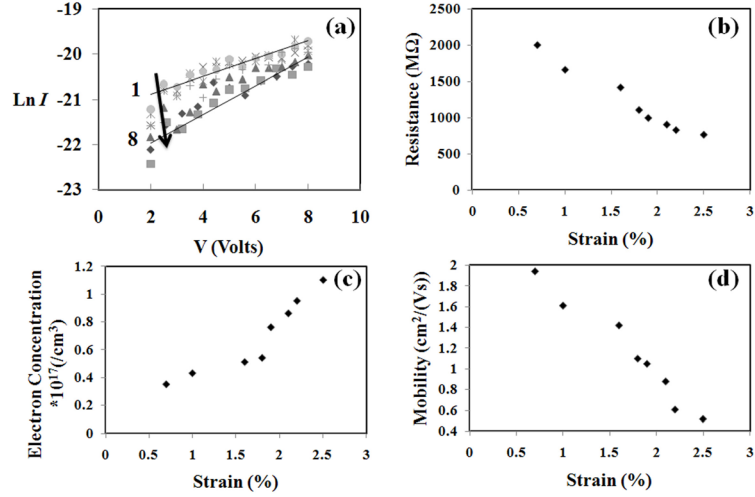


Figure 6.2 (a) Characteristic $\ln I$ - V data corresponding to the I - V curves shown in Figure 6.1a. Arrow from 1 toward 8 indicates the increase in the bending deformation. (b-d) represent the parameters of resistance, electron concentration and mobility of the bent BNNT as a function of mechanical straining.

As plotted in Figure 6.2b, the resistance of BNNT (dV/dI) can be tuned in a wide range of 2000-769 $M\Omega$ under minimum and maximum bending deformations labeled as curves 1 and 8 in Figure 6.1a, respectively. Our calculation indicates that the electron concentration increases by a factor of 3 (Figure 6.2c), however, the carriers mobility is decreased (Figure 6.2d). The reduction in carrier mobility can be related to the scattering between electron-phonon under the applied electric field,¹⁰² or due to presence of impurities similar to the reported results for graphene.¹⁰³ As the nanotube bends, the radius of the curvature in the nanotube's cross-section also changes. The theoretical calculations show that the conduction electrons are more sensitive to the induced-curvature while the valance electrons remain relatively unaffected.⁴² As a result, the charge distribution density across the nanotube diameter changes which decreases the energy difference between the band gaps. Similarly, it is reported that in case of ZnO ,¹⁰⁴ Bi_2S_3 ¹⁰⁵ and BNNT,¹⁴ the carrier concentration increases due to band gap reduction upon the applied stress.

Unfortunately, it will be impossible to compare the exact values of electronic parameters obtained in this work with the ones reported in Ref.⁴³ for deformed BNNTs. This is because in Ref.⁴³, the change in I - V characteristics in terms of exact strain values

was not quantified. For instance, the value of strain corresponding to the reported carrier concentration of $1.1 \times 10^{17} / \text{cm}^3$ for deformed BNNTs in Ref. ⁴³ was not given. This point in fact is the strength of the work presented here because for the first time it provides a quantified correlation between the values of strain and the electronic properties of BNNTs.

6.3.2 Field Emission Properties

Figure 6.3a represents the typical field emission characteristic of an individual BNNT (shown in the inset) under an applied bias voltage. The emission of electron starts at a particular voltage (~ 65 V), also known as turn-on voltage, where the measured current exceeds the background current of 0.5 nA, and exponentially increases to 140 nA at 110 V. The turn-on voltage is calculated to be ~ 325 V/ μm and the current density of an individual BNNT is measured as ~ 1 mA/ cm^2 at voltage of 110 V. Note, the emission of electrons from the tip of the nanotubes is a “ballistic” process.¹⁰⁶ In another word, when the sample is biased, electrons emit in group from the tip of the nanotubes. Thus, changes in electrostatic forces between the tip and the STM result in the vibrations of the tip of the nanotubes. Therefore, the fluctuations in the emission current shown in Figure 6.3 and afterward results are due to the fact that the distance between the tip of the nanotubes and the STM surface slightly changes during the FE experiments.

The FE behavior of this nanotube can be modeled following the well-known Fowler–Nordheim (F-N) equation,¹⁰⁷ as shown in Figure 6.3b.

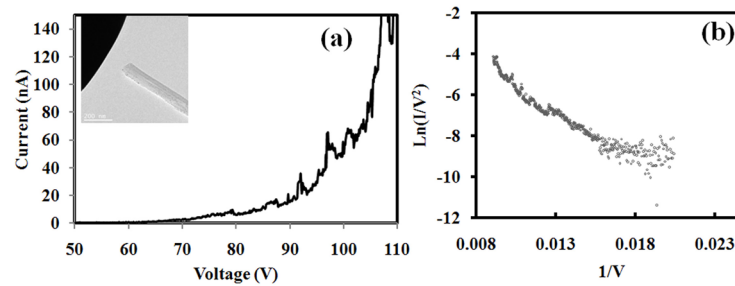


Figure 6.3 (a) the I-V curve represents the FE behavior of an individual BNNT shown in inset (1st FE cycle). Scale bar is 200 nm. (b) The corresponding Fowler-Nordheim plot representing the field emission behavior shown in (a).

The linear plot of $\ln(I/V^2)$ vs. I/V confirms the F-N field emission characteristics of the BNNT. One can notice that BNNT exhibits only one slope which is in good comparison with other reported field emission behavior of BNNTs.⁴⁵ In contrast, CNTs' F-N plot shows two distinct slopes representing current saturation during field emission experiment at high field.^{108,109} Based on the field emission current, one can also calculate other characteristics of the nanotube, such as field enhancement factor, work function, and the radius of the apex, as followed:¹⁰⁷

$$I = KF^2 / \phi \exp(-B\phi^{3/2} / F) \quad (6-2)$$

where $B = 6.8 \times 10^9 \text{ VeV}^{-3/2} \text{ m}^{-1}$, K is a constant, and ϕ is the sample work function. The local electric field, F , is related to the applied voltage V and can be defined as $F = \beta V/d$, where β , the field enhancement factor, quantifies the ability of amplifying the average field V/d . If S is the slope of F-N plot (Figure 6.3b) one can calculate the field enhancement factor using the equation below:

$$S = -B\phi^{3/2}d / \beta \quad (6-3)$$

Assuming the work function of pristine BNNT is 6 eV,⁴² then according to Equation 6-3, $\beta = 98$. The calculated field enhancement factor is significantly higher than the value assumed by Cumings *et al.*⁴⁵ They considered $\beta = 10$ and then back calculated the work function to be ~11-13 eV. This is extremely high for BNNTs as the work functions of 5.5-6 eV has been reported in the literature.¹⁷ Chen *et al.*¹¹⁰ investigated the enhancement in conductivity and the FE behavior of BNNTs coated with Au nanoparticles. In their FE measurement, they assumed that due to high quantity and high uniformity of their morphology slope of Fowler-Nordheim is only proportional to the work function. Therefore, assuming work function of 6 eV, they back calculated the field enhancement factor. Using fixed enhancement factor for all different samples, they calculated changes in the work function of BNNT as a result of Au coating layer.

We then repeated the FE experiment to investigate the structural and emission stability of the BNNT upon four cycles of emission, as illustrated in Figure 6.4a. Curves

1, 2, 3, and 4 represent the 1st, 2nd, 3rd, and 4th FE cycles, respectively. As can be seen, in the 2nd cycle, the turn-on voltage is increased to ~80 V and the emission current dropped slightly to ~120 nA. FE cycles 3 and 4 represent further degradation of emission current as well as higher turn-on voltages, respectively. In the 4th cycle the amount of emission current drops almost 90% in comparison to the 1st cycle.

Previous study showed that the field enhancement factor strongly depended on the geometry of the apex of the emitter.¹¹¹ However, our comparison of the tip radius between the pristine and the FE cycled nanotubes did not show any obvious change. Figure 6.4b also shows that the geometry of the BNNT at the tip, compared to the inset in Figure 6.4a, is not changed significantly. The TEM analysis of the FE cycled nanotube revealed the likelihood of structural decomposition that can explain the reduction in the field enhancement factor. As shown in Figure 6.4b&c, the HRTEM images indicate the presence of dark particles on the outer surface of the FE cycled nanotube. The formation of these particles is due to defects generated by Joule heating to be discussed hereafter. These defects will cause electron scattering and degrade the emission current.

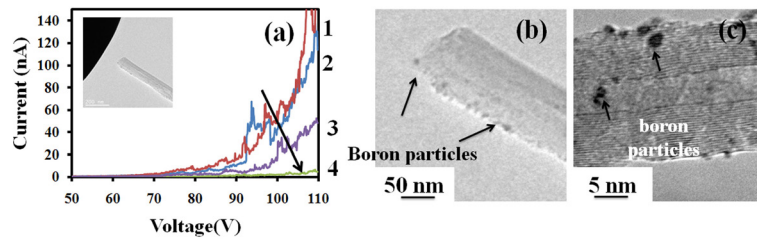


Figure 6.4 (a) Field emission behaviors of the BNNT at four consecutive measurements. (b&c) Arrows indicate the formation of black particles as a result of decomposition on the outer surface of BNNT.

Figure 6.5 represents a schematic of the proposed mechanism of the formation of dark particles on the outer surface of the BNNT. As shown in Figure 6.5a, the sample is biased with negative voltage. As the FE experiments were conducted, due to the high emission current density, the temperature of the sample is increased and reached to the decomposition temperature at which the B-N bonds start to break.⁷² The volatile nitrogen atoms leave the structure and are released into the vacuum while the B atoms remain

(Figure 6.5b). As the number of boron atoms with the dangling bond increases, they tend to form particles, as shown in Figure 6.5 c&d. Therefore, as the nanotube decomposed, nitrogen which contributes 5 electrons compared to boron with 3 electrons leave the structure and emission current of the nanotube degraded significantly. We should note that several other FE experiments were carried out at same voltage range of 140 V but at different distances from the STM tip. As the distance between the tip of the nanotube and STM tip were increased the amount of current also dropped. However, the degradation trend of emission current in FE cycles was also observed indicating that the observed behavior is independent of the distance between the nanotube and the STM tip.

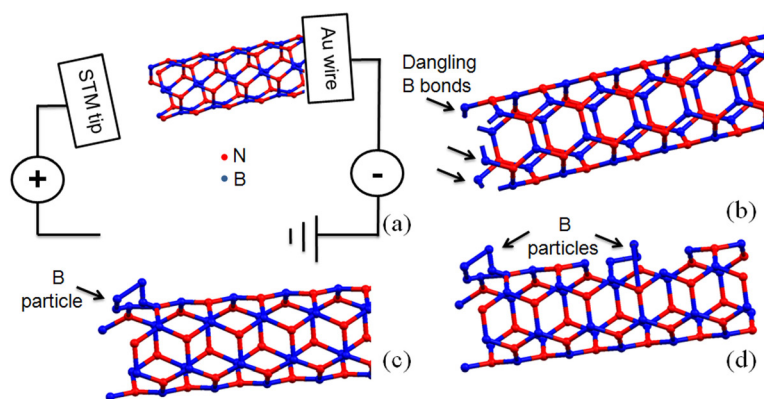


Figure 6.5 (a) The schematic represents the FE setup where there is a gap between the tip of the sample and STM tip. As shown, the sample is biased with negative voltage with respect to the STM tip. (b) Arrows indicate the formation of dangling B bonds. The nitrogen atoms leave the structure when the sample reaches to the decomposition temperature. (c) and (d) illustrate the formation of boron particles as the number of B atoms with dangling bonds is increased.

To rule out the effect of beam damage on the sample, we reduced the accelerating voltage from 300 kV to 200 kV, and also expanded the beam during the experiments. Moreover, if the decomposition was due to the e-beam radiation, then such decomposition phenomenon should also be observed during the normal TEM imaging of BNNTs. But, in fact the formation of particles was only observed when the bias voltage was applied and induced the flow of high density current. In addition, the e-beam radiation should not raise the temperature of nanotube significantly. Based on the model

reported by Jencic *et al.*,¹¹² one can calculate that the temperature raise due to the beam exposure at 200 kV and with low electron flux dose is only a few degrees.

These results are important in order to understand the mechanism and the performance of the emitters before commercializing them. As mentioned earlier, it is reported that the structure of BNNTs is stable at high temperatures. However, our results show that the repeated cycling under a high electric field can lead to degradation in emission properties. Therefore, it is crucial to employ these findings in future design and fabrication of BNNT-base nanodevices such as transistors and electromechanical devices.¹¹³ The effect of strain on the electrical characteristics of BNNTs should also be taken into account. For instance, BNNTs can be used as sensors where their conductivity is changed as a result of applied force or strain.

6.1 Conclusion

We studied the electrical and field emission of individual BNNTs using *in-situ* TEM techniques at bias voltage of up to 110 V. Our results showed that individual BNNTs exhibit the current density of $\sim 1 \text{ mA/cm}^2$ at 110 V and turn-on voltage was 325 V/ μm . However, structural degradation was observed only after 4 cycles of emitting and the emission current dropped significantly. Measurements on the semiconducting parameters of individual BNNTs revealed that the band gap can be tuned by mean of mechanical deformation. Based on the amount of strain, resistance of individual BNNT was engineered in range of 2000-769 M Ω and electron concentration was calculated to be $0.35\text{-}1.1 \times 10^{17} \text{ /cm}^3$ in that range of strain with slight decrease in the mobility of the carriers.

Chapter 7 -*IN-SITU* TEM MONITORING OF THERMAL DECOMPOSITION IN INDIVIDUAL BORON NITRIDE NANOTUBES

The material contained in this chapter was previously published in the JOM JOURNAL OF THE MINERALS, METALS AND MATERIALS SOCIETY (Reprinted with permission from H. M. Ghassemi, C. H. Lee, Y. K. Yap, and R. S. Yassar, Journal of THE MINERALS, METALS AND MATERIALS SOCIETY 62, 69 (2010). Copyright 2010, Springer)

7.1 Introduction

Boron nitride nanotubes (BNNTs) are structurally similar to carbon nanotubes (CNTs), where alternating boron and nitrogen form an ionic structure. Their mechanical properties are predicted to be similar to carbon nanotubes.¹² The Young's modulus of BNNTs have been reported in range of 0.5- 0.8 TPa^{28,41} These nanotubes are also insulators due to their wide band gap of 5.4 eV or higher.²⁹ Thermal characterization of BNNTs showed better stability at higher temperatures in comparison to CNTs. Thermogravimetry curves indicated that BNNTs started to decompose at 950 °C, while in the case of CNTs oxidation happened at 500 °C.²² Thus BNNTs are prospective wide band gap semiconductors for high-power, high-temperature devices.

The study of material failure at elevated temperatures is important for high temperature applications of new energy technologies and electronic systems.^{114,115} In the case of nanotubes and nanowires, one can study the thermal stability and failure of such structures using the Joule heating methods.^{116,117,118,119} According to this approach, at the presence of electrical current, the nanowire or nanotube can be heated to high temperatures. This can result in the variation of electrical properties. Moreover, at elevated temperatures, phase transformation may be induced, and decomposition of the structure may be observed.

While there are a number of reports on mechanical properties of BNNTs at room temperatures^{43,71} the failure of BNNTs has rarely been studied at high temperatures.¹¹⁷ In

this paper, we report the real-time thermal decomposition of individual BNNTs by the use of an in-situ scanning tunneling microscope (STM) inside a transmission electron microscope (TEM). Individual samples were kept under high constant bias voltage of 100 V while TEM images were recorded in-situ to capture the decomposition process.

7.2 Experimental Procedure

The synthesis of BNNTs is challenging and requires very high growth temperatures ($>1500\text{ }^{\circ}\text{C}$), a specific fabrication system, or dangerous chemistry.^{120,98} Recently, we have succeeded in growing BNNTs without dangerous chemicals in a conventional tube furnace.¹⁷ These BNNTs can be grown directly on Si substrates by thermal chemical vapor deposition at $1100\text{--}1200\text{ }^{\circ}\text{C}$. UV–visible absorption spectroscopy (HP 8453 Spectrophotometer) was also used to further characterize the as-grown BNNTs. This was performed by a suspension of BNNTs in ethanol. These multi-walled BNNTs were used in Joule heating experiments. These experiments were conducted inside the chamber of a JEOL JEM-4000FX TEM operating at 200 KV using an in-situ STM holder. The schematic of this holder is shown in Figure 7.1a. It consists of a sapphire ball and a piezo tube mounted on Au wire, can approach the STM tip. Figure 7.1b represents the whole electric circuit when STM tip, BNNTs and Au wire are connected.

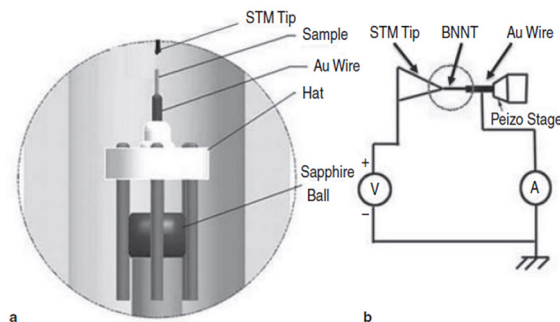


Figure 7.1 (a) Schematic of the utilized STM-TEM sample holder. Sample mounted on Au wire approaches the STM tip via sliding on the sapphire ball. (b) Shows the electric circuit as the BNNT (inside the red circle) is connected to the STM tip and Au wire.

Individual BNNTs were then attached to an Au wire either through mechanical scratching of the wire on the Si substrate or using silver paint. Then the wire was fixed on

a hat which fits on top of a sapphire ball, connected to stacks of piezoelectric layers that allow nanometer motion of the sample toward the STM tip. Using the Nanofactory™ software (NFC3), each sample position was adjusted with a precision of 1 nm in X, Y and Z directions.⁸⁷ Here, the samples were always grounded, and bias voltage was applied to the tungsten STM tip. The STM tip was then inserted into each nanotube to assure a stable contact (Figure 7.2). Constant bias voltage of 100 V was applied to the samples while the current flows were captured as a function of time. To eliminate the possibility for the promotion of thermal decomposing via the electron beam, the experiments were conducted at low intensity electron beam. Also, the accelerating voltage was reduced from 300 Kv to 200 Kv.

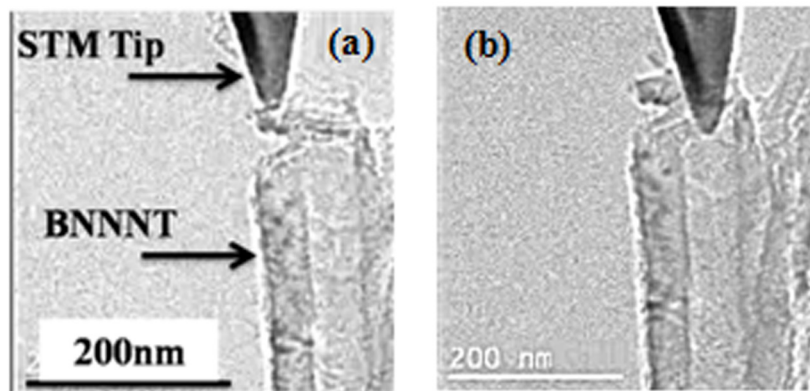


Figure 7.2 (a, b) TEM images correspond to the process of inserting the STM tip into the nanotube to secure the electrical contact.

7.3 Results and Discussion

Individual BNNTs were connected to the STM tip at one end and the Au wire on the other end. Before Joule heating, the outer diameters of the nanotubes were measured to be ~50 nm, while their lengths averaged ~1 μm (Figure 7.3a and b). Average inner shell distance was ~0.35 nm (Figure 7.3c). The structures of the tested nanotubes had no amorphous layer on the outer shells.

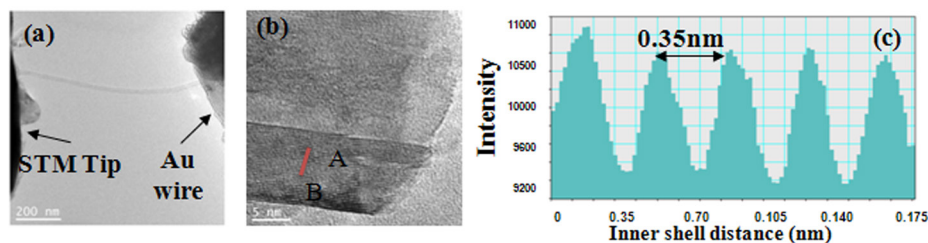


Figure 7.3 (a) TEM image of a BNNT connected across the Au wire and the STM tip. Scale bar is 200nm. (b) High resolution TEM image of the end of an individual BNNT shows that there is no amorphous layer or contamination outside or inside the nanotube. Scale bar is 5nm. (c) The inner-shell distances of a BNNT is determined as 0.35 nm, based on the intensity histogram obtained along the AB line in (b).

Individual nanotubes were then subjected to a bias voltage according to the design shown in Figure 7.1. The electrical current, I , as a function of applied bias voltage, V , was monitored for each nanotube as shown in Figure 7.4a. More than 50 different BNNTs were examined and the recorded I - V data showed consistency. Negligible current could be detected even at high bias voltages. This confirms an insulator behavior in the BNNT nanotubes. This is expected, as our BNNTs possess a wide energy band gap.²⁹ As shown in Figure 7.4b, the strong absorption in UV-visible spectroscopy corresponds to the optical band gap of 5.9 eV, which is higher than the values reported by others by the magnitude of 0.4 eV.^{120,29} The absorption band at ~ 4.75 eV is due to the intrinsic dark exciton absorption. We suggest that the relatively small absorption at ~ 3.7 eV may be associated with defects in the BNNTs.¹⁷

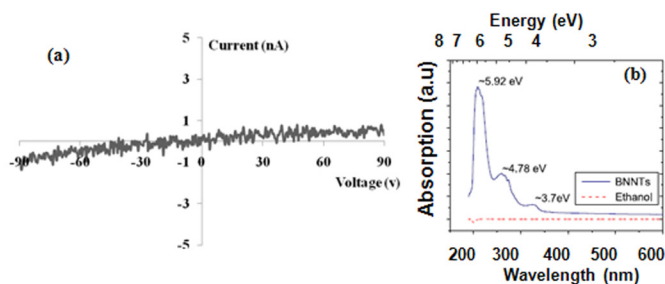


Figure 7.4 (a) The typical I - V curve measured along individual BNNTs does not pass noticeable current under undeformed condition. (b) The strong absorption in UV-visible spectroscopy corresponds to the optical band gap of ~ 5.9 eV.¹⁷ Peak at 4.78 eV corresponds to intrinsic dark exciton absorption and the small peak at 3.7eV is suggested to be associated with the defect in BNNTs.

One should note that the contact resistance cannot be the reason for negligible conductivity in the tested BNNTs. These nanotubes are proven to be insulator by previously published articles due to their large band gap. In addition, we have tested several other nanotubes and nanowires (ZnO, TiO₂, VN, C) and the amount of detected current is in accordance with their expected electrical behavior.

In the Joule heating technique, a number of samples were subjected to high bias voltages that led to current flow through the individual nanotubes. Considering that the input power depends on the square root of current, one expects a high amount of thermal energy to be released due to electron transport in the nanotube. Part of this thermal energy is transferred to the vacuum and the rest increases the temperature of the nanotube. Previous Joule heating experiments estimated the temperature to be more than 1900 °C.¹¹⁷ Figure 7.5 shows the joule heating current versus time after the application of 100 V bias on a nanotube. The detected current increases slightly in the beginning and increases more rapidly after 77 seconds. This is then followed by a sudden drop of current at 95 seconds. The abrupt drop in current, shown in Figure 7.5, corresponds to the structural failure of the nanotube that results in the disconnection of the STM-BNNT-wire electrical circuit. Inset of Figure 7.5 shows the broken part of the nanotube attached to the STM tip after failure.

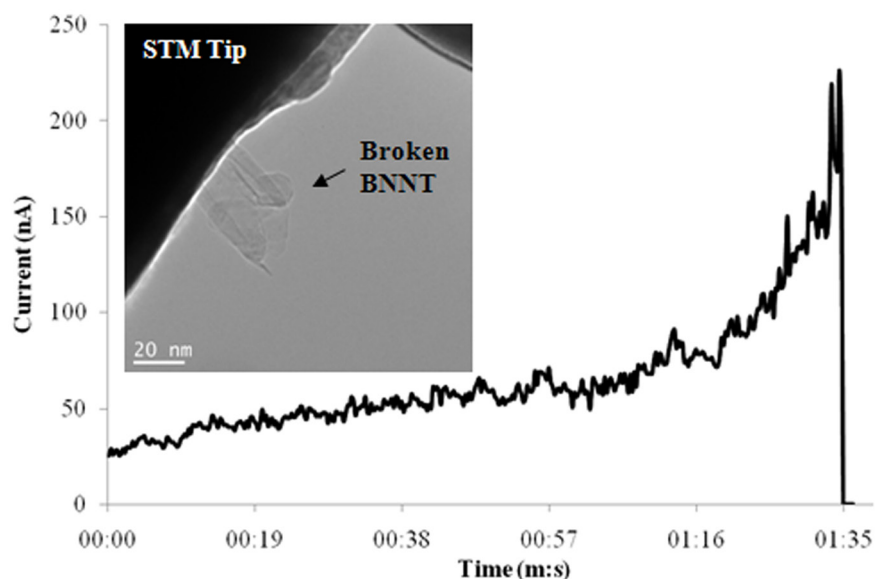


Figure 7.5 Current flow as a function of duration of applied. Constant voltage of 100 V was applied to an individual nanotube. Current increases slightly in the beginning and increases more rapidly after 77 seconds. The sudden drop of current at 95 seconds corresponds to the disconnection of STM-BNNT-wire circuit due to the BNNT decomposition. (Inset) TEM image of showing the broken nanotube is attached to the STM tip.

Figure 7.6 a-f represent the TEM snap shots of thermal decomposition of a BNNT under the application of 100 V bias voltage. One can notice the formation and enlargement of nanoparticles (shown by black arrows) during the decomposition process. The formation of the clusters was faster than the video rate of our camera and thus the capture of initial stage of clustering was quite difficult. No crystallinity could be observed during high resolution TEM analysis, which suggests amorphous structures for these nanoparticles. This finding is in agreement with a recent report.¹¹⁷ Electron energy loss spectroscopy analysis, performed by Zhi *et al.*¹¹⁷ suggests that these particles are clusters of boron atoms. The nitrogen atoms likely leave the structure in the vacuum due to high temperature heating and the application of bias voltage. This bias voltage further strengthens the driving force for the dissociation of bonds in ionic BN structures.

Temperatures up to 1900°K have been reported depending on the geometry of the nanotube.^{116,117}

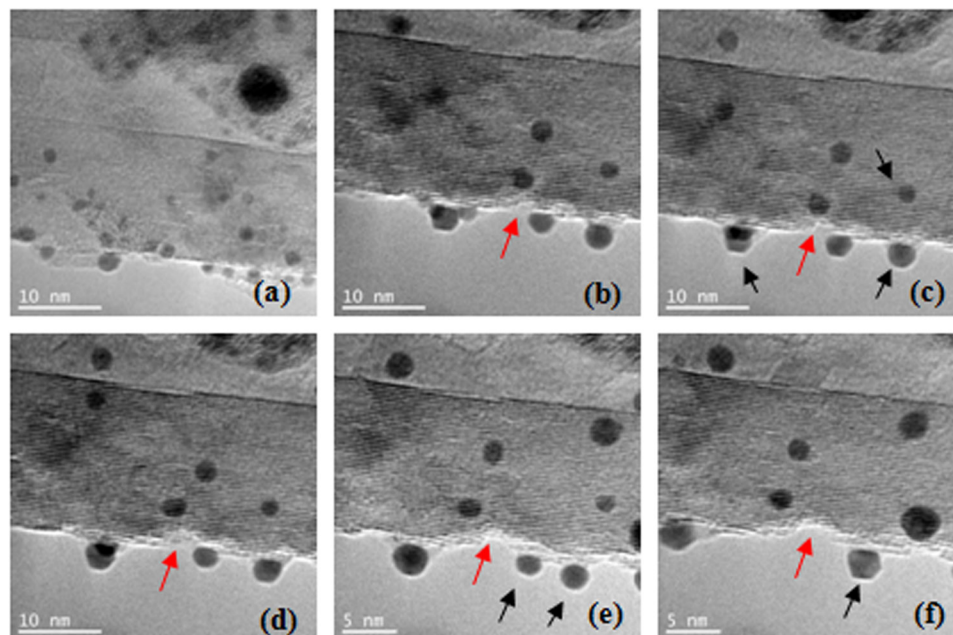


Figure 7.6 (a-f) High-resolution TEM images correspond to the process of nanoparticles formation during the thermal decomposition of BN nanotubes. Black arrows points toward the growth of nanoparticles on the outermost shell layers. Red arrows indicate the void formation in the outer shell of the BN nanotube and its propagation toward the inner shells.

From Figure 7.6, one can see that the decomposition process initiates at the outermost shell layers. This is evident by monitoring the formation of voids on the external shells shown by red arrows in Figure 7.6b-f. While the inner shells remain almost intact, the depth of voids in outer shells gradually increases. Our finding is opposite to the recent report of Zhi's *et al.*¹¹⁷ that reported the start of decomposition process from inner shells. As the red arrows indicate, the voids become deeper while the size of adjacent nanoparticles increases (follow the black arrows in (c) through (f)). These changes suggest that the outer shells of our BNNTs most likely have relatively higher defect density in comparison to inner shells. In addition, structural defects can act as initial sites of decomposition events. Point defects such as vacancy defects turn the favorite B-N bonds to B-B or N-N. As such, the honeycomb morphology converts to 7-5-

5-7 defect (Stone-Wales).⁶⁵ These defects have large thermodynamic energies and higher tendency to evolve upon heating and initiating the decomposition process.

It is worth mentioning that nanoparticles formed at different sizes along the length of the nanotube. More particles could be detected (Figure 7.7a) in the vicinity of the STM tip while fewer particles could be observed in the areas far from the tip (Figure 7.7b and c). One reason for this could be defect density which gives rise to the decomposing at one end of nanotube, even though the theoretical calculations¹²¹ predicted that the center of the nanotube should have higher temperature in comparison to the ends. One should note that the assumptions in Ref. ¹²¹ may not be applicable to our experimental analysis. Some of these assumptions are (a) the current density in the contacts is three orders of magnitude smaller than in the wire, and the heat generation term within the contacts is neglected. This assumption cannot be the case in our experiments. (b) The current density is described by a step function, which might not be the case here. In our case, there are Schottky barriers at contact points, causing non-linearity in the I - V curves.⁷¹ (c) There are no “hot spots” within the wire, i.e., localized points of higher resistance than the surroundings, which also may not be true in our case due to structural/defect variation in the nanotubes.

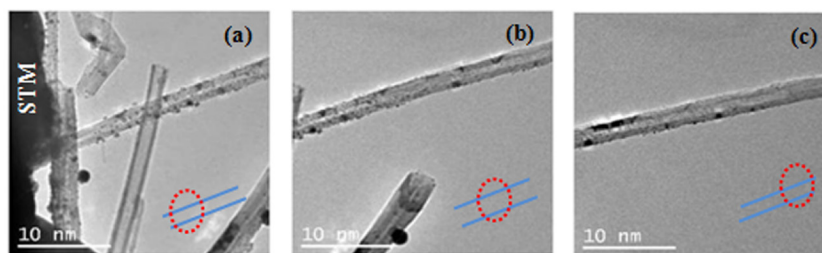


Figure 7.7 TEM images show variations in the density of nanoparticles during the thermal decomposition of a BN nanotube. Regions near the STM tip (a) with more particles indicate higher temperatures compared to zones further away from the STM tip (b and c). The locations of these TEM images are taken from different parts of the BNNT as schematically drawn in these images.

One should note that the decomposition of BNNTs cannot be due to electron beam exposure. If this was the case, then such decomposition phenomenon should also be seen during normal TEM imaging of BNNTs. But, in fact the formation of clusters was

observed only when the bias voltage was applied. In addition, the exposure to electron beam damage was minimized by expanding the beam over the entire screening area and the accelerating voltage was decreased from 300 to 200 Kv.

7.4 Conclusion

Thermal decomposition of individual BNNTs was studied via in-situ TEM imaging. Real-time monitoring shows that, with the Joule heating experiment, the BN nanotubes fail through the dissociation of atomic structure resulting in the formation of nanoparticles with different sizes and population density. These particles form mostly on outer shell layers, and the presence of structural defects may act as the active site of dissociation event. Such information is invaluable for designing robust nanotube-based electronic circuits subjected to current flow.

Chapter 8 -*IN-SITU* ELECTROCHEMICAL LITHIATION/DELITHIATION OBSERVATION OF INDIVIDUAL AMORPHOUS SI NANORODS

The material contained in this chapter was previously published in the ACS Nano (Reprinted with permission from H. M. Ghassemi, M. Au, N. Chen, P. A. Heiden, and R. S. Yassar, ACS Nano 5 (10), 7805-7811 (2011). Copyright 2011, American Chemical Society).

8.1 Introduction

Although the idea of batteries are simple, surprisingly their development has progressed much slower than other areas of electronics.¹²² This time-consuming development is due to the lack of suitable electrode materials and electrolytes. Traditional lithium-ion batteries employ carbonaceous anodes with a capacity of 372 mAhg⁻¹. To obtain substantial enhancement in their specific capacity, it is vital to substitute carbonaceous anodes with those of greater capacity.

An attractive candidate to replace carbonaceous anodes is silicon which has the highest theoretical capacity, in excess of 4000 mAhg⁻¹ and low discharge potential upon intercalation of 4.4 Li atoms per Si atoms.^{40,123,124} The fundamental reason behind such high capacity is that in silicon anodes each Si atom can accommodate up to 4.4 Li atoms (Li₂₂Si₅),⁴⁰ while in graphite each carbon atom can accommodate 1/6 Li atom (LiC₆). A major drawback with silicon is that, upon driving Li into Si, a volume expansion of ~300%^{47,125} to 400%⁴⁸ occurs due to the formation of various phases such as Li₁₂Si₇, Li₇Si₃, Li₁₃Si₄, and Li₂₂Si₅.¹²⁶ This leads to induced-mechanical stresses large enough to fracture and pulverize Si into powder after the first few cycles of charging/discharging and eventually loss of electrical contact and capacity fade during cycling.^{124,127}

Recently, Chan *et al.*⁴⁸ studied the structural stability of Si nanowires (NW) under the lithiation/delithiation process. Despite the high capacity at the first cycle (~ 4277 mAhg⁻¹), the Si NW anodes showed an irreversible capacity loss (~1300 mAhg⁻¹) in the 1st charge-discharge cycle. Several scenarios may have happened including the formation

of the solid electrolyte interface (SEI) and loss of active material, the difficulty in decomposition of Li-Si phases that forms during the first charging process, and the exfoliation of the active material (Li_xSi) from the electrode due to the large volume expansion caused by the alloying of Li with Si.

In theory, the one-dimensional morphology of the Si NWs was expected to improve the capacity retention of anodes due to better accommodation with lateral strains generated due to Li intercalation in the NWs. However, it is now widely known that the Si NWs have poor cyclability retention due to the fracture and pulverization of Si NWs.¹²⁴ The fracture of nanosized Si wires contradicts the suggested idea that below a certain size particles do not fracture.^{128,125}

To better understand the lithiation/delithiation process in nanostructured materials, *in-situ* studies of electrochemical reactions inside high resolution electron microscopes have been proposed. Wang *et al.*¹²⁹ built a miniature prototype battery using LiCoO_2 as the cathode, SnO_2 nanowire as the anode, and an ionic liquid-based as the electrolyte to study the interface of Li ion batteries inside a transmission electron microscope (TEM). Their observation provided direct imaging of the conversion of SnO_2 to Li_xSn_y and Li_2O during charging cycle. However, due to lack of detailed study, the reaction(s) during the lithiation process, as well as the formation of phase(s), were not discussed. Briazer *et al.*¹³⁰ reported the first *ex-situ* TEM observation of the cross-section of a nanobattery made by stacking layers of anode and cathode to study the interface behavior, all in solid-state. Their observation indicates a rapid deterioration of the interface upon cycling due to chemical elements immigrating between the stacked layers. Recently, Huang *et al.*¹³¹ reported the real time formation of “Medusa zone” during the lithiation of SnO_2 nanowires. The formation of this zone induced large mechanical distortion and, consequently, degradation in structural properties.

Amorphous and crystalline Si have a similar specific capacity to store Li^+ ; however, studies^{132,133,134} have shown that homogenous volume expansion in amorphous Si causes less pulverization and better cycling performance. Very recently, Huang *et al.*^{135,136} reported the anisotropic swelling as a result of lithiation of crystalline Si NWs using *in-situ* techniques. Formation of dumbbell-shaped cross section led to formation of

crack in the middle of NW along its axis. One expects that since there is no long-range order in amorphous structure or preferred diffusion path, the diffusion of the same amount of Li can occur more uniformly. Here, we investigated the lithiation of individual amorphous Si nanorods using an *in-situ* electrochemical setup inside of TEM technique. Two different diffusion paths, longitudinal and radial, were examined and the formation of Li_xSi phases were confirmed by diffraction pattern studies that agree with our *ex-situ* lithiation results.

8.2. Experimental Procedure

The pure Si nanorods were fabricated by an oblique angle (co)deposition technique in a custom designed two-source electron-beam deposition system.¹³⁷

Individual Si NRs were then attached to a gold wire by light mechanical scratching on the as-grown samples. As a result of van der Waals forces, individual NRs stick to the wire in different directions. The piezo-driven holder allows nanometer motion of the sample toward the AFM tip. Sample position can be adjusted with a precision of 1 nm in X, Y and Z directions. High-resolution TEM images and electron diffraction patterns were collected to characterize the formation of different phases during the lithiation of different individual Si NRs.

8.3. Results

8.3.1 Selective Lithiation of Si NRs

Figure 8.1a depicts the *in-situ* lithiation setup where a drop of IL is placed on the STM tip and individual Si NRs are placed on the gold wire. Then by the help of piezo-driven stage, the gold wire is moved toward the STM tip until an individual Si NR is in contact with the IL (Figure 8.1a). The applied bias voltage, in range of 3-4 V, introduces surface tension to the IL stream on the NR which causes Plateau-Rayleigh instability phenomenon,¹³⁸ and breaks the stream into droplets as shown in Figure 8.1b.

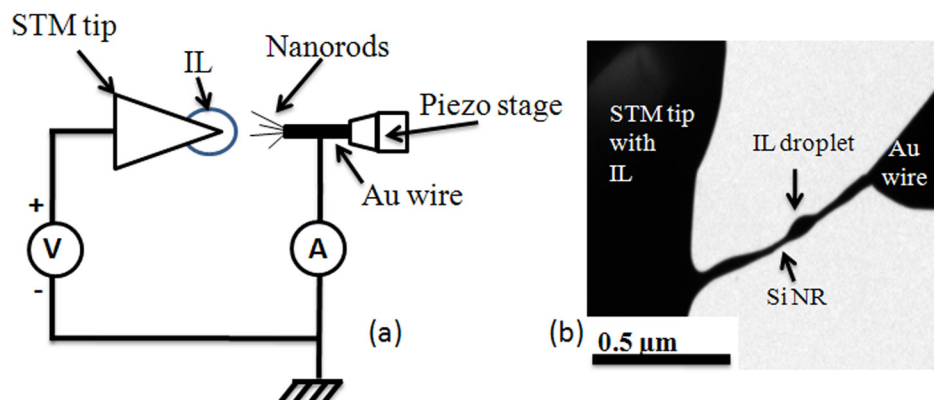


Figure 8.1 (a) Schematic of STM holder experimental setup. As the STM tip is positively biased, IL flows on the nanorods and Li ions diffuse into nanorods. (b) Shows the low-magnification image during the lithiation experiment. The arrow indicates a droplet as the IL flows on the Si NR (the other arrow) from the STM side to the gold wire.

Figure 8.2 shows still images of an *in-situ* video showing the effect of lithiation on the geometrical structure of Si nanorods. The yellow arrows indicate the main diffusion path for Li^+ into the NR, as that is the contact point between the NR and ILs. The red arrows in Figure 8.2 indicate the preferential locations where significant volume straining was observed. In Figure 8.2a, the ionic liquids containing Li ions are located on the far left side of the image and the Si NR was brought into contact with ILs. In less than two seconds, the first changes were observed on the tip of NR (Location 1) and an area very close to the tip (Location 2), as shown by the red arrows. These areas of the NR continued to grow and became larger in size, however, their growth was almost stopped after 14 seconds and another area (Location 3) started to expand in volume (Figure 8.2c). This location of nanorod continued to grow as shown by the red arrows in Figure 8.2c-f. Also, the radial straining is marked on Figure 8.2a-f and measured to be almost 10%. The volume expansion in Si during lithiation is due to the formation of Li_xSi phases.^{40,48,131}

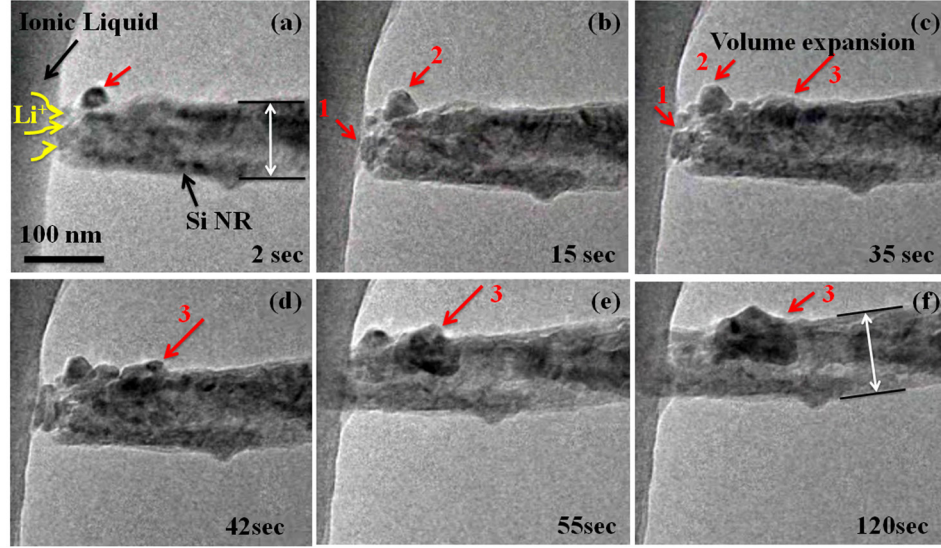


Figure 8.2 Snapshot series of lithiation process represents the swelling or radial straining at selective locations (indicated with red arrows) of a Si NR.

Overall, two important observations can be made here. First, the lithiation process does not start only at the contact point where the IL and NR meet. The process rather starts at selective areas close to the surface of NR. This is somewhat in contrast with the recent observation of the lithiation process in crystalline SnO_2 nanowires where the lithiation process was propagated into the nanowire from the interface.¹³¹ In principal, due to surface coverage of ionic liquids on the nanorod, the surface diffusion, which has lower activation energy compared to that of bulk, can be a faster path for the Li ions to be transferred to the nanorods. In this scenario, the Li ions will face larger barrier energy to diffuse into bulk Si in comparison to the surface channels.^{139,140} It is shown by Gai *et al.*¹⁴¹ that due to the reduced energy barriers in nanomaterials, formation of the $\text{Li}_{12}\text{Si}_7$ phase takes place at lower temperature and applied voltage compared to that of the bulk Si structure.

Second, there is selectiveness to the lithiation locations within the nanorod. Initially, Locations 1 and 2 became lithiated and then Location 3 grew. While it is unclear why the lithiation is localized in particular areas, speculations can be made on the presence of structural disorder within the Si nanorods. The switching from Locations 1 or 2 to Location 3 can be explained by the fact that upon lithiation and associated nano-

scale crack formation during volume straining, the diffusion path for Li ions will be disconnected. The interruption in Li channels will result in the stoppage of volume growth and consequently the lithiation of other locations.

In order to identify if the observed structural features are due to the insertion of lithium into the NR, a number of experiments were conducted with the same IL but with no lithium content. Figure 8.3a shows an amorphous Si NR that is in contact with the IL. It can be seen that after 60 minutes of being in contact with ILs with no Li content (Figure 8.3d), no detectable deformation and/or phase formation was observed. The diffraction pattern shown in the insets of Figure 8.3 a&e also indicate that the structure of Si NR remained amorphous after 60 min. Therefore, the formations of particles observed in Figure 8.2 are due to the diffusion of the Li into the Si NR and consequently the formation of Li_xSi phases.

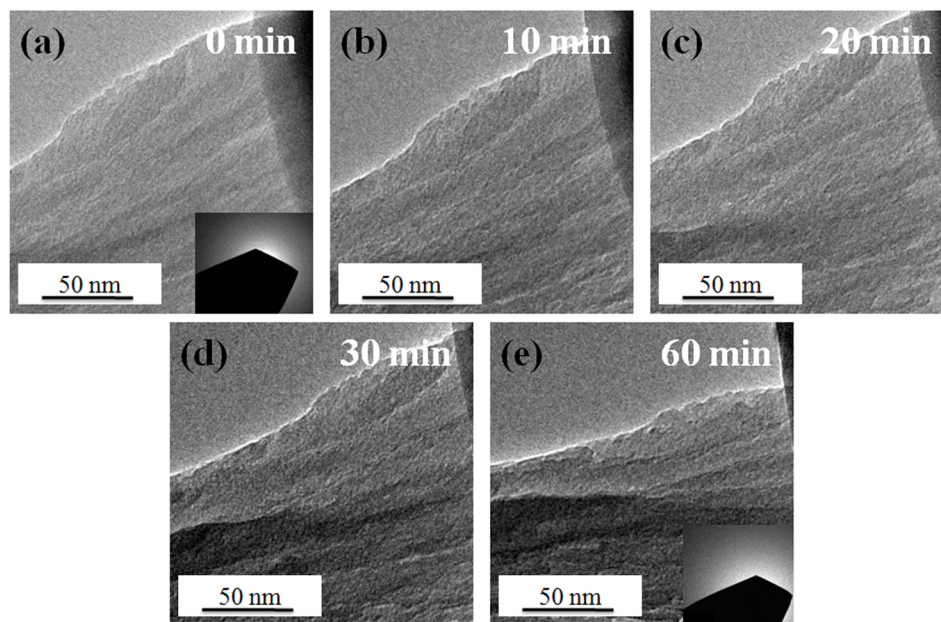


Figure 8.3 An amorphous Si NR in contact with the IL that has no Li content at (a) 0 min, (b) 10 min (c) 20 minutes, (d) 30 min, (e) 60 min. Insets in (a) and (e) show the diffraction pattern of the Si NR initially and after 1hr of experiment.

8.3.2 *In-Situ/Ex-Situ* Phase Transformation during Lithiation

In order to understand if the phase transformations observed during the lithiation of Si NRs were assisted by the electron beam radiation, the structure of the *in-situ* lithiated nanorods was compared with the ones lithiated *ex-situ*. The *ex-situ* experiments were conducted in a half cell where a beaker cell of Li-ion battery was constructed in a VAC (Vacuum Atmosphere Cooperation) glove box filled with argon gas.

Figure 8.4 compares the high-resolution TEM images and diffraction patterns of an *in-situ* lithiated nanorod and an *ex-situ* lithiated nanorod. In Figure 8.4a&b, the bright field TEM images of *in-situ* and *ex-situ* lithiated nanorods are shown in low magnifications. Both nanorods have similar distribution of dark contrast particles. These particles formed during the charging cycle and are expected to be various forms of Li_xSi phases. Interestingly, these particles are crystalline, which means that amorphous Si transforms to crystalline Li_xSi during lithiation. Figure 8.4 c&d show HRTEM images of the $\text{Li}_{22}\text{Si}_5$ particles. The d spacing was measured to be 0.34 nm in *in-situ* lithiated sample which is in good agreement with that of the *ex-situ* lithiated samples and other reported results.¹⁴² Due to the crystallinity of these phases and associated strain energy of their formation, one expects these particles to be darker in comparison to the surrounding amorphous matrix. The analysis of the diffraction patterns shown in the Figure 8.4e&f indicate that these Li_xSi particles are in fact $\text{Li}_{22}\text{Si}_5$ phases. This study indicates that the *in-situ* lithiation experiments in TEM are in complete agreement with the *ex-situ* charging tests and therefore the electron-beam assisted modification of Li ion diffusion can be ruled out. In addition, one should note that the phase identification in this study has been mainly based on HRTEM and diffraction analysis. In future research, it will be interesting to study the possibility for the existence of any Li_xSi amorphous phases using electron energy loss spectroscopy (EELS).

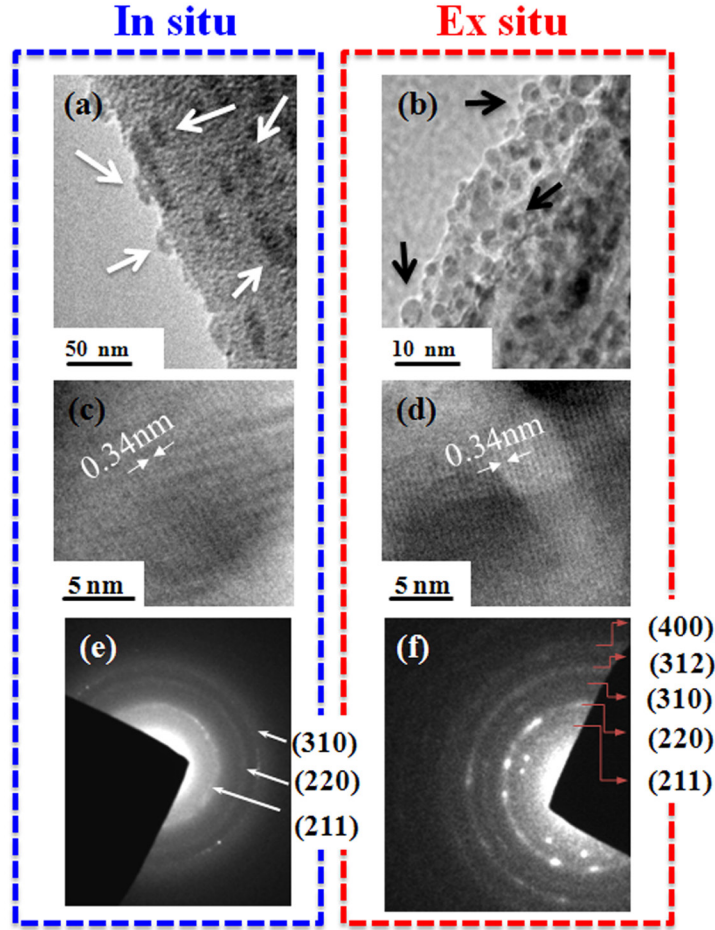


Figure 8.4 (a) An *in-situ* charged Si NR contains several particles of $\text{Li}_{22}\text{Si}_5$ phase marked by white arrows. Similar particle morphology was observed in the *ex-situ* fully charged Si NRs as shown in (b). (c) and (d) represent the HRTEM images of the $\text{Li}_{22}\text{Si}_5$ particles indicating the crystalline nature of the lithiated phase. The d spacing as shown in (d) measured to be 0.34 nm. (e) and (f) illustrate the electron diffraction patterns of the lithiated NRs in *in-situ* and *ex-situ* experiments, respectively.

According to the Li-Si phase diagram,¹⁴³ various forms of Li-Si alloys can form including LiSi, $\text{Li}_{12}\text{Si}_7$, and $\text{Li}_{22}\text{Si}_5$. One expects the formation of a series of the Li_xSi_y phases as the concentration of Li increases in the Si structure. However, in this study we only observed the direct formation of the $\text{Li}_{22}\text{Si}_5$ phase inside the amorphous Si. This is in contrast with the x-ray diffraction (XRD) results of Obrovac *et al.*¹⁴⁴ and Hatchard *et al.*¹⁴⁵ where $\text{Li}_{15}\text{Si}_4$ was identified to be the fully lithiated phase during the lithiation of Si at room temperature.

This apparent discrepancy can be explained from both thermodynamic and kinetic points of view. The standard Gibbs free energy for $\text{Li}_{22}\text{Si}_5$ is calculated to be -273 Kcal/mol as opposed to that of $\text{Li}_{12}\text{Si}_7$ which is -199 Kcal/mol.¹⁴⁶ Hence, from the thermodynamic point of view, the direct formation of crystalline $\text{Li}_{22}\text{Si}_5$ is expected to be more favorable than amorphous silicon. One should also note that the structure of Si nanorods is amorphous, meaning that no long-range order in atomic arrangements exists. This disordering in the structure of amorphous Si can act as diffusion channels for the Li ions to transport faster than the crystalline Si.¹⁴⁷ Therefore, from the kinetic point of view, there is higher tendency to form the fully lithiated (and the most stable) form of Li-Si alloy. Measurements by Wilkening *et al.*¹⁴⁷ also indicated that activation energy of amorphous LiNbO_3 is less than 1/3 of microcrystalline one. Therefore, diffusivity of elements such as Li in amorphous structures is much higher than that of the nanocrystal and microcrystal ones. The last point is that the results from both Obrovac *et al.*¹⁴⁴ and Hatchard *et al.*¹⁴⁵ showed that there was a critical thickness of 2 μm above which the crystalline $\text{Li}_{15}\text{Si}_4$ could form. In the case of NRs, since the diffusion path for the Li atoms is significantly lower than that of the above-mentioned thick layers of a-Si, each Si atom can be surrounded by higher number of Li resulting in the formation of $\text{Li}_{22}\text{Si}_5$. Experimental results from another group also confirmed the formation of $\text{Li}_{22}\text{Si}_5$ phase and 4200 mAhg^{-1} storage capacity was reported.⁴⁷

8.3.3 The Effect of Contact Area in Ionic Liquids-Nanorods Interfaces

Figure 8.5 depicts the *in-situ* lithiation process for the two different cases where Si NRs and ILs are in contact with each other. In Figure 8.5a, the tip of a Si NR is in contact with IL (the Li^+ path is shown schematically) and the lithiated Si NR is shown in Figure 8.5b. As discussed before, the formation of $\text{Li}_{22}\text{Si}_5$ phases were observed (marked by arrows). The overall radial straining of this NR was measured to be $\sim 10\%$. Figure 8.5c shows an individual NR where the sides of the NR are in contact with IL. In order to better show the structural changes, three TEM images were overlaid. The sides of the NR (1) are in contact with IL and the NR (2) and NR (3) were used to designate the region

where the radial straining was observed (Figure 8.5c). The initial diameter of NR (1) was measured to be ~ 26 nm and its amorphous structure is shown in the inset of Figure 8.6c. Similar to the case in Figure 8.5b, the formation of $\text{Li}_{22}\text{Si}_5$ phase was observed as indicated by arrows in the inset of Figure 8.5d. The NR (1) expanded from 26 nm to 70 nm as a result of Li insertion that can be estimated to be close to 270% straining in a radial direction. Note, our intention is mainly to capture the swelling of the NRs rather than the total volume straining. Therefore we did not keep track of the longitudinal straining of the NRs as they perhaps elongate into the ILs.

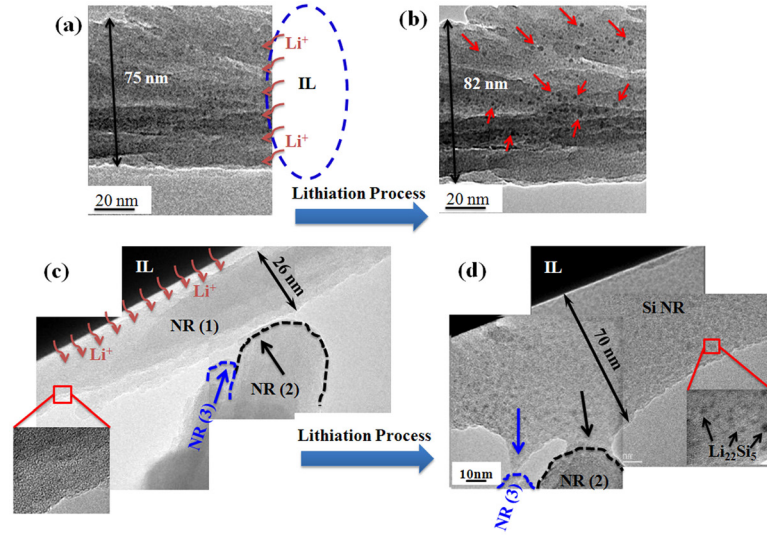


Figure 8.5 (a) An individual Si NR that is in contact with the IL before lithiation. The Li ion diffusion is along the axis of the nanorod. Image in (b) shows the NR after lithiation process with straining of $\sim 10\%$ in diameter. (c) Individual Si NR in contact with IL from the side surface. The thickness of the NR was measured to be 26nm before the lithiation and high resolution image (inset) shows the amorphous structure of NR before lithiation. (d) After the lithiation process, the diameter of NR expanded to 70nm. Inset shows a high-resolution image of $\text{Li}_{22}\text{Si}_5$ particles formed as a result of lithiation.

Inside a conventional Li-ion battery, anodes and cathodes are actually immersed into the electrolyte. However, in the case where only the tip of NRs was in contact with the ILs (Figure 8.6a), the regions of the NR close to the IL source were exposed to a higher Li density compared to the areas away from the NR. This can also explain why the majority of lithiation activities in Figure 8.2 were observed in areas close to ILs. In the

case where the side of Si NRs is immersed into ILs (Figure 8.6b), Li ions have a larger surface area to diffuse into the NR. Therefore, one expects the NR to expand more in order to accommodate the volumetric strains. Therefore, increasing the surface area with an electrolyte in Si NRs in ILs can better mimic the real-condition of battery charging.

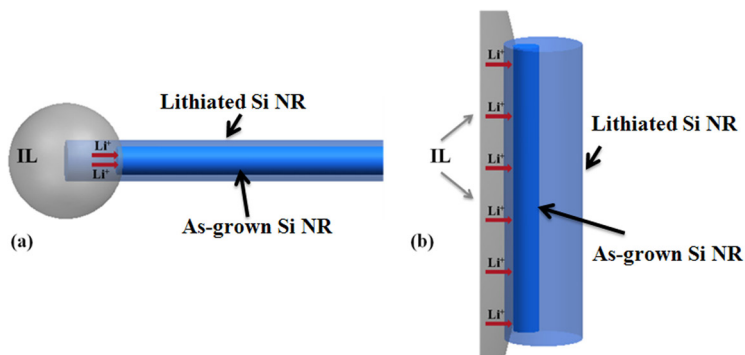


Figure 8.6 Schematics of two cases of interactions at IL-NR interfaces are shown. Schematic (a) illustrates the case where IL is in contact with the tip of a Si NR. Schematic (b) represents a case where the sides of NR are dipped into the IL.

8.3.4 *In-Situ* Delithiation Process

By reversing the applied bias on the lithiated NR, the discharging process can be studied. A nanorod was lithiated inside TEM as shown in Figure 8.7Ia-Ic, and 15% straining in diameter was measured. By comparing Figure 8.7IIa-IIc, one can see that the density of small particles was increased as a result of decomposition of larger particles upon delithiation. Also, the *in-situ* delithiated NRs show 10% shrinkage in overall diameter as a result of Li deintercalation. The shrinkage in diameter is due to the decomposition of $\text{Li}_{22}\text{Si}_5$ to the structures with smaller unit cell volume (for instance $\text{Li}_{12}\text{Si}_7$ in Ref. ¹⁴⁸) or full extraction of Li ions from $\text{Li}_{22}\text{Si}_5$ phase. In fact, the white arrows in Figure 8.7II-a and II-c point out a particle that completely vanished during delithiation. In addition, in comparison to the initial diameter (Figure 8.7I-a), the delithiated NR (Figure 8.7II-c) has a larger diameter by 5%. This residual straining means that some of the Li ions that intercalated into Si did not leave the Si structure upon delithiation. This conclusion also explains the irreversible capacity loss that has been observed in Si structures.^{124,48}

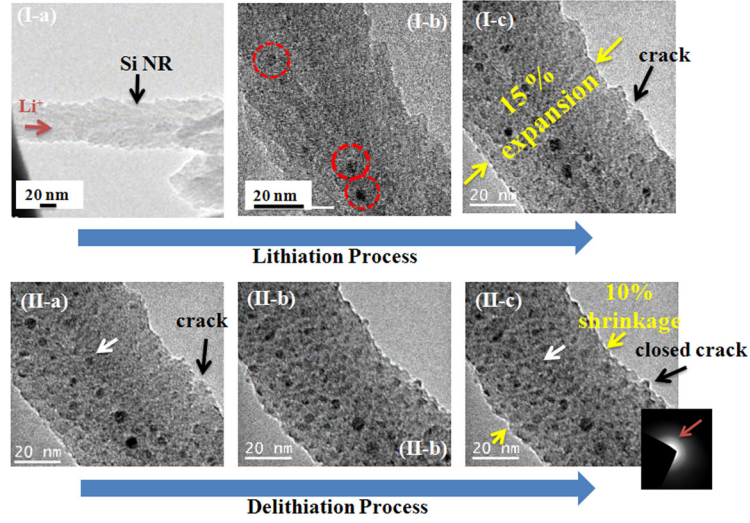


Figure 8.7 (I-a to I-c) *In-situ* lithiation of an individual Si nanorod. Images on (I-b) and (I-c) represent the formation of $\text{Li}_{22}\text{Si}_5$ after 20 and 30 min, respectively. The arrow in Image (I-c) indicates a crack formed on the surface of Si NR during lithiation process. (II-a to II-c) The delithiation process is shown. The white arrow in image (II-a) points to a $\text{Li}_{22}\text{Si}_5$ particle that disappears during delithiation process as shown in (II-b) and (II-c). In addition, a crack closure can be seen by comparing the images (II-a) and (II-c) and tracking the black arrow.

It is generally speculated that the reduction of size in silicon to nanometer range should improve its fracture toughness during lithiation.^{128,149,150} However, mechanical failure in the form of crack formation was observed in our lithiated NRs. This means that the induced-mechanical stresses due to lithiation can be large enough to initiate cracks and eventually to pulverize nanoscale silicon into particles. Huggins and Nix¹²⁸ calculated the critical size for fracture of a particle subjected to lithiation as below:

$$h_c = \frac{23}{\pi} \left[\frac{3k_{1c}}{B\varepsilon_T} \right]^2 \quad (8-1)$$

where, h_c is the critical size, K_{Ic} is the fracture toughness in $\text{MPa}\sqrt{\text{m}}$, B is the biaxial Young's modulus of the material and ε_T is the total strain. For silicon, the fracture toughness is $10 \text{ MPa}\sqrt{\text{m}}$ and the strain due to formation of $\text{Li}_{22}\text{Si}_5$ is $\approx 400\%$.⁴⁸

Therefore, the critical size under which the fracture does not happen can be estimated to

be 75 nm. Here, the cracks were detected in the 55 nm Si NRs (marked by a dark arrow in Figure 8.7II-a), which contradicts the theoretical predictions given in.¹²⁸ In our case, Si NRs with diameters less than 26 nm did not show crack formation upon lithiation (Figure 8.5d). This means that the theoretical models should be corrected in order to predict the true critical size scale below which one should not expect cracking in Si upon lithiation. However, it should be kept in mind that deterministic conclusion on an exact size scale will be too speculative at this stage due to lack of statistical analysis.

8.1 Conclusion

In summary, one life-cycle of lithiation/delithiation process on a nanobattery was performed using an *in-situ* electrochemical setup inside a transmission electron microscope. Direct formations of $\text{Li}_{22}\text{Si}_5$ particles were recorded. Our results show that the NRs are subjected to higher radial straining when there is larger surface area for the diffusion of Li ions into the Si nanorods. The results suggest that there is a size-scale regime beyond which the fracture toughness of Si nanorods is larger than the strain energy required to induce cracking in Si nanorods. The Si nanorods with diameters of 26 nm did not fracture upon lithiation while nanorods with 55 nm were cracked. In addition, $\text{Li}_{22}\text{Si}_5$ particles were not fully decomposed when subjected to delithiation. This observation can explain the irreversible capacity loss in Si structures used in Li-ion battery technologies.

Chapter 9 -REAL-TIME OBSERVATION OF LITHIUM FIBERS GROWTH INSIDE A NANOSCALE LITHIUM-ION BATTERY

The material contained in this chapter was previously published in the ACS Nano (Reprinted with permission from H. M. Ghassemi, M. Au, N. Chen, P. A. Heiden, and R. S. Yassar, Applied Physics Letters **99**, 123113 (2011). Copyright 2011, American Institute of Physics).

9.1 Introduction

Lithium-ion batteries are of great interest due to their high energy density, however, various safety issues such as lithium dendrite formation limit their practical application.^{151,152} The formation of the lithium dendrite⁴⁹ or accumulation of mossy lithium¹⁵³ on the anode electrode can create short-circuit after several lithiation-delithiation cycles, causing high-rate discharge. In a severe case, when a high rate of overcharging is applied to the cell, it can catch fire or even explode.¹⁵² It was found that there is a direct relationship between the current density and dendrite formation using scanning electron microscopy.¹⁵¹ While more than two decades ago^{154,155} polymer electrolytes were proposed as a solution, their application remains limited because of the high working temperature need to achieve ionic conductivity of the polymer.¹⁵⁶

Ionic liquids (ILs), discovered by Wilkes *et al.*,¹⁵⁷ are liquid-like salts that are composed solely of ions and have high ion conductivity with no structural variations. Due to their physicochemical properties, many applications are possible.^{158,159} One is the electrolyte of the lithium-ion batteries, where high ionic conductivity and zero electrical conductivity are needed.¹⁶⁰ However, despite the improved cycling performance compared to the traditional electrolytes, the formation of lithium dendrite still occurs at practical current density.¹⁶¹ Therefore, it is crucial to understand the mechanism of the formation of lithium fibers to enable the safe and secure use of lithium-ion batteries in mobile applications.

To understand the Li fiber growth in ionic-liquid based batteries, we performed *in-situ* lithiation experiments using Si nanorods (NRs) as the anode, LiCoO₂ as the cathode, and 1-butyl-3-methylimidazolium (BMIMCl) ionic liquids (ILs) as the electrolyte. The lithiation process was conducted inside a transmission electron microscope (TEM) and the formation of Li fibers was observed. During the *in-situ* experiments, the beam was expanded and condenser lens apertures were used to minimize the beam intensity and radiation.

9.2. Experimental Procedure

Aligned silicon nanorods were grown on the Cu substrate using a glancing angle deposition technique. The details of nanorod fabrication were reported in our previous publication.¹³⁷ LiCoO₂ powder, purchased from Sigma-Aldrich, and was used as cathode materials. A small amount of the cathode powders was glued on a gold wire and the anode material was glued to the scanning tunneling microscope (STM) side (Nanofactory™ STM sample holder). The gold wire with cathode and ILs was then placed on a hat, which sits on the sapphire ball of the sample holder. The applied bias voltage introduces surface tension to the IL stream on the NR, which breaks the stream into droplets according to the Plateau-Rayleigh instability phenomenon.¹³⁸ Here, we biased the cathode -3.5V in relationship to the anode materials to initiate the releasing of the Li⁺.

9.3. Results

Figure 9.1a represents a schematic of the *in-situ* experiment set-up inside the TEM. As can be seen, the cathode is mounted on the gold wire and the Si NRs are placed on the STM electrode. Figure 9.1b represents a typical configuration of a nano-battery where the anode and ILs are in contact. Figure 9.1c shows that a thin layer of the IL is formed due to the stream of the ILs in the presence of the applied voltage. Figure 9.1d depicts a typical amorphous NR after one hour of the lithiation process, where arrows indicate the formation of Li₂₂Si₅ phase with their electron diffraction pattern (EDP) shown in the inset.

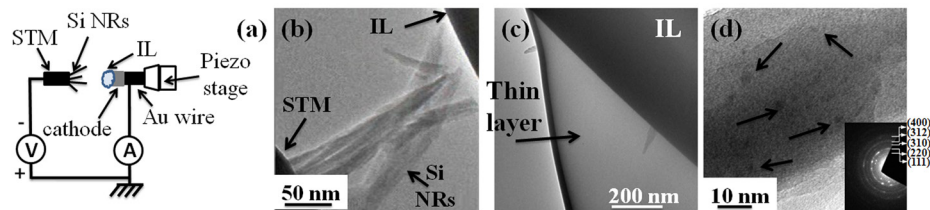


Figure 9.1 (a) A schematic of the in-situ lithiation setup is shown where the anode is placed on the STM and the IL is placed on the cathode. (b) The TEM image shows a nano-battery configuration in which the Si NRs are in contact with the ILs prior to the lithiation experiment. (c) The formation of a thin layer of ILs on the surface of ILs (the darker region) is shown. (d) The TEM image of Si NR structure after 1 hr of lithiation. Arrows indicate the $\text{Li}_{22}\text{Si}_5$ particles that are formed. Inset represents a diffraction pattern of the lithiated Si NR indicating the presence of the $\text{Li}_{22}\text{Si}_5$ phase.

The growth of Li fibers was investigated by focusing on the evolution of IL-Si NR interface. Figure 9.2a shows an IL droplet just before the lithiation process begins, while the diffraction image in the inset shows a fuzzy pattern that indicates no crystalline ordering presents. After the lithiation experiment took place, the formation of small islands was observed on the IL (Figure 9.2b). The diffraction pattern in the inset of Figure 9.2b confirms that these islands have a crystalline order similar to Li metals.

A snapshot series of the formation of Li islands in the IL is shown in Figure 9.2c-g. The black arrow in Figure 9.2c-f follows the evolution of IL during the lithiation process (Movie 1, Supplementary Documents). One can see that behind the movement of the IL, small islands of Li remain (shown by the red arrows). The islands appear to have random distribution. One can also notice that the islands do not move in the Movie. Note, the lithiation experiments conducted for 60-90 minutes and the Movies in Supplementary documents only represents few minutes of the formation and growth of Li fibers which might be quite short to notice any movement of the islands. The inset in Figure 9.2g shows the EDP of the islands that confirms the formation of the crystalline lithium islands. Note, the ILs have a low tendency to crystallize due to flexibility (anions) and dissymmetry (cations),¹⁶⁰ hence the EDP spots can only be correlated to the lithium contents.

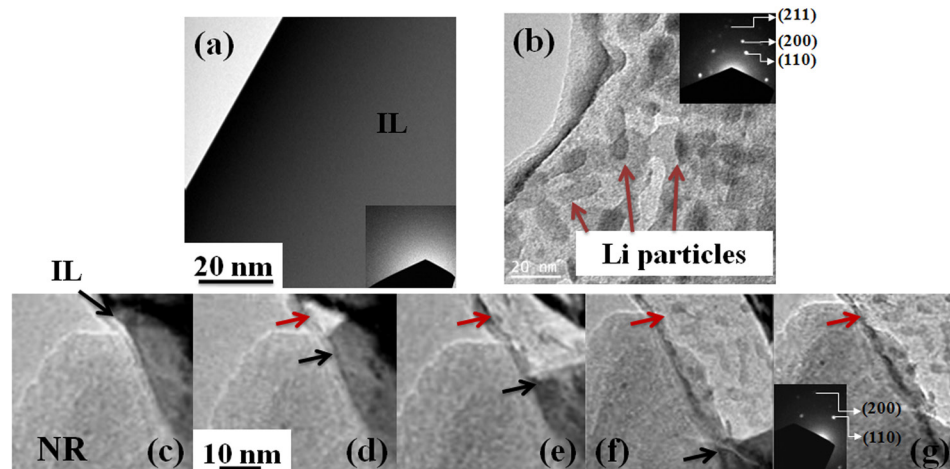


Figure 9.2 (a) Represents a typical surface of ILs prior to the lithiation process; the EDP in the inset shows no crystalline ordering can be found within the IL. (b) The nucleation of Li fibers during the lithiation process. The EDP in the inset indicates the crystalline ordering within the IL. (c-g) Series of snapshots taken from the real-time video indicate the appearance of the Li fibers at various stages. The inset shows that the newly formed fibers have crystalline orders.

Wang *et al.*¹⁶² reported the changes in the distributions of anion and cations under high electric field. His simulation study showed that, by increasing the externally applied electric field, the ILs structure changed from spatially heterogeneous to spatially homogenous and then to nematic-like. On the other hand, when the external electric field is comparable to the electrostatic interactions between the cations and anions, the system acts like a simple liquid with more freely moved ions.

Figure 9.3 shows the subsequent stages of Li islands growth. Figure 9.3a shows a Si NR that is dipped into ILs from both sides. After almost 30 minutes of the lithiation process, one can see the formation of lithium fibers as indicated with white arrows in Figure 9.3b. As one expects, the growth of the Li fibers is in the same direction as that of the applied electric field. Figure 9.3c and d represent the growth of lithium fibers toward the cathode (Movie2 in the Supplementary Documents). This is in agreement with the previous report that shows that lithium fibers form on the surface of the anode material and grow toward the cathode, inside the electrolyte, due to the presence of an electric field.^{49,163,131}

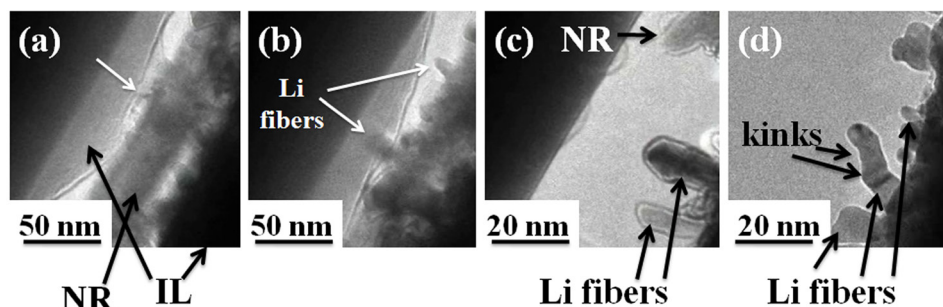


Figure 9.3 (a) Black arrows indicate an individual NR surrounded by IL. (b) Arrows indicate the formation of Li islands on the NR. (c) Represents the growth of Li fibers. (d) The formation of kinks and growth of Li fibers are marked by black arrows.

One can observe that each of the fibers grows rapidly to a certain length and then slows or even stops and another fiber starts to grow (Movie 2, Supplementary Documents). As the fibers grow, it seems that their length increases but the diameter remains constant. The formation of kinks on the fibers during the growth stage was also observed (as marked in Figure 9.3d). Note, the Movie 1 was captured from the early stage of lithiation process, when the nucleation of Li islands took place inside the IL. The Movie 2 represents the final stage of Li growth in the form of fibers on the surface of the anode. These observations are in good agreement with the reported SEM observations.¹⁶⁴ It was first reported¹⁶⁵ that lithium deposits on the anode as needle-like during lithiation. Upon delithiation process, if the dissolution current is larger than deposition current, then they detach from the anode surface and float into the electrolyte. These so-called “dead-Li” are electrochemically inactive but chemically active due to their large surface area and responsible for the loss of cycling performance of the battery.

Runaway reactions can take place between the cathode and anode, risking explosion and fire.¹⁶⁶ Therefore, from a practical point of view, it is necessary to prevent unwanted reactions and phenomenon due to the growth of lithium fibers. A number of methods have been proposed to increase the safety of Li-ion batteries including the replacement of the organic electrolyte with ionic liquids. However, the results of this study shows that the Li fibers can nucleate and grow in such ionic liquid electrolytes.

Therefore, further studies should be pursued to design the electrolytes that prevent the growth of Li fibers.

9.4. Conclusion

A nanoscale Li-ion battery was constructed inside a transmission electron microscope to study the formation of lithium fibers during the lithiation process. The ionic liquids served as the electrolyte to enable the observation of electrochemistry process. Interestingly, it was observed that, in addition to the lithiation of Si NRs, some Li islands formed inside the IL. These islands continued to grow as Li fibers toward the counter electrode parallel to the applied electric field. The formation of Li fibers can induce possible short circuit and compromise the safety of the Li-ion battery. The experiments shown in this study can elucidate understanding of the formation and growth mechanism of the lithium fibers using different electrolytes to diagnose the safety issue toward the next generation of high performance Li-ion batteries.

Chapter 10 -DISCUSSION

Mechanical and electrical characterizations of one-dimensional nanostructures can be amazingly different than those of their bulk. Therefore, to utilize their applications, it is desirable to directly measure the properties of nanostructures and investigate their behavior in various environments. Furthermore, combination of mechanical and electrical characterization techniques enables researchers to conduct new experiments such as operating a nano-battery inside the electron microscope. Hence, several areas of interests can be studied and developed using *in-situ* techniques. Below is the discussion of our investigations on different properties of two different one-dimensional nanostructures, namely, boron nitride nanotubes and Si nanorods.

10. 1. *In Situ* Mechanical Characterizations of BNNTs

It was found out that the bending deformation behavior of BNNTs depends on the magnitude of the mechanical straining. We categorized the bending angle into two regimes. Under small-bending deformation, where the bending angle is less than 65°, several BNNTs recovered their original shape upon removing the applied force. In this regime, the nanotubes did not reveal any residual deformation. This behavior is highly desirable in fabrication of robust nanodevices such as rotational actuators.¹⁶⁷

In the next step, the buckling mechanism in multi-walled BNNTs upon severe mechanical deformation were studied, to better understand the elastic recovery of the BNNTs. High-resolution TEM images revealed that bent BNNTs form multiple rippling upon buckling. Our calculations also revealed that the critical strain to form the first ripple was 4.1% and the buckling process was reversible up to 26% strain. As opposed to carbon nanotubes, the BNNTs buckled into V-shaped ripples rather than smooth wavy shapes.

It is proposed that in the buckled region B-N bonds convert to B-B and N-N bonds, which is thermodynamically unfavorable to form. Therefore, as the applied force is released and the nanotubes return back to the original straight shape, the B-N bonds form again to minimize the overall energy of the system. In order to reduce the increase in the thermodynamic energy of the system during buckling, nanotube tends to form

buckles with larger wavelength to reduce the number of these unfavorable sites. This is different from the behavior of CNTs since the switched bond is still C-C. Hence, the thermodynamic energy of the system is not increased significantly and the wavelengths are reported to be shorter. These results revealed the underlying mechanism which is responsible for the high flexibility of the BNNTs.

Interestingly, BNNTs showed structural failure during the cyclic bending at large-angle of bending, up to 120°. The *in-situ* results revealed that the brittle failure mechanism was initiated from the outermost walls and propagated toward the tubular axis with discrete drops of applied forces. Force-displacement plot of a BNNT which was correlated to the fracture failure cycle indicated two distinct drops of the force before the failure was completed. These two drops represented the initiation and propagation in the nanotube's shell-walls. Furthermore, the cross-section of the fractured BNNT remained tubular and the inner channel could be clearly observed. These observations suggested that the breakage of the nanotube shells is brittle. Based on these observations, one can modify the design of a nano-device, flexible MEMS integrated circuit, in which BNNTs undergo extreme applied force.

10. 2. *In Situ* Electrical Characterizations of BNNTs

The electrical properties of pure BNNTs were then studied using *in-situ* techniques inside TEM. Our measurements showed only few nA current flow under applied bias voltage up to 80 V for pure and stress-free BNNTs, which further confirm the insulating behavior of BNNTs. Further calculation revealed the resistance of the BNNTs to be ~10 GΩ which is in good agreement with the reported values.⁹⁶ Therefore, it is shown that, for instance, BNNTs can be used as insulator coating in applications such as nano-cables.¹⁶⁸ These nano-cables, considering the high-mechanical stability of BNNTs, are suitable for application in harsh environments.

Next, the nanotubes were subjected to series of mechanical straining while *I-V* data was simultaneously collected. The applied stress changed the conductivity of BNNT; hence, higher electrical currents were detected at elevated strain levels. We then calculated the semiconducting parameters of the BNNTs as a function of applied stress. Results showed that the resistance of BNNT (dV/dI) can be tuned in a wide range of

2000-769 M Ω under minimum and maximum bending deformations. Calculations also indicated that the electron concentration increased by a factor of 3, however, the carriers mobility was decreased. The reduction in carrier mobility can be correlated to the scattering between electron-phonon under the applied electric field, or due to presence of impurities similar to the reported results for graphene.¹⁰³ These results revealed that the mechanical properties of BNNTs can be combined with tunable electrical characteristics to build future micro- and nano-electronic devices, such as nano-sensors.¹⁶⁹

Field emission (FE) characteristics of individual BNNTs were also measured and structural evolution were studied inside the TEM. The results revealed that the emission of electron starts at a particular voltage of ~ 65 V, also known as turn-on voltage, and exponentially increases to 140 nA at 110 V. The turn-on voltage is calculated to be ~ 325 V/ μm and the current density of an individual BNNT is measured as ~ 1 mA/cm² at voltage of 110 V. Our results revealed that by assuming the work function of pristine BNNT as 6 eV, field enhancement factor, β , is equal to 98. The FE experiments were repeated to further investigate the structural and emission stability of the BNNT upon four cycles of emission. The nanotube showed that in the 2nd cycle of FE, the turn-on voltage is increased from 65 V to ~ 80 V and the emission current dropped slightly to ~ 120 nA. FE cycles 3 and 4 represent further degradation of emission current as well as higher turn-on voltages, respectively. In the 4th cycle the amount of emission current drops almost 90% in comparison to the 1st cycle. The TEM analysis of the FE cycled nanotube revealed the likelihood of structural decomposition that can explain the reduction in the field enhancement factor. As the FE experiments were conducted, due to the high emission current density, the temperature of the sample is increased and reached to the decomposition temperature at which the B-N bonds start to break. The volatile nitrogen atoms leave the structure and are released into the vacuum while the B atoms remain. Therefore, as the nanotube decomposed, nitrogen which contributes 5 electrons compared to boron with 3 electrons leave the structure and emission current of the nanotube degraded significantly.

10. 3. *In Situ* Electrochemical Lithiation/Delithiation of Si Nanorods

In-situ electrochemical lithiation and delithiation of amorphous Si nanorods revealed the direct formation of $\text{Li}_{22}\text{Si}_5$ phase due to intercalation of Li ions. From the kinetic point of view, crystalline $\text{Li}_{22}\text{Si}_5$ phase tends to form, directly from the amorphous phase, as the highly lithiated (and the most stable) form of Li-Si alloy. Electron diffraction patterns along with high-resolution TEM images were also in good agreement with our *ex-situ* results. Therefore, the electron-beam assisted modification of Li-ion diffusion can be ruled out. It was also found out that the lithiation of Si was dominated by surface diffusion due to smaller barrier energy compared to bulk diffusion mechanism. It should be noted that nanostructures possess significantly higher surface area compared to the bulk materials. Selective diffusion of lithium also was observed, hence, there were different sites which were selectively lithiated during the experiment one after each other. This observation was somewhat in contrast with the recent observation of the lithiation process in crystalline SnO_2 nanowires where the lithiation process was propagated into the nanowire from the interface.¹³¹

In the next step, different tests were conducted to study the effect of contact area on the anode-electrolyte interface. *In-situ* observations revealed that when the tip of the nanorod is in contact with the electrolyte only 15% radial expansion took place as a result of lithiation process. However, when the nanorod was immersed into the electrolyte the radial straining of 270% was observed. Therefore, increasing the contact area between the electrolyte and anode material can better mimic the real-condition of battery charging.

To further analyze the Li intercalation in a life cycle of a battery, the direction of bias voltage was reversed to extract the lithium from Si nanorod. *In-situ* observations illustrated that most of the dark contrast, due to the formation of $\text{Li}_{22}\text{Si}_5$, disappeared upon delithiation process. However, some particles were still remained after delithiation process which indicated that some of the lithium was entrapped inside the anode. Therefore, upon the next lithiation process less amount of lithium can diffuse into the

anode material which means that the storage capacity is decreased. In another word, the initial capacity of Si anode cannot be obtained in the next (irreversible capacity loss).

After the delithiation process, one could notice that majority of the radial expansion of 15% was recovered. However, there was still 5% radial expansion left in the structure due to the presence of entrapped lithium. Interestingly enough, the crack which formed due to the radial expansion during the lithiation process was closed after the delithiation process due to shrinkage of the structure. Based on the proposed theory¹²⁸ on the critical size for fracture of a particle, Si nanorods with diameter below 75 *nm* should not form any crack during the lithiation. Comparing the lithiation process of nanorods with different diameters, we did not observe formation of any crack in a nanorod with diameter of 26 *nm*, which suggested that the fracture roughness is increased compared to a nanorod with diameter of 55 *nm*. Therefore, it was understood that to prevent the mechanical failure and pulverization of Si materials, amorphous Si nanorods with diameter of ~26 *nm* is a superior candidate.

A major safety issue with lithium-ion batteries is the formation and growth of lithium fibers on the anode surface. The formation of the lithium dendrite or accumulation of mossy lithium on the anode electrode can create short-circuit after several lithiation-delithiation cycles, causing high-rate discharge. Our study revealed that the growth of the Li fibers is in the same direction as that of the applied electric field. One can observe that each of the fibers grows rapidly to a certain length and then slows or even stops, and another fiber starts to grow. These fibers can be detached during the delithiation process and float into the electrolyte causing the loss of cycling performance of the battery. Thus, safety of the lithium-ion batteries can be elevated by preventing the formation and/or growth of the Li fibers on the anode surface.

Chapter 11 -Conclusions

In this research, mechanical and electrical properties of boron nitride nanotubes as well as electrochemical characterization of amorphous Si nanorods were investigated. BNNTs were grown on a silicon substrate using CVD techniques. *In-situ* characterization techniques were carried out inside TEM.

(i) *In-situ* study on the bending deformation of individual BNNTs revealed that the behavior is unlike under different regimes. At low bending angle ($\sim 65^\circ$) the nanotubes recovered their initial straight shape. For the high-angle ($\sim 120^\circ$) cyclic bending, *in-situ* TEM imaging allowed the real-time recording of the shell-walls failure initiation and propagation process. Brittle mechanism was observed for bending failure of BNNTs. The drops of the measured force corresponding to the failure of shell-walls determined the contribution of shell-walls on the overall strength of nanotubes.

(ii) High-resolution TEM images revealed that bent BNNTs form multiple rippling upon buckling. The rippling wavelength, λ , nanotube outer diameter, r , and thickness, h , are correlated through the relationship of $\lambda/(rh)^{0.5} = 1.45$. It was also found that the buckling was reversible up to 26% strain. As opposed to carbon nanotubes, the BNNTs buckled into V-shaped ripples rather than smooth wavy shapes. The BNNTs showed a larger rippling wavelength compared to that of CNTs with the same number of walls. This difference was explained by the tendency of BN structures to reduce the number of thermodynamically unfavorable B–B and N–N bonds at the sharp corners in the rippling regions. The BNNTs' structure also exhibited a higher fracture strain compared to their counterpart.

(iii) Real-time monitoring of the thermal decomposition of the BNNTs, under the Joule heating experiment, revealed the failure mechanism of the nanotubes. HRTEM showed that failure was due to the dissociation of atomic structure resulting in the formation of nanoparticles with different sizes and population density. These particles form mostly on outer shell layers, and the presence of structural defects may act as the active site of dissociation event.

(iv) Electrical measurements showed that individual BNNTs exhibit the current density of $\sim 1 \text{ mA/cm}^2$ at 110 V and turn-on voltage was 325 V/ μm . However, structural degradation was observed only after 4 cycles of emitting and the emission current dropped significantly. Measurements on the semiconducting parameters of individual BNNTs revealed that the band gap can be tuned by means of mechanical deformation. Based on the amount of strain, resistance of individual BNNT was engineered in the range of 2000-769 M Ω and electron concentration was calculated to be $0.35\text{-}1.1 \times 10^{17} / \text{cm}^3$ in that range of strain with slight decrease in the mobility of the carriers.

(v) The lithiation of individual Si NRs revealed that higher radial straining took place when there was larger surface area for the diffusion of Li-ions into the Si nanorods. The results suggest that there is a size-scale regime beyond which the fracture toughness of Si nanorods is larger than the strain energy required to induce cracking in Si nanorods. The Si nanorods with diameters of 26 nm did not fracture upon lithiation while nanorods with 55 nm were cracked. In addition, $\text{Li}_{22}\text{Si}_5$ particles were not fully decomposed when subjected to delithiation.

(vi) Study on the formation and growth of the lithium fibers on the anode materials revealed that in addition to the lithiation of Si NRs, some Li islands formed inside the IL. These islands continued to grow as Li fibers toward the counter electrode parallel to the applied electric field. The formation of Li fibers can induce possible short circuit and compromise the safety of the Li-ion battery.

Chapter 12 -Future Works

This PhD project was mainly focus on mechanical and electrical properties of pure multi-walled BNNTs as well as electrochemical characterization of Si anode nanorods. However, various aspects of these investigations were remained to be explored. Below, three future projects are proposed to further study and investigate *in-situ* properties of these materials.

12. 1. Chemical Effect on the Mechanical Properties of BNNTs

BNNTs can be doped with elements such as carbon resulting formation of BCN nanotube^{170,171,172,173,174} or be decorated by transition metals such as Ti or Pd on the outer or inner surface.^{175,176} In contrast to several theoretical studies,¹⁷⁷ experimental reports on various properties of doped-BNNTs are still limited. Therefore, the mechanical properties can be different because the B-N bonds convert to B-C and/or C-N bonds. These new nanostructures can be good candidate for nanoscale electronic devices and photonic applications.¹⁷⁸

To further understand the effect of chemical alteration on the mechanical properties, several *in-situ* experiments can be designed and performed. For instance, one can study the mechanical respond of the doped-BNNTs under applied force and investigate the deformation mechanism. As discussed in Chapter 6, BNNTs have potential applications in micro- and nano-electronic devices, for instance as nano-switches where the structure undergoes several loading-unloading cycles. Therefore, investigation on the structural stability of the doped-BNNTs under cyclic deformation is important. In case of fracture failure of the doped-BNNTs, one can compare the type failure mechanism to that of the pure BNNTs.

In addition to compression tests, tensile experiments can also be performed inside TEM.^{179,180} To perform a tensile test, one needs to weld the two ends of the nanotubes to the AFM tip and gold wire by focusing the electron beam on the contact points.^{174,181} Therefore, one can obtain the true stress-strain from the force-displacement plot, hence; the Young's modulus as well as the ultimate tensile strength can be calculated. These

results can be further analyzed and compared to that of the pure BNNTs to investigate the effect of chemical alteration on the mechanical stability of the nanotubes.

12. 2. Chemical Effect on the Electrical Properties of BNNTs

Some of the electronic applications of pure BNNTs might be limited due to their wide bandgap of ~ 6 eV. However, their electrical properties can be tuned by either straining or chemical alteration. The latter approach can significantly lower the bandgap, especially by means of conductive elements.^{96,110,182} Therefore, one can investigate the effect of doping elements on the bandgap, as well as its type.^{183,184}

The conductivity of doped-BNNTs is expected to be higher than that of the pure BNNTs due to reduction in the conduction band energy.¹⁸⁵ Following the calculations presented in Chapter 6, semiconducting parameters such as resistivity, electron concentration and carrier mobility can be calculated as a function of doping element and its concentration. Therefore, a comprehensive study is needed to investigate and understand the mechanism of bandgap alteration based on the type of the doping element.

Furthermore, the FE characteristics of doped-BNNTs are expected to enhance compared to that of the pure one. It is experimentally reported¹¹⁰ that gold enhances the field emission properties of the pure BNNTs. However, the effect of different doping elements is still unexplored and needs further investigations. By synthesizing different concentrations of each doping elements, the FE characteristics can be optimized. Moreover, the stability of the emission current can be investigated. As discussed in Chapter 6, structural decomposition can take place as a result of high emission current which leads to the degradation of the FE properties. From this point of view, the FE failure mechanism of doped-BNNTs is another step to explore.

12. 3. *In-Situ* Electrochemical Characterizations of Cathode Materials

Currently, majority of investigations in the lithium-ion batteries area are focused on optimization of the anode materials. However, to further develop high-power batteries for hybrid cars,^{186,187} the properties of cathode materials should also be investigated.¹⁸⁸ It

is shown that during charging-discharging cycles, the electrical conductivity of the cathode materials diminishes significantly.¹⁸⁹ It is also reported that in different cathode materials formation of oxide layer is responsible for this degradation and can be minimized by surface coating.¹⁹⁰

LiCoO₂ is one of the most commercially used cathode materials due to its convenience and simplicity of preparation. Even though the theoretical capacity is calculated to be 273 mAhg⁻¹, only ~140 mAhg⁻¹ can experimentally be obtained.¹⁹¹ Several studies were carried out to enhance the capacity by coating the cathode material¹⁹² as well as by means of their morphology and shape.^{193,194} To completely understand the phenomena responsible for the capacity retention upon extraction of Li⁺, *in-situ* techniques can be designed to characterize the phase transformation. It is also reported that over-delithiation can cause of ~9% volume shrinkage in the cathode materials which causes pulverization over life-time.¹⁹⁰

References

1. Gabor L. Hornyak THF, Dutta J., Moore J. J. . Introduction to Nanoscience and Nanotechnology. Golden, Colorado, USA, CRC Press, 2008.
2. Roduner E. Size matters: why nanomaterials are different. Chemical Society Reviews 2006;35(7):583-592.
3. Agrawal R, Peng B, Gdoutos EE, Espinosa HD. Elasticity Size Effects in ZnO Nanowires—A Combined Experimental-Computational Approach. Nano Letters 2008;8(11):3668-3674.
4. Débart A, Paterson AJ, Bao J, Bruce PG. α -MnO₂ Nanowires: A Catalyst for the O₂ Electrode in Rechargeable Lithium Batteries. Angewandte Chemie International Edition 2008;47(24):4521-4524.
5. Liu H, Kameoka J, Czaplewski DA, Craighead HG. Polymeric Nanowire Chemical Sensor. Nano Letters 2004;4(4):671-675.
6. Strelcov E, Lilach Y, Kolmakov A. Gas Sensor Based on Metal–Insulator Transition in VO₂ Nanowire Thermistor. Nano Letters 2009;9(6):2322-2326.
7. Takagi M. Electron-Diffraction Study of the Structure of Supercooled Liquid Bismuth. Journal of the Physical Society of Japan 1956;11(4):11.
8. Gojny FH, Wichmann MHG, Köpke U, Fiedler B, Schulte K. Carbon nanotube-reinforced epoxy-composites: enhanced stiffness and fracture toughness at low nanotube content. Composites Science and Technology 2004;64(15):2363-2371.
9. Wang XW, Fei GT, Zheng K, Jin Z, Zhang LD. Size-dependent melting behavior of Zn nanowire arrays. Applied Physics Letters 2006;88(17):173114.
10. Iijima S. Helical microtubules of graphitic carbon. Nature 1991;354(6348):56-58.
11. Song J, Jiang H, Wu J, Huang Y, Hwang KC. Stone–Wales transformation in boron nitride nanotubes. Scripta Materialia 2007;57(7):571-574.
12. Verma V, Jindal VK, Dharamvir K. Elastic moduli of a boron nitride nanotube. Nanotechnology 2007;18(43):435711.
13. Chopra NG, Zettl A. Measurement of the elastic modulus of a multi-wall boron nitride nanotube. Solid State Communications 1998;105(5):297-300.

14. Golberg D, Bai XD, Mitome M, Tang CC, Zhi CY, Bando Y. Structural peculiarities of in situ deformation of a multi-walled BN nanotube inside a high-resolution analytical transmission electron microscope. *Acta Materialia* 2007;55(4):1293-1298.
15. Golberg D, Mitome M, Kurashima K, Zhi CY, Tang CC, Bando Y, Lourie O. In situ electrical probing and bias-mediated manipulation of dielectric nanotubes in a high-resolution transmission electron microscope. *Applied Physics Letters* 2006;88(12):123101.
16. Masa Ishigami SA, and A. Zettl Properties of Boron Nitride Nanotubes. *AIP Conference Proceeding* 2003;94:4.
17. Lee CH, Wang J, Kayatsha VK, Huang JY, Yap YK. Effective growth of boron nitride nanotubes by thermal chemical vapor deposition. *Nanotechnology* 2008;19(45):455605.
18. Wu X, Yang JL, Zeng XC. Adsorption of hydrogen molecules on the platinum-doped boron nitride nanotubes. *The Journal of Chemical Physics* 2006;125(4):044704.
19. Oku T, Suganuma K. High-resolution electron microscopy and structural optimization of C₃₆, B₃₆N₃₆ and Fe@B₃₆N₃₆ clusters. *Diamond and Related Materials*;10(3-7):1205-1209.
20. Alem N, Erni R, Kisielowski C, Rossell MD, Gannett W, Zettl A. Atomically thin hexagonal boron nitride probed by ultrahigh-resolution transmission electron microscopy. *Physical Review B* 2009;80(15):155425.
21. Nasreen G. Chopra RJL, K. Cherrey, Vincent H. Crespi, Marvin L. Cohen, Steven G. Louie and A. Zettl. *Boron Nitride Nanotubes. science* 1996;269 (5226):2.
22. Golberg D, Bando Y, Kurashima K, Sato T. Synthesis and characterization of ropes made of BN multiwalled nanotubes. *Scripta Materialia* 2001;44(8-9):1561-1565.
23. Han W, Bando Y, Kurashima K, Sato T. Synthesis of boron nitride nanotubes from carbon nanotubes by a substitution reaction. *Applied Physics Letters* 1998;73(21):3085-3087.
24. Lee RS, Gavillet J, Chapelle MLdl, Loiseau A, Cochon JL, Pigache D, Thibault J, Willaime F. Catalyst-free synthesis of boron nitride single-wall nanotubes with a preferred zig-zag configuration. *Physical Review B* 2001;64(12):121405.
25. Zhu, Bando Y, Yin L, Golberg D. Field Nanoemitters: Ultrathin BN Nanosheets Protruding from Si₃N₄ Nanowires. *Nano Letters* 2006;6(12):2982-2986.

26. Nigam S, Majumder C. CO Oxidation by BN–Fullerene Cage: Effect of Impurity on the Chemical Reactivity. *ACS Nano* 2008;2(7):1422-1428.
27. Guan L, Suenaga K, Okubo S, Okazaki T, Iijima S. Metallic Wires of Lanthanum Atoms Inside Carbon Nanotubes. *Journal of the American Chemical Society* 2008;130(7):2162-2163.
28. Golberg D, Costa PMFJ, Lourie O, Mitome M, Bai X, Kurashima K, Zhi C, Tang C, Bando Y. Direct Force Measurements and Kinking under Elastic Deformation of Individual Multiwalled Boron Nitride Nanotubes. *Nano Letters* 2007;7(7):2146-2151.
29. Blase X, Rubio A, Louie SG, Cohen ML. Stability and Band Gap Constancy of Boron Nitride Nanotubes. *EPL (Europhysics Letters)* 1994;28(5):335.
30. Tang C, Bando Y, Liu C, Fan S, Zhang J, Ding X, Golberg D. Thermal Conductivity of Nanostructured Boron Nitride Materials. *The Journal of Physical Chemistry B* 2006;110(21):10354-10357.
31. Tian B, Zheng X, Kempa TJ, Fang Y, Yu N, Yu G, Huang J, Lieber CM. Coaxial silicon nanowires as solar cells and nanoelectronic power sources. *Nature* 2007;449(7164):885-889.
32. Chang L, Yang-kyu C, Ha D, Ranade P, Shiyong X, Bokor J, Chenming H, King TJ. Extremely scaled silicon nano-CMOS devices. *Proceedings of the IEEE* 2003;91(11):1860-1873.
33. Hochbaum AI, Chen R, Delgado RD, Liang W, Garnett EC, Najarian M, Majumdar A, Yang P. Enhanced thermoelectric performance of rough silicon nanowires. *Nature* 2008;451(7175):163-167.
34. Hall JJ. Electronic Effects in the Elastic Constants of n-Type Silicon. *Physical Review* 1967;161(3):756-761.
35. Serway RA. *Principles of Physics* ed) n, editor. Fort Worth, Texas: London: Saunders College 1998.
36. Volz SG, Chen G. Molecular dynamics simulation of thermal conductivity of silicon nanowires. *Applied Physics Letters* 1999;75(14):2056-2058.
37. Tabib-Azar M, Nassirou M, Wang R, Sharma S, Kamins TI, Islam MS, Williams RS. Mechanical properties of self-welded silicon nanobridges. *Applied Physics Letters* 2005;87(11):113102.
38. He R, Yang P. Giant piezoresistance effect in silicon nanowires. *Nat Nano* 2006;1(1):42-46.

39. Li D, Wu Y, Kim P, Shi L, Yang P, Majumdar A. Thermal conductivity of individual silicon nanowires. *Applied Physics Letters* 2003;83(14):2934-2936.
40. Boukamp BA, Lesh GC, Huggins RA. All-Solid Lithium Electrodes with Mixed-Conductor Matrix. *Journal of The Electrochemical Society* 1981;128(4):725-729.
41. Suryavanshi AP, Yu M-F, Wen J, Tang C, Bando Y. Elastic modulus and resonance behavior of boron nitride nanotubes. *Applied Physics Letters* 2004;84(14):2527-2529.
42. Kim Y-H, Chang KJ, Louie SG. Electronic structure of radially deformed BN and BC₃ nanotubes. *Physical Review B* 2001;63(20):205408.
43. Bai X, Golberg D, Bando Y, Zhi C, Tang C, Mitome M, Kurashima K. Deformation-Driven Electrical Transport of Individual Boron Nitride Nanotubes. *Nano Letters* 2007;7(3):632-637.
44. Bonard J-M, Croci M, Klinke C, Kurt R, Noury O, Weiss N. Carbon nanotube films as electron field emitters. *Carbon* 2002;40(10):1715-1728.
45. Cumings J, Zettl A. Field emission and current-voltage properties of boron nitride nanotubes. *Solid State Communications* 2004;129(10):661-664.
46. Pandey A, Prasad A, Moscatello JP, Yap YK. Stable Electron Field Emission from PMMA–CNT Matrices. *ACS Nano* 2010;4(11):6760-6766.
47. Baggetto L, Niessen RAH, Roozeboom F, Notten PHL. High Energy Density All-Solid-State Batteries: A Challenging Concept Towards 3D Integration. *Advanced Functional Materials* 2008;18(7):1057-1066.
48. Chan CK, Peng H, Liu G, McIlwrath K, Zhang XF, Huggins RA, Cui Y. High-performance lithium battery anodes using silicon nanowires. *Nat Nano* 2008;3(1):31-35.
49. Rosso M, Brissot C, Teyssot A, Dollé M, Sannier L, Tarascon J-M, Bouchet R, Lascaud S. Dendrite short-circuit and fuse effect on Li/polymer/Li cells. *Electrochimica Acta* 2006;51(25):5334-5340.
50. Tobishima S-i, Takei K, Sakurai Y, Yamaki J-i. Lithium ion cell safety. *Journal of Power Sources* 2000;90(2):188-195.
51. Golberg D, Bando Y. Unique morphologies of boron nitride nanotubes. *Applied Physics Letters* 2001;79(3):415-417.
52. Chen Y, Chadderton LT, Gerald JF, Williams JS. A solid-state process for formation of boron nitride nanotubes. *Applied Physics Letters* 1999;74(20):2960-2962.

53. Golberg D, Bando Y, Tang CC, Zhi CY. Boron Nitride Nanotubes. *Advanced Materials* 2007;19(18):2413-2432.
54. Loiseau A, Willaime F, Demoncy N, Hug G, Pascard H. Boron Nitride Nanotubes with Reduced Numbers of Layers Synthesized by Arc Discharge. *Physical Review Letters* 1996;76(25):4737-4740.
55. Zhou GW, Zhang Z, Bai ZG, Yu DP. Catalyst effects on formation of boron nitride nano-tubules synthesized by laser ablation. *Solid State Communications* 1999;109(8):555-559.
56. Golberg D, Bando Y, Han W, Kurashima K, Sato T. Single-walled B-doped carbon, B/N-doped carbon and BN nanotubes synthesized from single-walled carbon nanotubes through a substitution reaction. *Chemical Physics Letters* 1999;308(3-4):337-342.
57. Moscatello JP, Wang J, Ulmen B, Mensah SL, Xie M, Wu S, Pandey A, Lee CH, Prasad A, Kayastha VK and others. ChemInform Abstract: Controlled Growth of Carbon, Boron Nitride, and Zinc Oxide Nanotubes. *ChemInform* 2010;41(23):no-no.
58. Shan B, Lakatos GW, Peng S, Cho K. First-principles study of band-gap change in deformed nanotubes. *Applied Physics Letters* 2005;87(17):173109.
59. Demczyk BG, Cumings J, Zettl A, Ritchie RO. Structure of boron nitride nanotubules. *Applied Physics Letters* 2001;78(18):2772-2774.
60. Zheng F, Zhou G, Hao S, Duan W. Structural characterizations and electronic properties of boron nitride nanotube crystalline bundles. *The Journal of Chemical Physics* 2005;123(12):124716.
61. Blase X, De Vita A, Charlier JC, Car R. Frustration Effects and Microscopic Growth Mechanisms for BN Nanotubes. *Physical Review Letters* 1998;80(8):1666-1669.
62. Kuzumaki T, Hayashi T, Ichinose H, Miyazawa K, Ito K, Ishida Y. In-situ observed deformation of carbon nanotubes. *Philosophical Magazine A* 1998;77(6):1461-1469.
63. Iijima S, Brabec C, Maiti A, Bernholc J. Structural flexibility of carbon nanotubes. *The Journal of Chemical Physics* 1996;104(5):2089-2092.
64. Asaka K, Kato R, Miyazawa Ki, Kizuka T. Buckling of C₆₀ whiskers. *Applied Physics Letters* 2006;89(7):071912.
65. Stone AJ, Wales DJ. Theoretical studies of icosahedral C₆₀ and some related species. *Chemical Physics Letters* 1986;128(5-6):501-503.

66. Hernández E, Goze C, Bernier P, Rubio A. Elastic Properties of C and B_xC_yN_z Composite Nanotubes. *Physical Review Letters* 1998;80(20):4502-4505.
67. Song J, Huang Y, Jiang H, Hwang KC, Yu MF. Deformation and bifurcation analysis of boron-nitride nanotubes. *International Journal of Mechanical Sciences* 2006;48(11):1197-1207.
68. Peng Z, Yonggang H, Geubelle P, Kehchih H. On the continuum modeling of carbon nanotubes. *Acta Mechanica Sinica* 2002;18(5):528-536.
69. Enyashin A, Ivanovskii A. Deformation mechanisms for carbon and boron nitride nanotubes. *Inorganic Materials* 2006;42(12):1336-1341.
70. Peng B, Locascio M, Zapol P, Li S, Mielke SL, Schatz GC, Espinosa HD. Measurements of near-ultimate strength for multiwalled carbon nanotubes and irradiation-induced crosslinking improvements. *Nat Nano* 2008;3(10):626-631.
71. Ghassemi HM, Yassar RS. On the Mechanical Behavior of Boron Nitride Nanotubes. *Applied Mechanics Reviews* 2010;63(2):020804.
72. Ghassemi H, Lee C, Yap Y, Yassar R. In situ TEM monitoring of thermal decomposition in individual boron nitride nanotubes. *JOM Journal of the Minerals, Metals and Materials Society* 2010;62(4):69-73.
73. Seiji Akita HN, Takayoshi Kishida and Yoshikazu Nakayama. Influence of Force Acting on Side Face of Carbon Nanotube in Atomic Force Microscopy
The Japan Society of Applied Physics 2000;39:4.
74. Yu M-F, Lourie O, Dyer MJ, Moloni K, Kelly TF, Ruoff RS. Strength and Breaking Mechanism of Multiwalled Carbon Nanotubes Under Tensile Load. *science* 2000;287(5453):637-640.
75. Espinosa HD, Yong Z, Moldovan N. Design and Operation of a MEMS-Based Material Testing System for Nanomechanical Characterization. *Microelectromechanical Systems, Journal of* 2007;16(5):1219-1231.
76. Ding W, Calabri L, Kohlhaas K, Chen X, Dikin D, Ruoff R. Modulus, Fracture Strength, and Brittle vs. Plastic Response of the Outer Shell of Arc-grown Multi-walled Carbon Nanotubes. *Experimental Mechanics* 2007;47(1):25-36.
77. Xiao Y, Yan XH, Cao JX, Ding JW, Mao YL, Xiang J. Specific heat and quantized thermal conductance of single-walled boron nitride nanotubes. *Physical Review B* 2004;69(20):205415.

78. Chico L, Crespi VH, Benedict LX, Louie SG, Cohen ML. Pure Carbon Nanoscale Devices: Nanotube Heterojunctions. *Physical Review Letters* 1996;76(6):971-974.
79. Collins PG, Bando H, Zettl A. Nanoscale electronic devices on carbon nanotubes. *Nanotechnology* 1998;9(3):153.
80. Chen Z-G, Zou J, Liu G, Li F, Cheng H-M, Sekiguchi T, Gu M, Yao X-D, Wang L-Z, Lu GQ. Long wavelength emissions of periodic yard-glass shaped boron nitride nanotubes. *Applied Physics Letters* 2009;94(2):023105.
81. Hu N, Karube Y, Yan C, Masuda Z, Fukunaga H. Tunneling effect in a polymer/carbon nanotube nanocomposite strain sensor. *Acta Materialia* 2008;56(13):2929-2936.
82. Yakobson BI, Brabec CJ, Bernholc J. Nanomechanics of Carbon Tubes: Instabilities beyond Linear Response. *Physical Review Letters* 1996;76(14):2511-2514.
83. Falvo MR, Clary GJ, Taylor RM, Chi V, Brooks FP, Washburn S, Superfine R. Bending and buckling of carbon nanotubes under large strain. *Nature* 1997;389(6651):582-584.
84. Poncharal P, Wang ZL, Ugarte D, de Heer WA. Electrostatic Deflections and Electromechanical Resonances of Carbon Nanotubes. *science* 1999;283(5407):1513-1516.
85. Bower C, Rosen R, Jin L, Han J, Zhou O. Deformation of carbon nanotubes in nanotube--polymer composites. *Applied Physics Letters* 1999;74(22):3317-3319.
86. Lourie O, Cox DM, Wagner HD. Buckling and Collapse of Embedded Carbon Nanotubes. *Physical Review Letters* 1998;81(8):1638-1641.
87. Ghassemi HM, Lee CH, Yap YK, Yassar RS. Real-time fracture detection of individual boron nitride nanotubes in severe cyclic deformation processes. *Journal of Applied Physics* 2010;108(2):024314.
88. Menon M, Srivastava D. Structure of boron nitride nanotubes: tube closing versus chirality. *Chemical Physics Letters* 1999;307(5-6):407-412.
89. Seifert G, Fowler PW, Mitchell D, Porezag D, Frauenheim T. Boron-nitrogen analogues of the fullerenes: electronic and structural properties. *Chemical Physics Letters* 1997;268(5-6):352-358.
90. Cumings J, Zettl A. Low-Friction Nanoscale Linear Bearing Realized from Multiwall Carbon Nanotubes. *science* 2000;289(5479):602-604.

91. Ju GT, Kyriakides S. Bifurcation and localization instabilities in cylindrical shells under bending—II. Predictions. *International Journal of Solids and Structures* 1992;29(9):1143-1171.
92. Landau LDL, E. M. . *Theory of elasticity*. Pergamon: Oxford; 1986.
93. Stephen P. Timoshenko JMG. *Theory of Elastic Stability*. McGraw-Hill Book Company, Inc.; 2009.
94. Cardinale GF, Howitt DG, McCarty KF, Medlin DL, Mirkarimi PB, Moody NR. Analysis of residual stress in cubic boron nitride thin films using micromachined cantilever beams. *Diamond and Related Materials* 1996;5(11):1295-1302.
95. Pantano A, M. Parks D, Boyce MC. Mechanics of deformation of single- and multi-wall carbon nanotubes. *Journal of the Mechanics and Physics of Solids* 2004;52(4):789-821.
96. Golberg D, Dorozhkin PS, Bando Y, Dong ZC, Tang CC, Uemura Y, Grobert N, Reyes-Reyes M, Terrones H, Terrones M. Structure, transport and field-emission properties of compound nanotubes: $\text{CN}_{x-y}\text{B}_y\text{N}_{1-y}$ vs. $\text{BNC}_{x-y}\text{N}_y$ ($x+y \approx 1$). *Applied Physics A: Materials Science & Processing* 2003;76(4):499-507.
97. Golberg D, Costa P, Mitome M, Bando Y. Nanotubes in a gradient electric field as revealed by STM TEM technique. *Nano Research* 2008;1(2):166-175.
98. Wang J, Kayastha VK, Yap YK, Fan Z, Lu JG, Pan Z, Ivanov IN, Poretzky AA, Geohegan DB. Low Temperature Growth of Boron Nitride Nanotubes on Substrates. *Nano Letters* 2005;5(12):2528-2532.
99. Jaffrennou P, Barjon J, Lauret JS, Maguer A, Golberg D, Attal-Trétout B, Ducastelle F, Loiseau A. Optical properties of multiwall boron nitride nanotubes. *physica status solidi (b)* 2007;244(11):4147-4151.
100. Schottky W. Halbleitertheorie der Sperrschicht. *Naturwissenschaften* 1938;26(52):843-843.
101. Padovani FA, Stratton R. Field and thermionic-field emission in Schottky barriers. *Solid-State Electronics* 1966;9(7):695-707.
102. Dürkop T, Getty SA, Cobas E, Fuhrer MS. Extraordinary Mobility in Semiconducting Carbon Nanotubes. *Nano Letters* 2003;4(1):35-39.
103. Bolotin KI, Sikes KJ, Jiang Z, Klima M, Fudenberg G, Hone J, Kim P, Stormer HL. Ultrahigh electron mobility in suspended graphene. *Solid State Communications* 2008;146(9-10):351-355.

104. Asthana A, Momeni K, Prasad A, Yap YK, Yassar RS. In situ probing of electromechanical properties of an individual ZnO nanobelt. *Applied Physics Letters* 2009;95(17):172106.
105. Zhang Z, Yao K, Liu Y, Jin C, Liang X, Chen Q, Peng LM. Quantitative Analysis of Current–Voltage Characteristics of Semiconducting Nanowires: Decoupling of Contact Effects. *Advanced Functional Materials* 2007;17(14):2478-2489.
106. Wang ZL, Gao RP, Heer WAd, Poncharal P. In situ imaging of field emission from individual carbon nanotubes and their structural damage. *Applied Physics Letters* 2002;80(5):856-858.
107. Fowler RH, Nordheim L. Electron Emission in Intense Electric Fields. *Proceedings of the Royal Society of London. Series A* 1928;119(781):173-181.
108. Bonard JM, Salvétat JP, Stöckli T, Forró L, Châtelain A. Field emission from carbon nanotubes: perspectives for applications and clues to the emission mechanism. *Applied Physics A: Materials Science & Processing* 1999;69(3):245-254.
109. Collins PG, Zettl A. Unique characteristics of cold cathode carbon-nanotube-matrix field emitters. *Physical Review B* 1997;55(15):9391-9399.
110. Chen H, Zhang H, Fu L, Chen Y, Williams JS, Yu C, Yu D. Nano Au-decorated boron nitride nanotubes: Conductance modification and field-emission enhancement. *Applied Physics Letters* 2008;92(24):243105.
111. Ducastelle F, Blase X, Bonard JM, Charlier JC, Petit P. Electronic Structure Understanding Carbon Nanotubes. In: Loiseau A, Launois P, Petit P, Roche S, Salvétat J-P, editors. Volume 677, *Lecture Notes in Physics*: Springer Berlin / Heidelberg; 2006. p 199-276.
112. Jencic I, Bench MW, Robertson IM, Kirk MA. Electron-beam-induced crystallization of isolated amorphous regions in Si, Ge, GaP, and GaAs. *Journal of Applied Physics* 1995;78(2):974-982.
113. Golberg D, Bando Y, Huang Y, Terao T, Mitome M, Tang C, Zhi C. Boron Nitride Nanotubes and Nanosheets. *ACS Nano* 2010;4(6):2979-2993.
114. Kwon Y-K, Tománek D, Iijima S. “Bucky Shuttle” Memory Device: Synthetic Approach and Molecular Dynamics Simulations. *Physical Review Letters* 1999;82(7):1470-1473.
115. Collins PG, Zettl A, Bando H, Thess A, Smalley RE. Nanotube Nanodevice. *science* 1997;278(5335):100-102.

116. Huang JY, Chen S, Ren ZF, Chen G, Dresselhaus MS. Real-Time Observation of Tubule Formation from Amorphous Carbon Nanowires under High-Bias Joule Heating. *Nano Letters* 2006;6(8):1699-1705.
117. Xu Z, Golberg D, Bando Y. In Situ TEM-STM Recorded Kinetics of Boron Nitride Nanotube Failure under Current Flow. *Nano Letters* 2009;9(6):2251-2254.
118. Huang JY, Ding F, Yakobson BI. Dislocation Dynamics in Multiwalled Carbon Nanotubes at High Temperatures. *Physical Review Letters* 2008;100(3):035503.
119. Huang JY, Ding F, Jiao K, Yakobson BI. Real Time Microscopy, Kinetics, and Mechanism of Giant Fullerene Evaporation. *Physical Review Letters* 2007;99(17):175503.
120. Wang J, Lee CH, Bando Y, Golberg D, Yap YK. Multiwalled Boron Nitride Nanotubes: Growth, Properties, and Applications
B-C-N Nanotubes and Related Nanostructures. Volume 6, Lecture Notes in Nanoscale Science and Technology: Springer New York; 2009. p 23-44.
121. Durkan C, Schneider MA, Welland ME. Analysis of failure mechanisms in electrically stressed Au nanowires. *Journal of Applied Physics* 1999;86(3):1280-1286.
122. Armand M, Tarascon JM. Building better batteries. *Nature* 2008;451(7179):652-657.
123. Green M, Fielder E, Scrosati B, Wachtler M, Moreno JS. Structured Silicon Anodes for Lithium Battery Applications. *Electrochemical and Solid-State Letters* 2003;6(5):A75-A79.
124. Kasavajjula U, Wang C, Appleby AJ. Nano- and bulk-silicon-based insertion anodes for lithium-ion secondary cells. *Journal of Power Sources* 2007;163(2):1003-1039.
125. Yang J, Winter M, Besenhard JO. Small particle size multiphase Li-alloy anodes for lithium-ion batteries. *Solid State Ionics* 1996;90(1-4):281-287.
126. Föll H, Hartz H, Ossei-Wusu E, Carstensen J, Riemenschneider O. Si nanowire arrays as anodes in Li ion batteries. *physica status solidi (RRL) – Rapid Research Letters* 2010;4(1-2):4-6.
127. Maranchi JP, Hepp AF, Evans AG, Nuhfer NT, Kumta PN. Interfacial Properties of the a-Si/Cu:Active--Inactive Thin-Film Anode System for Lithium-Ion Batteries. *Journal of The Electrochemical Society* 2006;153(6):A1246-A1253.

128. Huggins R, Nix W. Decrepitation model for capacity loss during cycling of alloys in rechargeable electrochemical systems. *Ionics* 2000;6(1):57-63.
129. C.M. Wang WX, J. Liu, D.W. Choi, B. Arey, L.V. Saraf, J.G. Zhang, Z.G. Yang, S. Thevuthasan, D.R. Baer and N. Salmon . In situ transmission electron microscopy and spectroscopy studies of interfaces in Li ion batteries: Challenges and opportunities. *Journal of Materials Research* 2010;25:7.
130. Brazier A, Dupont L, Dantras-Laffont L, Kuwata N, Kawamura J, Tarascon JM. First Cross-Section Observation of an All Solid-State Lithium-Ion “Nanobattery” by Transmission Electron Microscopy. *Chemistry of Materials* 2008;20(6):2352-2359.
131. Huang JY, Zhong L, Wang CM, Sullivan JP, Xu W, Zhang LQ, Mao SX, Hudak NS, Liu XH, Subramanian A and others. In Situ Observation of the Electrochemical Lithiation of a Single SnO₂ Nanowire Electrode. *science* 2010;330(6010):1515-1520.
132. Beaulieu LY, Eberman KW, Turner RL, Krause LJ, Dahn JR. Colossal Reversible Volume Changes in Lithium Alloys. *Electrochemical and Solid-State Letters* 2001;4(9):A137-A140.
133. Yin J, Wada M, Yamamoto K, Kitano Y, Tanase S, Sakai T. Micrometer-Scale Amorphous Si Thin-Film Electrodes Fabricated by Electron-Beam Deposition for Li-Ion Batteries. *Journal of The Electrochemical Society* 2006;153(3):A472-A477.
134. Maranchi JP, Hepp AF, Kumta PN. High Capacity, Reversible Silicon Thin-Film Anodes for Lithium-Ion Batteries. *Electrochemical and Solid-State Letters* 2003;6(9):A198-A201.
135. Liu XH, Zheng H, Zhong L, Huang S, Karki K, Zhang LQ, Liu Y, Kushima A, Liang WT, Wang JW and others. Anisotropic Swelling and Fracture of Silicon Nanowires during Lithiation. *Nano Letters* 2011;11(8):3312-3318.
136. Liu XH, Zhang LQ, Zhong L, Liu Y, Zheng H, Wang JW, Cho J-H, Dayeh SA, Picraux ST, Sullivan JP and others. Ultrafast Electrochemical Lithiation of Individual Si Nanowire Anodes. *Nano Letters* 2011;11(6):2251-2258.
137. He Y, Zhang Z, Hoffmann C, Zhao Y. Embedding Ag Nanoparticles into MgF₂ Nanorod Arrays. *Advanced Functional Materials* 2008;18(11):1676-1684.
138. Pierre-Gilles de Gennes FB-W, David Quere. *Capillarity and Wetting Phenomena: Drops, Bubbles, Pearls, Waves.* english, editor: springer; 2003. 306 p.

139. Hofmann S, Csányi G, Ferrari AC, Payne MC, Robertson J. Surface Diffusion: The Low Activation Energy Path for Nanotube Growth. *Physical Review Letters* 2005;95(3):036101.
140. Tanemura M, Iwata K, Takahashi K, Fujimoto Y, Okuyama F, Sugie H, Filip V. Growth of aligned carbon nanotubes by plasma-enhanced chemical vapor deposition: Optimization of growth parameters. *Journal of Applied Physics* 2001;90(3):1529-1533.
141. Gao B, Sinha S, Fleming L, Zhou O. Alloy Formation in Nanostructured Silicon. *Advanced Materials* 2001;13(11):816-819.
142. Zhou Y-N, Li W-J, Chen H-J, Liu C, Zhang L, Fu Z. Nanostructured NiSi thin films as a new anode material for lithium ion batteries. *Electrochemistry Communications* 2011;13(6):546-549.
143. Okamoto H. The Li-Si (Lithium-Silicon) system. *Journal of Phase Equilibria* 1990;11(3):306-312.
144. Obrovac MN, Christensen L. Structural Changes in Silicon Anodes during Lithium Insertion/Extraction. *Electrochemical and Solid-State Letters* 2004;7(5):A93-A96.
145. Hatchard TD, Dahn JR. In Situ XRD and Electrochemical Study of the Reaction of Lithium with Amorphous Silicon. *Journal of The Electrochemical Society* 2004;151(6):A838-A842.
146. Anani A, Crouch-Baker S, Huggins RA. Kinetic and Thermodynamic Parameters of Several Binary Lithium Alloy Negative Electrode Materials at Ambient Temperature. *Journal of The Electrochemical Society* 1987;134(12):3098-3102.
147. Wilkening M, Bork D, Indris S, Heitjans P. Diffusion in amorphous LiNbO₃ studied by ⁷Li NMR - comparison with the nano- and microcrystalline material. *Physical Chemistry Chemical Physics* 2002;4(14):3246-3251.
148. Kang K, Lee H-S, Han D-W, Kim G-S, Lee D, Lee G, Kang Y-M, Jo M-H. Maximum Li storage in Si nanowires for the high capacity three-dimensional Li-ion battery. *Applied Physics Letters* 2010;96(5):053110.
149. Dimov N, Kugino S, Yoshio M. Mixed silicon-graphite composites as anode material for lithium ion batteries: Influence of preparation conditions on the properties of the material. *Journal of Power Sources* 2004;136(1):108-114.
150. Aifantis KE, Dempsey JP. Stable crack growth in nanostructured Li-batteries. *Journal of Power Sources* 2005;143(1-2):203-211.

151. Orsini F, Du Pasquier A, Beaudoin B, Tarascon JM, Trentin M, Langenhuizen N, De Beer E, Notten P. In situ Scanning Electron Microscopy (SEM) observation of interfaces within plastic lithium batteries. *Journal of Power Sources* 1998;76(1):19-29.
152. Tobishima S, Sakurai Y, Yamaki J. Safety characteristics of rechargeable lithium metal cells. *Journal of Power Sources* 1997;68(2):455-458.
153. Bhattacharyya R, Key B, Chen H, Best AS, Hollenkamp AF, Grey CP. In situ NMR observation of the formation of metallic lithium microstructures in lithium batteries. *Nat Mater* 2010;9(6):504-510.
154. M.B. Armand JMCaMJD. 1978; St. Andrews. p Paper 6.5,.
155. Croce F, Appetecchi GB, Persi L, Scrosati B. Nanocomposite polymer electrolytes for lithium batteries. *Nature* 1998;394(6692):456-458.
156. Xu K. Nonaqueous Liquid Electrolytes for Lithium-Based Rechargeable Batteries. *Chemical Reviews* 2004;104(10):4303-4418.
157. Wilkes JS, Zaworotko MJ. Air and water stable 1-ethyl-3-methylimidazolium based ionic liquids. *Journal of the Chemical Society, Chemical Communications* 1992(13):965-967.
158. Ionic Liquids. American Chemical Society; 2002. 492 p.
159. Kuwabata S, Kongkanand A, Oyamatsu D, Torimoto T. Observation of Ionic Liquid by Scanning Electron Microscope. *Chemistry Letters* 2006;35(6):600-601.
160. Armand M, Endres F, MacFarlane DR, Ohno H, Scrosati B. Ionic-liquid materials for the electrochemical challenges of the future. *Nat Mater* 2009;8(8):621-629.
161. Howlett PC, MacFarlane DR, Hollenkamp AF. High Lithium Metal Cycling Efficiency in a Room-Temperature Ionic Liquid. *Electrochemical and Solid-State Letters* 2004;7(5):A97-A101.
162. Wang Y. Disordering and Reordering of Ionic Liquids under an External Electric Field. *The Journal of Physical Chemistry B* 2009;113(32):11058-11060.
163. Liu XH, Zhong L, Zhang LQ, Kushima A, Mao SX, Li J, Ye ZZ, Sullivan JP, Huang JY. Lithium fiber growth on the anode in a nanowire lithium ion battery during charging. *Applied Physics Letters* 2011;98(18):183107.
164. Yamaki J-i, Tobishima S-i, Hayashi K, Keiichi S, Nemoto Y, Arakawa M. A consideration of the morphology of electrochemically deposited lithium in an organic electrolyte. *Journal of Power Sources* 1998;74(2):219-227.

165. Yoshimatsu I, Hirai T, Yamaki J-i. Lithium Electrode Morphology during Cycling in Lithium Cells. *Journal of The Electrochemical Society* 1988;135(10):2422-2427.
166. Aurbach D, Zinigrad E, Cohen Y, Teller H. A short review of failure mechanisms of lithium metal and lithiated graphite anodes in liquid electrolyte solutions. *Solid State Ionics* 2002;148(3-4):405-416.
167. Bourlon B, Glatli DC, Miko C, Forró L, Bachtold A. Carbon Nanotube Based Bearing for Rotational Motions. *Nano Letters* 2004;4(4):709-712.
168. Zhou Z, Zhao J, Chen Z, Gao X, Lu JP, Schleyer PvR, Yang C-K. True Nanocable Assemblies with Insulating BN Nanotube Sheaths and Conducting Cu Nanowire Cores. *The Journal of Physical Chemistry B* 2006;110(6):2529-2532.
169. Kong J, Franklin NR, Zhou C, Chapline MG, Peng S, Cho K, Dai H. Nanotube Molecular Wires as Chemical Sensors. *science* 2000;287(5453):622-625.
170. . C. H. Lee VKK, J. Wang, and Y. K. Yap. Introduction to B-C-N materials. *B-C-N Nanotubes and Related Nanostructures. Volume 6: Springer.* p 22.
171. Mazzoni MSC, Nunes RW, Azevedo S, Chacham H. Electronic structure and energetics of $B_xC_yN_z$ layered structures. *Physical Review B* 2006;73(7):073108.
172. Yin L-W, Bando Y, Golberg D, Gloter A, Li M-S, Yuan X, Sekiguchi T. Porous BCN Nanotubular Fibers: Growth and Spatially Resolved Cathodoluminescence. *Journal of the American Chemical Society* 2005;127(47):16354-16355.
173. Yu J, Ahn J, Yoon SF, Zhang Q, Rusli, Gan B, Chew K, Yu MB, Bai XD, Wang EG. Semiconducting boron carbonitride nanostructures: Nanotubes and nanofibers. *Applied Physics Letters* 2000;77(13):1949-1951.
174. Terrones M, Golberg D, Grobert N, Seeger T, Reyes-Reyes M, Mayne M, Kamalakaran R, Dorozhkin P, Dong ZC, Terrones H and others. Production and State-of-the-Art Characterization of Aligned Nanotubes with Homogeneous BC_xN ($1 \leq x \leq 5$) Compositions. *Advanced Materials* 2003;15(22):1899-1903.
175. Zhao J-x, Ding Y-h. Theoretical studies of chemical functionalization of the (8,0) boron nitride nanotube with various metalloporphyrin MP (M= = Fe, Co, Ni, Cu, and Zn) complexes. *Materials Chemistry and Physics* 2009;116(1):21-27.
176. Seif A, Boshra A, Seif M. Lithium-doped (4,4) Boron nitride nanotube: Density functional theory study of N and B nuclear magnetic shielding and electric field

- gradient tensors. *Journal of Molecular Structure: THEOCHEM* 2009;895(1-3):82-85.
177. Kang HS. Theoretical Study of Boron Nitride Nanotubes with Defects in Nitrogen-Rich Synthesis. *The Journal of Physical Chemistry B* 2006;110(10):4621-4628.
 178. Liao L, Liu K, Wang W, Bai X, Wang E, Liu Y, Li J, Liu C. Multiwall Boron Carbonitride/Carbon Nanotube Junction and Its Rectification Behavior. *Journal of the American Chemical Society* 2007;129(31):9562-9563.
 179. Wei X, Wang M-S, Bando Y, Golberg D. Tensile Tests on Individual Multi-Walled Boron Nitride Nanotubes. *Advanced Materials* 2010;22(43):4895-4899.
 180. Huang JY, Chen S, Wang ZQ, Kempa K, Wang YM, Jo SH, Chen G, Dresselhaus MS, Ren ZF. Superplastic carbon nanotubes. *Nature* 2006;439(7074):281-281.
 181. Lu Y, Peng C, Ganesan Y, Huang JY, Lou J. Quantitative in situ TEM tensile testing of an individual nickel nanowire. *Nanotechnology* 2011;22(35):355702.
 182. Wei X, Wang M-S, Bando Y, Golberg D. Post-Synthesis Carbon Doping of Individual Multiwalled Boron Nitride Nanotubes via Electron-Beam Irradiation. *Journal of the American Chemical Society* 2010;132(39):13592-13593.
 183. Ahmad S. The X (X= C, Si and Ge) doped BN nanotube: A computational study. *Superlattices and Microstructures* 2011;50(1):14-20.
 184. Chen H, Chen Y, Liu Y, Zhang H, Li CP, Liu Z, Ringer SP, Williams JS. Rare-earth doped boron nitride nanotubes. *Materials Science and Engineering: B* 2008;146(1-3):189-192.
 185. Chen H, Chen Y, Liu Y. Cathodoluminescence of boron nitride nanotubes doped by ytterbium. *Journal of Alloys and Compounds* 2010;504, Supplement 1(0):S353-S355.
 186. Du Pasquier A, Plitz I, Menocal S, Amatucci G. A comparative study of Li-ion battery, supercapacitor and nonaqueous asymmetric hybrid devices for automotive applications. *Journal of Power Sources* 2003;115(1):171-178.
 187. Westbrook MH. *The Electric Car: Development and Future of Battery, Hybrid and Fuel-cell Cars.* series Ipae, editor: Institution of Electrical Engineers; 2001.
 188. Wang Y, Cao G. Developments in Nanostructured Cathode Materials for High-Performance Lithium-Ion Batteries. *Advanced Materials* 2008;20(12):2251-2269.

189. Kostecki R, McLarnon F. Degradation of $\text{LiNi}_{0.8}\text{Co}_{0.2}\text{O}_2$ Cathode Surfaces in High-Power Lithium-Ion Batteries. *Electrochemical and Solid-State Letters* 2002;5(7):A164-A166.
190. Li C, Zhang HP, Fu LJ, Liu H, Wu YP, Rahm E, Holze R, Wu HQ. Cathode materials modified by surface coating for lithium ion batteries. *Electrochimica Acta* 2006;51(19):3872-3883.
191. Ruffo R, Wessells C, Huggins RA, Cui Y. Electrochemical behavior of LiCoO_2 as aqueous lithium-ion battery electrodes. *Electrochemistry Communications* 2009;11(2):247-249.
192. Kim J, Noh M, Cho J, Kim H, Kim K-B. Controlled Nanoparticle Metal Phosphates (Metal = Al, Fe, Ce, and Sr) Coatings on LiCoO_2 Cathode Materials. *Journal of The Electrochemical Society* 2005;152(6):A1142-A1148.
193. Wang D, Ma X, Wang Y, Wang L, Wang Z, Zheng W, He X, Li J, Peng Q, Li Y. Shape control of CoO and LiCoO_2 nanocrystals. *Nano Research* 2010;3(1):1-7.
194. Jiao F, Shaju KM, Bruce PG. Synthesis of Nanowire and Mesoporous Low-Temperature LiCoO_2 by a Post-Templating Reaction. *Angewandte Chemie International Edition* 2005;44(40):6550-6553.
195. Medlin DL, Friedmann TA, Mirkarimi PB, Mills MJ, McCarty KF. Evidence for rhombohedral boron nitride in cubic boron nitride films grown by ion-assisted deposition. *Physical Review B* 1994;50(11):7884-7887.
196. Sze SM, Coleman Jr DJ, Loya A. Current transport in metal-semiconductor-metal (MSM) structures. *Solid-State Electronics* 1971;14(12):1209-1218.

Appendix-A: BORON NITRIDE PHASES

Boron nitride structures consist of boron and nitrogen atoms. Since a B-N bond possesses the same amount of electron as that of the C-C bond in a carbon structure, they are considered to have covalent structure as well. Various crystallographic phases of BN exist, such as hexagon, wurtzite, rhombohedral and cubic.¹⁹⁵ Schematic of these structure are shown in Figure A. 1.

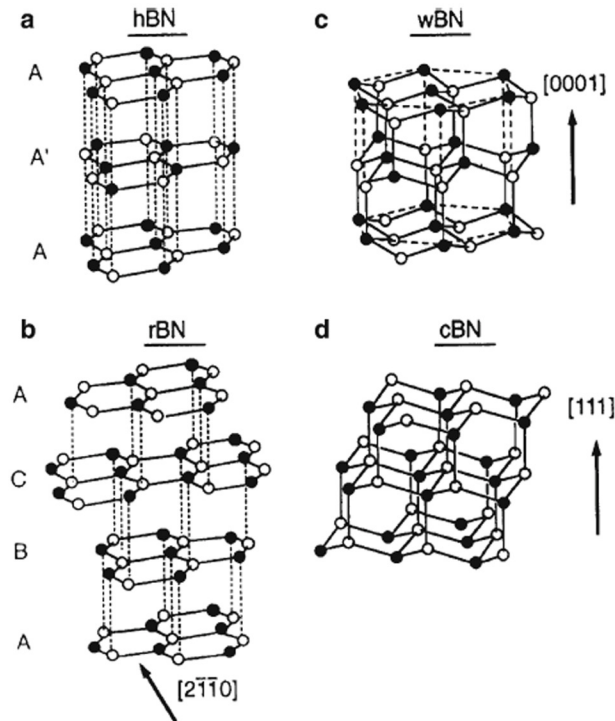


Figure A. 1 Schematics of different phases of BN structures corresponding to (a) hBN, (b) wBN, (c) rBN and (d) cBN.¹⁹⁵ (Reprinted with permission from Phys. Rev. B 50, 7884–7887 (1994) . Copyright 1994, American Physics Socieity Ltd.) DOI: 10.1103/PhysRevB.50.7884

Hexagon and rhombohedral structures BN structures include two sp^2 bonds, however cubic and wurtzite structures possess two sp^3 bonds. At high temperature and pressure, hBN can be converted to cBN in bulk form. BN nanotubes have hBN structure where B atoms in one layer are bonded to N atoms of adjacent layers, also known as $AA'AA'$ stacking sequence.¹⁷⁰

Appendix-B: ON THE RELATIONSHIP BETWEEN TEMPERATURE AND CURRENT DURING JOULE HEATING EXPERIMENTS

Based on the thermionic field-emission model,¹⁹⁶ one can correlate the amount of passing current through the sample to the increase in the temperature during the Joule heating experiment. Therefore, current density is a function of temperature using the equation below:

$$J(V, Q_b) = A^* T^2 \exp\left(-\frac{Q_b}{kT}\right) \exp\left(\frac{qV}{nkT}\right) * \{1 - \exp\left(-\frac{qV}{kT}\right)\} \quad (\text{B-1})$$

where $A^* = 4\pi m^* q k^2 / h^3$ is the Richardson constant of the semiconductor, Q_b is the effective Schottky barrier height, k is the Boltzmann constant, q is the magnitude of the electronic charge, T is the absolute temperature, and n is the ideality factor which is a dimensionless quantity for describing the deviation of the diode from an idea Schottky barrier with $n=1$. Following the above-mentioned calculations, one can plot the changes in the temperature based on the current density as shown in Figure B. 1. These results are in good agreement with the reported results.¹¹⁷

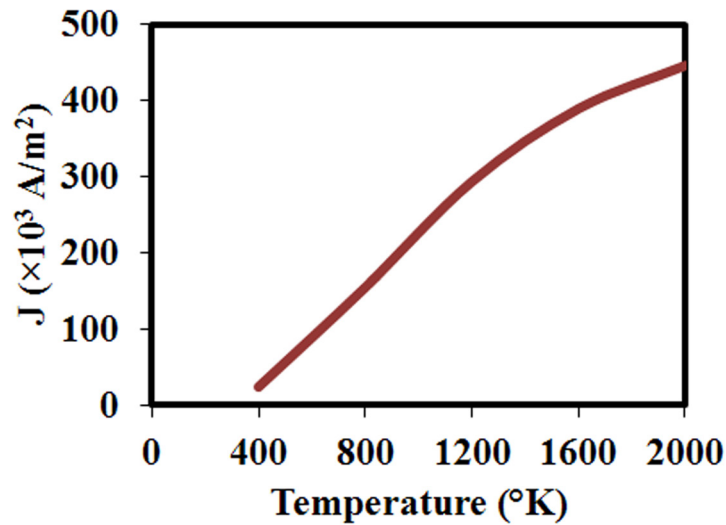


Figure B. 1 Plot of increase in temperature as a function of current density.

Appendix-C: COPYRIGHT PERMISSIONS

LICENSES FOR CHAPTER-3

Dear Mr. Ghassemi:

It is our pleasure to grant you permission to ASME paper “ON THE MECHANICAL BEHAVIOR OF BORON NITRIDE NANOTUBES,” by H. M. Ghassemi and R. S. Yassar, Applied Mechanics Reviews, Vol. 63, Issue 2, March 2010, cited in your letter for inclusion in a Doctoral Thesis entitled IN-SITU ELECTRICAL, MECHANICAL AND ELECTROCHEMICAL CHARACTERIZATIONS OF ONE-DIMENSIONAL NANOSTRUCTURES to be published by Michigan Technological University.

As is customary, we ask that you ensure full acknowledgment of this material, the author(s), source and ASME as original publisher on all printed copies being distributed.

Many thanks for your interest in ASME publications.

Sincerely,

Beth Darchi

Permissions & Copyrights

ASME, 3 Park Avenue

New York, NY 10016

T: 212-591-7700

F: 212-591-7841

E: darchib@asme.org

LICENSES FOR FIGURES 3.2 AND 3.3

Thank you very much for your order.

This is a License Agreement between hessam ghassemi ("You") and Elsevier ("Elsevier"). The license consists of your order details, the terms and conditions provided by Elsevier, and the payment terms and conditions.

Get the printable license.

License Number	2793160620563
License date	Nov 20, 2011
Licensed content publisher	Elsevier
Licensed content publication	Solid State Communications
Licensed content title	Measurement of the elastic modulus of a multi-wall boron nitride nanotube
Licensed content author	Nasreen G. Chopra,A. Zettl
Licensed content date	February 1998
Licensed content volume number	105
Licensed content issue number	5
Number of pages	4
Type of Use	reuse in a thesis/dissertation
Portion	figures/tables/illustrations
Number of figures/tables/illustrations	2
Format	both print and electronic
Are you the author of this Elsevier article?	No
Will you be translating?	No
Order reference number	
Title of your thesis/dissertation	IN-SITU ELECTRICAL, MECHANICAL AND ELECTROCHEMICAL CHARACTERIZATIONS OF ONE-DIMENSIONAL NANOSTRUCTURES
Expected completion date	Jan 2012
Estimated size (number	100

of pages)	
Elsevier VAT number	GB 494 6272 12
Permissions price	0.00 USD
VAT/Local Sales Tax	0.0 USD / 0.0 GBP
Total	0.00 USD

LICENSES FOR FIGURE 3.4

Thank you very much for your order.

This is a License Agreement between hessam ghassemi ("You") and American Institute of Physics ("AIP"). The license consists of your order details, the terms and conditions provided by American Institute of Physics, and the payment terms and conditions.

Get the printable license.

License Number	2793160931391
License date	Nov 20, 2011
Licensed content publisher	American Institute of Physics
Licensed content publication	Applied Physics Letters
Licensed content title	Elastic modulus and resonance behavior of boron nitride nanotubes
Licensed content author	Abhijit P. Suryavanshi, Min-Feng Yu, Jianguo Wen, Chengchun Tang, et al.
Licensed content date	Apr 5, 2004
Volume number	84
Issue number	14
Type of Use	Thesis/Dissertation
Requestor type	Student
Format	Print and electronic
Portion	Figure/Table
Number of figures/tables	1

Title of your thesis / dissertation	IN-SITU ELECTRICAL, MECHANICAL AND ELECTROCHEMICAL CHARACTERIZATIONS OF ONE-DIMENSIONAL NANOSTRUCTURES
Expected completion date	Jan 2012
Estimated size (number of pages)	100
Total	0.00 USD

LICENSES FOR FIGURES 3.5 AND 3.6

Thank you very much for your order.

This is a License Agreement between hessam ghassemi ("You") and Elsevier ("Elsevier"). The license consists of your order details, the terms and conditions provided by Elsevier, and the payment terms and conditions.

Get the printable license.

License Number	2793161236156
License date	Nov 20, 2011
Licensed content publisher	Elsevier
Licensed content publication	Acta Materialia
Licensed content title	Structural peculiarities of in situ deformation of a multi-walled BN nanotube inside a high-resolution analytical transmission electron microscope
Licensed content author	D. Golberg,X.D. Bai,M. Mitome,C.C. Tang,C.Y. Zhi,Y. Bando
Licensed content date	February 2007
Licensed content volume number	55
Licensed content issue number	4
Number of pages	6
Type of Use	reuse in a thesis/dissertation
Portion	figures/tables/illustrations
Number of figures/tables/illustrations	2
Format	both print and electronic

Are you the author of this Elsevier article?	No
Will you be translating?	No
Order reference number	
Title of your thesis/dissertation	IN-SITU ELECTRICAL, MECHANICAL AND ELECTROCHEMICAL CHARACTERIZATIONS OF ONE-DIMENSIONAL NANOSTRUCTURES
Expected completion date	Jan 2012
Estimated size (number of pages)	100
Elsevier VAT number	GB 494 6272 12
Permissions price	0.00 USD
VAT/Local Sales Tax	0.0 USD / 0.0 GBP
Total	0.00 USD

LICENSES FOR FIGURES 3.7 AND 3.8

PERMISSION/LICENSE IS GRANTED FOR YOUR ORDER AT NO CHARGE

This type of permission/license, instead of the standard Terms & Conditions, is sent to you because no fee is being charged for your order. Please note the following:

- Permission is granted for your request in both print and electronic formats.
- If figures and/or tables were requested, they may be adapted or used in part.
- Please print this page for your records and send a copy of it to your publisher/graduate school.
- Appropriate credit for the requested material should be given as follows: "Reprinted (adapted) with permission from (COMPLETE REFERENCE CITATION). Copyright (YEAR) American Chemical Society." Insert appropriate information in place of the capitalized words.
- One-time permission is granted only for the use specified in your request. No additional uses are granted (such as derivative works or other editions). For any

other uses, please submit a new request.

LICENSES FOR FIGURE 3.9

Thank you very much for your order.

This is a License Agreement between hessam ghassemi ("You") and Elsevier ("Elsevier"). The license consists of your order details, the terms and conditions provided by Elsevier, and the payment terms and conditions.

Get the printable license.

License Number	2793170306703
License date	Nov 20, 2011
Licensed content publisher	Elsevier
Licensed content publication	Scripta Materialia
Licensed content title	Stone–Wales transformation in boron nitride nanotubes
Licensed content author	J. Song,H. Jiang,J. Wu,Y. Huang,K.-C. Hwang
Licensed content date	October 2007
Licensed content volume number	57
Licensed content issue number	7
Number of pages	4
Type of Use	reuse in a thesis/dissertation
Portion	figures/tables/illustrations
Number of figures/tables/illustrations	1
Format	both print and electronic
Are you the author of this Elsevier article?	No
Will you be translating?	No
Order reference number	
Title of your thesis/dissertation	IN-SITU ELECTRICAL, MECHANICAL AND ELECTROCHEMICAL CHARACTERIZATIONS OF ONE-DIMENSIONAL NANOSTRUCTURES
Expected completion date	Jan 2012
Estimated size (number of pages)	100

Elsevier VAT number	GB 494 6272 12
Permissions price	0.00 USD
VAT/Local Sales Tax	0.0 USD / 0.0 GBP
Total	0.00 USD

LICENSES FOR CHAPTER-4

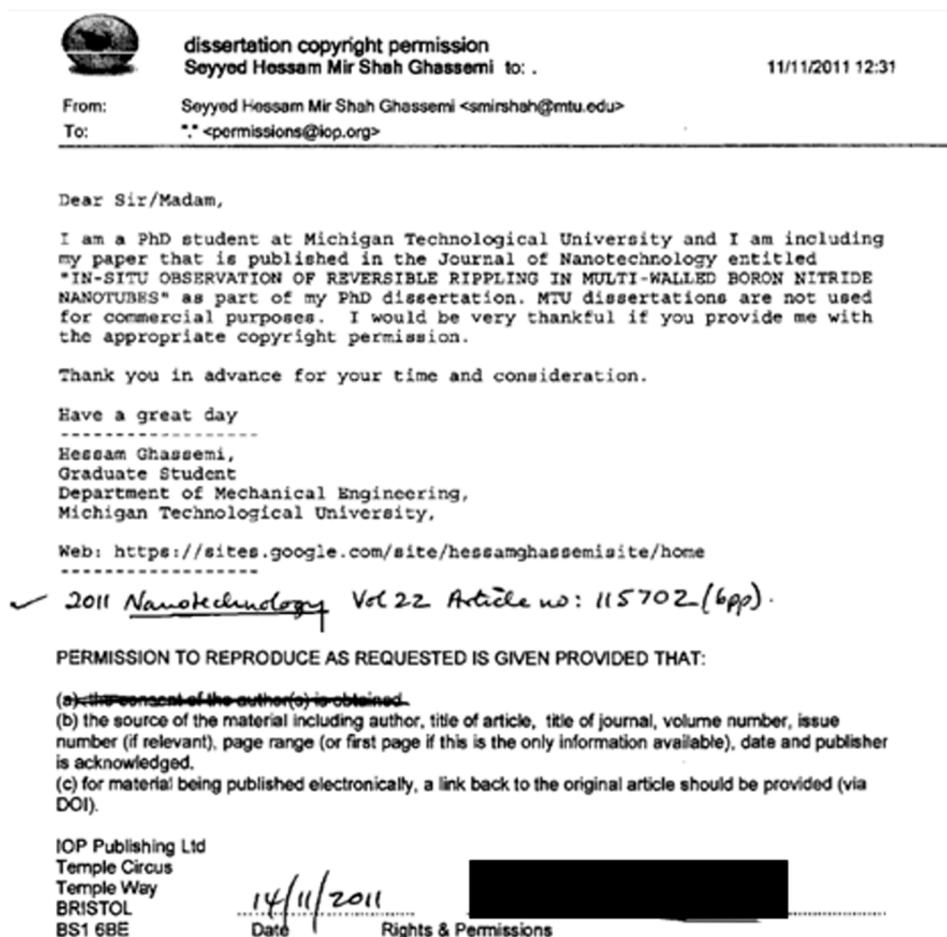
Thank you very much for your order.

This is a License Agreement between hessam ghassemi ("You") and American Institute of Physics ("AIP"). The license consists of your order details, the terms and conditions provided by American Institute of Physics, and the payment terms and conditions.

Get the printable license.

License Number	2785540281475
License date	Nov 10, 2011
Licensed content publisher	American Institute of Physics
Licensed content publication	Journal of Applied Physics
Licensed content title	Real-time fracture detection of individual boron nitride nanotubes in severe cyclic deformation processes
Licensed content author	H. M. Ghassemi, C. H. Lee, Y. K. Yap, R. S. Yassar et al.
Licensed content date	Jul 29, 2010
Volume number	108
Issue number	2
Type of Use	Thesis/Dissertation
Requestor type	Author (original article)
Format	Print and electronic
Portion	Excerpt (> 800 words)
Will you be translating?	No
Title of your thesis / dissertation	IN-SITU ELECTRICAL, MECHANICAL AND ELECTROCHEMICAL CHARACTERIZATIONS OF ONE-DIMENSIONAL NANOSTRUCTURES
Expected completion date	Jan 2012
Estimated size (number of pages)	100
Total	0.00 USD

LICENSES FOR CHAPTER-5



LICENSES FOR CHAPTER-6

Chapter 6 has been submitted to *Advanced Functional Materials*, but no copyright transfer agreement has been signed yet, as it is in the initial phase of review.

LICENSES FOR CHAPTER-7

Thank you very much for your order.

This is a License Agreement between hessam ghassemi ("You") and Springer ("Springer"). The license consists of your order details, the terms and conditions provided by Springer, and the payment terms and conditions.

Get the printable license.

License Number	2785920003355
License date	Nov 11, 2011
Licensed content publisher	Springer
Licensed content publication	JOM Journal of the Minerals, Metals and Materials Society
Licensed content title	In situ TEM monitoring of thermal decomposition in individual boron nitride nanotubes
Licensed content author	Hessam M. Ghassemi
Licensed content date	Jan 1, 2010
Volume number	62
Issue number	4
Type of Use	Thesis/Dissertation
Portion	Full text
Number of copies	1
Author of this Springer article	Yes and you are a contributor of the new work
Title of your thesis / dissertation	IN-SITU ELECTRICAL, MECHANICAL AND ELECTROCHEMICAL CHARACTERIZATIONS OF ONE-DIMENSIONAL NANOSTRUCTURES
Expected completion date	Jan 2012
Estimated size(pages)	100
Total	0.00 USD

LICENSES FOR CHAPTER-8

PERMISSION/LICENSE IS GRANTED FOR YOUR ORDER AT NO CHARGE

This type of permission/license, instead of the standard Terms & Conditions, is sent to you because no fee is being charged for your order. Please note the following:

- Permission is granted for your request in both print and electronic formats.
- If figures and/or tables were requested, they may be adapted or used in part.
- Please print this page for your records and send a copy of it to your publisher/graduate school.
- Appropriate credit for the requested material should be given as follows: "Reprinted (adapted) with permission from (COMPLETE REFERENCE CITATION). Copyright (YEAR) American Chemical Society." Insert appropriate information in place of the capitalized words.
- One-time permission is granted only for the use specified in your request. No additional uses are granted (such as derivative works or other editions). For any other uses, please submit a new request.

LICENSES FOR CHAPTER-9

Thank you very much for your order.

This is a License Agreement between hessam ghassemi ("You") and American Institute of Physics ("AIP"). The license consists of your order details, the terms and conditions provided by American Institute of Physics, and the payment terms and conditions.

Get the printable license.

License Number 2785920582992

License date Nov 11, 2011

Licensed content publisher American Institute of Physics

Licensed content publication Applied Physics Letters

Licensed Real-time observation of lithium fibers growth inside a

content title	nanoscale lithium-ion battery
Licensed content author	Hessam Ghassemi, Ming Au, Ning Chen, Patricia A. Heiden, et al.
Licensed content date	Sep 22, 2011
Volume number	99
Issue number	12
Type of Use	Thesis/Dissertation
Requestor type	Author (original article)
Format	Print and electronic
Portion	Excerpt (> 800 words)
Will you be translating?	No
Title of your thesis / dissertation	IN-SITU ELECTRICAL, MECHANICAL AND ELECTROCHEMICAL CHARACTERIZATIONS OF ONE-DIMENSIONAL NANOSTRUCTURES
Expected completion date	Jan 2012
Estimated size (number of pages)	100
Total	0.00 USD

LICENSES FOR Figure A.1

December 12, 2011

Hessam Ghassemi Graduate Student Department of Mechanical Engineering Michigan Technological University

Ref # 10902

Thank you for your permission request dated December 9, 2011. We are pleased to grant you a non-exclusive, non-transferable permission, English rights, limited to print and World Wide Web format only, provided you meet the criteria outlined below.

Permission is for a one-time use and does not include permission for future editions, updates, additional electronic forms, databases, translations, or any other matters. Permission must be sought for each additional use. This permission does not include the right to modify APS material.

Please print the required copyright credit line on the first page that the material appears: “Reprinted (abstract/excerpt/figure) with permission from [FULL REFERENCE CITATION] as follows: authors names, journal title, volume number, page number and year of publication. Copyright (YEAR) by the American Physical Society.

The following language must appear somewhere on the website: “Readers may view, browse, and/or download material for temporary copying purposes only, provided these uses are for noncommercial personal purposes. Except as provided by law, this material may not be further reproduced, distributed, transmitted, modified, adapted, performed, displayed, published, or sold in whole or part, without prior written permission from the American Physical Society.”

Provide a hyperlink from the reprinted APS material (the hyperlink may be embedded in the copyright credit line). APS’s link manager technology makes it convenient and easy to provide links to individual articles in APS journals. For information, see: <http://link.aps.org/>.

You must also obtain permission from at least one of the authors for each separate work, if you haven’t done so already. The author’s name and address can be found on the first page of the published Article.

Use of the APS material must not imply any endorsement by the American Physical Society.

Permission is granted for use of the following APS material only:

☐ Fig. 1, Phys. Rev. B 50, 7884 (1994)

Permission is limited to the single title specified or single edition of the publication as follows:

□ Ph.D. dissertation by Hessam Ghassemi to be published by Michigan Technological University

If you have any questions, please refer to the Copyright FAQ at: <http://publish.aps.org/copyrightFAQ.html> or send an email to assocpub@aps.org.

Sincerely,

Eileen LaManca

Publications Marketing Coordinator